University of Catania

International PhD in Translational Biomedicine

XXVIII cycle

Coordinator: Prof. Daniele Filippo Condorelli

Valentina Giglio

Biofunctionalized systems for drug discovery and delivery

PhD Thesis

Tutor: Prof. Giuseppe Spoto

Co-tutor: Prof. Graziella Vecchio

2013-2015

ABSTRACT

During this doctoral research work new potential drug delivery vehicles for targeted treatment of cancers were developed. For this purpose, both soft and hard materials were subject of study. Firstly, the synthesis, the characterization and the biological evaluation of monomeric β-cyclodextrins functionalized with folic acid (FA) were the focus of this research. In particular, four new conjugates (CyD-FAs), both 3- and 6-functionalized β-CyDs (β-CyD3 and β-CyD6) linked to the α- or γ-carboxylic group of the FA were synthesized, isolated and fully characterized. Furthermore, the ability of these compounds to include the anticancer drug LA-12 and to deliver it selectively to FR (+) tumor cell lines was investigated.

Since the promising results obtained with these CyD-FA conjugates as carriers for LA-12, polymeric nanoparticles based on cross-linked cyclodextrins were designed for drug delivery purposes. These systems, offer the advantages of CyD-type complexation in a synergistic way, resulting more effective than the parent CyDs. In particular, CyD-based polymers and oligomers were synthesized, functionalized with FA and tested as delivery systems towards different hydrophobic anticancer or anti-inflammatory agents. Furthermore, for selected systems, the binding constants of the formed inclusion complexes were determined as well.

Concerning hard materials, mesoporous silica nanoparticles were investigated. A new disc-shaped mesoporous material, the nanodiscs (NDs), was synthesized, isolated and fully characterized. This material was firstly used for the preparation of self-assembled monolayers (SAM), to be employed in targeted cancer cell adhesion and *in-situ* drug delivery. For this purpose, the NDs-monolayers were functionalized with FA as targeting moiety. Thanks to their large surface area and the possibility of high density of superficial functionalization with bioactive molecules, these systems resulted effective in binding cancer cells even upon short contact times. Moreover, exploiting the porosity of the synthesized particles, the intracellular release of small hydrophobic molecules pre-loaded in the channels of the NDs were achieved.

Secondly, preliminary biological experiments carried out to test the cellular uptake of NDs, and the drug-carrier ability were performed. Finally, in the attempt to increase the biodegradability of these interesting structures, disulfide-doped mesoporous silica nanodiscs (ss-NDs) were also prepared. Full characterization and preliminary biological assays of these hybrid materials was also performed, and their degradation in redox conditions investigated. This novel material, taking advantage of bio-redox reactions, undergoes a controlled disintegration process in presence of reducing agents (i.e. glutathione), displaying an improved drug delivery action.

Table of Contents

1 INTRODUCTION

Cancer is one of the most leading causes of death worldwide. In fact, according to the World Health Organization (WHO) report 2014, 8.2 million deaths were attributed to cancer, which constituted 13% of all deaths and in the next two decades, new global cancer incidences are expected to increase.[1] The lack of selective delivery of anti-cancer compounds to neoplastic tissues is one of the main reasons of such a high incidence for cancer disease. Currently available therapies do not suffice to erase this plague and new technologies are required. In this context, nanotechnology recent improvements towards the development of nanotherapeutic products holds great promise to ameliorate therapeutic strategies against cancer. Nanocarriers have unique properties such as nanoscale size, high surface-to-volume ratio, and favorable physico-chemical characteristics.[2] They can enhance the drug therapeutic effect acting both on its pharmacokinetic and pharmacodynamic profile. Embedding of drugs into nanocarriers can increase *in vivo* stability, extend the life span of the drug, and allow for controlled drug release.[3]

A wide range of nanomaterials based on inorganic, lipid, protein, glycan or other organic compounds have been employed for the development of new anticancer vehicles.

1.1 Nanotherapeutic platforms

The Nobelist Richard Feynman in 1959[4] gave a lecture entitled "there is plenty of room at the bottom" introducing the concept of nanotecnology for the first time. Nanotecnology refers to the handling and engineering material with dimensions on the nanometer scale (1–100 nm).[5]

Synthetic nanoparticles (NPs) are endowed with several advantage for the development of nanotherapeutic products such as size in the nanometer range that give them the ability to cross biological barriers[6] including the blood-brain barrier[7] or the cell membrane by different uptake mechanisms.[8] They can therefore interact with a wide panel of biological entities (e.g. from proteins to cells). In addition, NPs exhibit tuneable physical, chemical or biological properties that can dramatically change as a function of their size due to modified quantum mechanical properties.[9]

Depending on the type of applications, NPs can span different shapes (e.g. nanospheres, nanotubes, nanorods, nanowires, nanodiscs) and materials (e.g. silica, metal, lipid- or polymer-based) so they can be hollow, porous or solid. An additional advantage of NPs may be their increased loading capacity compared to molecular vectors. For instance, it has been shown a 70

nm NP can contain ~2,000 siRNA drug molecules whereas antibody conjugates have less than 10 siRNA molecules.[10] These characteristics confer NPs high transport abilities, making them attractive tools for the design of biosensors, imaging contrast agents and nanotherapeutic carriers.

Various types of nanotherapeutic products have been used in clinical cancer care, including viral vectors, drug conjugates, lipid-based nanocarriers, polymer-based nanocarriers, and inorganic nanoparticles. Some of these products current in clinical studies or approved for clinical cancer care are summarized in table 1.

Concerning lipid-based nanocarriers, the most frequently investigated are liposomes and micelles. A pegylated liposomal doxorubicin (Doxil® or Caelyx®) was the first nanocarrier approved by the US Food and Drug Administration (FDA) in 1995[17] (Fig. 1). In the liposomal formulation the critical cardiotoxicity of free doxorubicin is markedly redused. Concerning polymeric nanoparticles can be distinguished NPs based on natural polymers (i.e. protein or glycans nanocarriers) or based on synthetic polymers. The only one protein-based nanoparticle has found its way into the clinic so far is an albumin-bound paclitaxel (Abraxane®)[16], used for the therapy of breast cancer, non-small-cell lung cancer, and pancreatic cancer.

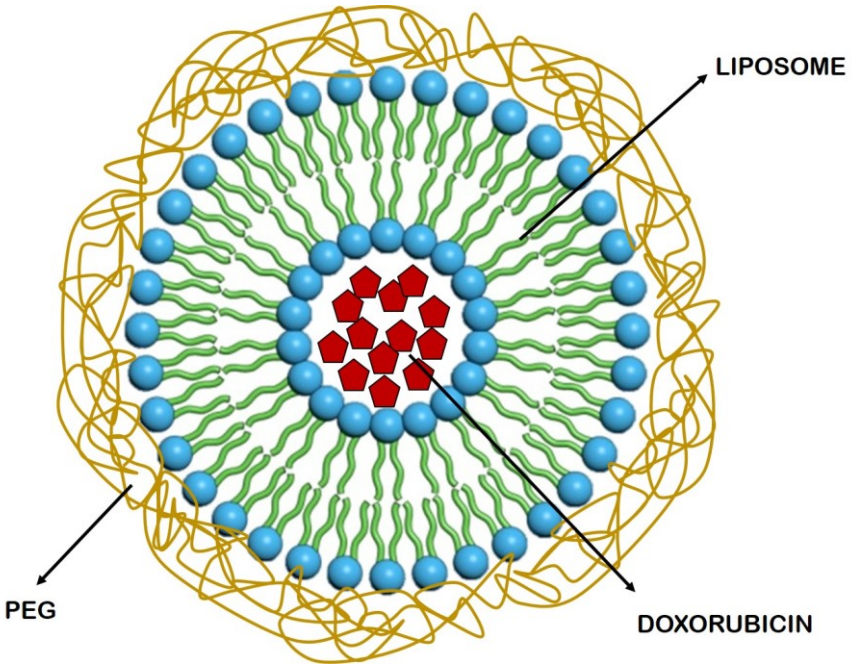

Figure 1: Schematic structure of Doxil® fomulation

Among the synthetic polymers, poly (D,L-lactide-co-glycolide) (PLGA) and poly(amidoamine) dendrimers (PAMAM) have been the most extensively investigated for drug delivery.[11,12] Inorganic nanoparticles have been also used for a variety of applications, including tumor imaging, enhancement of radiotherapy, or drug delivery.[13] In this group of NPs, iron oxide nanoparticles (magnetic NPs) have been tested in clinical studies for magnetic resonance imaging

of tumors.[14] For instance NanoTherm®, an aqueous colloidal dispersion of iron oxide nanoparticles, was approved in Europe in 2010 for the treatment of brain tumors.[15]

Table 1: Nanocarrier-drug conjugates approved or in clinical trials.

Product	Platform	Drug	Indication	Status	Reference
Abraxane®	Albumin bonded NP	Paclitaxel	Breast cancer, pancreatic cancer	2005	16
Doxil®/Caelyx®	Liposome	DOX	Breast cancer, ovarian cancer	1999	17
Myocet®	Liposome	DOX	Breast cancer	2000	18
CT-2106	Polyglutamic acid drug conjugate	Camptothecin	Colon cancer, ovarian cancer	Phase 1/2	19
NKTR-102	PEG drug conjugate	Irinotecan	Breast cancer, ovarian cancer, colorectal cancer	Phase 3	20
Lipoplatin	Liposome	Cisplatin	Non-small-cell lung cancer	Phase 3	21
ThermoDox	Thermo-sensitive liposome	DOX	Primary hepatocellular	Phase 3	22
CALAA-01	CyD polymeric NP	siRNA targeting ribonucleotide reductase subunit 2	Solid tumors	Phase 1	23
CRLX-101 (IT-101)	CyD polymeric NP	Camptothecin	Solid tumors, renal cell carcinoma, rectal cancer, non-small-cell lung cancer	Phase 1/2	24

1.2 Why develop nanosized therapeutic?

There are persuasive topics in favor of developing nanocarriers to improve drug delivery.

First, nanoparticles may help to overcome problems of solubility and chemical stability of anti-cancer drugs. Poor water solubility limits the bioavailability of a compound and may prevents its development as an anti-cancer agent.[25] Uptake and delivery of poorly soluble drugs could be increased by loading the compound in a hydrophilic nanocarrier. At the same time, this may improve their chemical stability. The radiosensitizer wortmannin is an example of a drug "abandoned" (neglected) because of its poor solubility and chemical instability. Using a lipid-based nanocarrier system, the solubility of wortmannin was increased from 4 mg/L to 20 g/L while increasing its stability *in vivo*. Moreover, this nanoparticle formulation has both improved wortmannin efficacy and reduced its toxicity.[26] Cyclodextrins (CyDs) represents a means to overcome drug solubility and availability. In literature are reported a plenty of papers on the use of CyDs to develop drug delivery systems.[27,28] This class of molecules will be discussed in detail in the section 1.7.1.

Furthermore, nanocarrier can protect anti-cancer compounds from biodegradation or early excretion influencing the pharmacokinetic profile of a compound. For example, the encapsulation of those drugs cleaved enzymatically (e.g., siRNA by RNAses in the plasma, proteins by pepsin or trypsin in the stomach) into nanocarriers or coupling to synthetic polymers may overcome this problem. It is widely known in the literature that the bioconjugation with polyethylene glycol (PEG) derivatives prolongs the circulation time and the biocompatibility of a compound avoiding premature degradation phenomena.[29,30] Nanoplatin (NC-6004, Fig. 2) is a PEG-PLGA polymeric nanoparticles with cisplatin as payload. This NP formulation is currently in phase II clinical study thanks its good pharmacokinetic profile as well as minimized toxic effects related to the administration of naked cisplatin.[31]

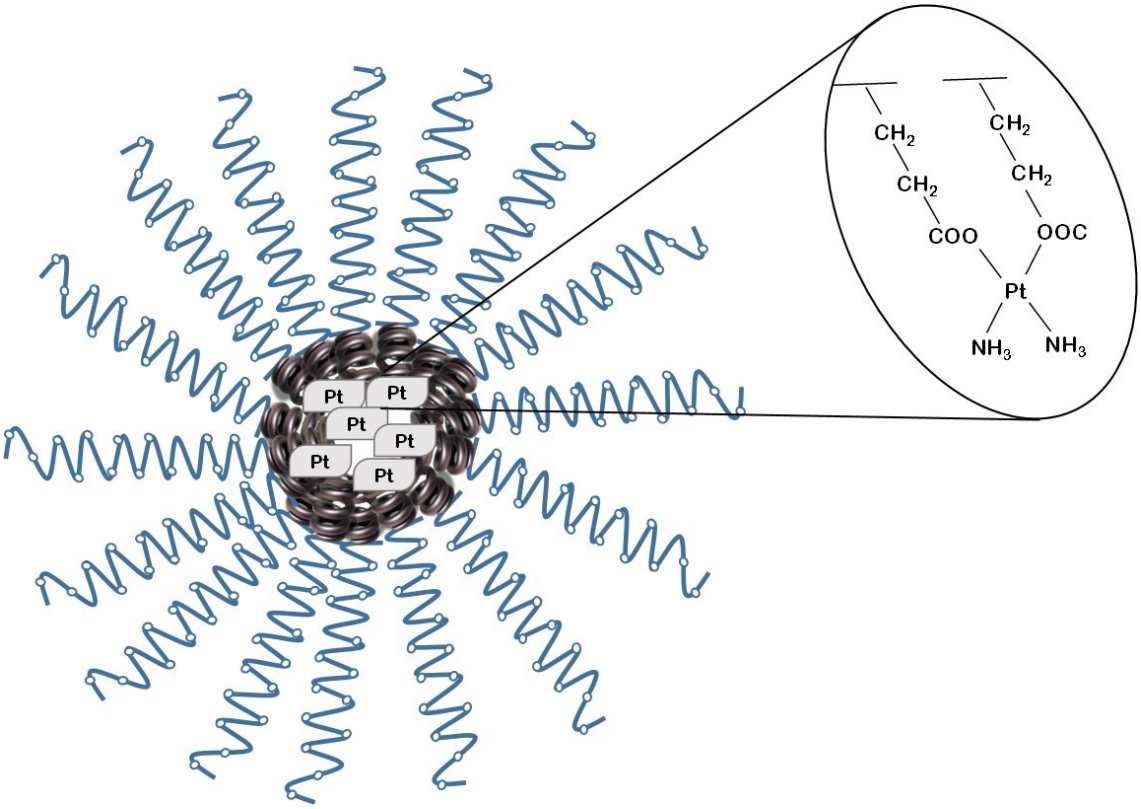

Figure 2: Structure of cisplatin-incorporated polymeric micelle, NC-6004. Core part, cisplatin residue bound to poly-L-glutamic acid (PLGA). Exterior part, PEG.

Nanotechnology can help to improve biodistribution and targeting of anti-tumor agents as well. Distribution of anti-cancer drugs is defined by their physico-chemical properties and is limited by drug penetration into tumor tissue,[32,33] which hampers its efficiency.[34] However, nanocarries can be engineered to improve this feature and redirect chemotherapeutics selectively to tumor site. Both passive and active targeting strategies are used to directing anti-cancer drugs.

Finally, nanocarriers can be designed to release their cargo upon a trigger resulting in stimuli-responsive nanomedicine therapeutics. Triggers can be divided into internal (patho-physiological/pathochemical condition) and external (physical stimuli such as temperature, light, ultrasound, magnetic force, and electric fields) stimuli. Internal stimuli include changes in pH, redox, ionic strength, and oxidative stress in the target tissues.[35,36] For instance, in solid tumors, the extracellular pH is more acidic than the systemic one.[37] Similarly, the pH of intracellular organelles (*e.g.*, endosomes and lysosomes) differs from that of the cytoplasm or blood. This condition can be used to enhance intracellular release of drugs from nanocarriers. For example, pH-responsive liposomes were used to trigger the release of the drug and therefore increase the therapeutic efficacy.[38]

1.3 Drug targeting

The goal to develop safer therapeutical agents that are efficiently and selectively delivered to the desired site of action without affecting non-target cells has begun an attractive and actively pursued objective in pharmaceutical research. To achieve tumor targeting, nanocarriers must first overcome systemic barriers, especially clearance via phagocytic uptake and hepatic filtration. Then they are expected to extravasate the tumor vasculature and penetrate the tumor microenvironment so that even cancer cells situated distal to the tumor vessel can be exposed to the anticancer agent at high enough concentrations. Targeting of nanoparticles to diseased tissue and cells generally assumes two strategies: passive (or physical) and active (or chemical) targeting.

1.3.1 Passive targeting

Conventional surface unmodified nanoparticles are usually caught in the circulation by the reticuloendothelial system, such as the liver and the spleen, depending on their size and surface characteristics.[39] The fate of injected nanoparticles can be controlled by adjusting their size and surface characteristics. One of the advantages of nanoparticles is that their size is tunable. The size of nanoparticles used in a drug delivery system should be large enough to prevent their rapid leakage into blood capillaries but small enough to escape capture by fixed macrophages that are lodged in the reticuloendothelial systems. Usually the range of size should vary from 100 to 600 nm, because this is the range of size of gap junction between endothelial cells of the leaky tumor vasculature.[40] In addition to their size, the surface characteristics of nanoparticles are also an important factor determining their life span and fate during circulation relating to their capture by macrophages. Nanoparticles should ideally have a hydrophilic surface to escape macrophage capture.[41] This can be achieved coating the surface of nanoparticles with a hydrophilic polymer, such as PEG, which protects them from opsonization by repelling plasma proteins.[29] Nanoparticles that satisfy the size and surface characteristics requirements described above for escaping reticuloendothelial system capture can circulate for longer times in the bloodstream and have a greater chance of reaching the targeted tumor tissues. Tumor vessels have the unique pathophysiologic property to selectively accumulate macromolecules, including nanoparticles in tumor tissues.[42] This phenomenon called “enhanced permeability and retention (EPR) effect” (Fig. 3) is due to abnormal and leaky architecture of blood vessels surrounding the tumor.[43,44] The cutoff size of fenestrations and gaps between endothelial cells, varies from case to case, from 200 to 800 nm, in contrast to normal endothelium with pores with 5–10 nm gap.[45-48] This

damaged regulation of tumor blood vessels allow nanoparticles to preferentially accumulate in tumors rather than spread into healthy tissues. In addition, cancer cells use high rates of glycolysis to obtain extra energy, resulting in a relatively acidic micro-environment when compared with normal tissues.[49,50] These characteristics of tumor cells provide a strong rationale for releasing drugs as a function of their pKa and the cellular pH gradient. In this passive-targeting mechanism, the anti-cancer drug loaded on nanocarriers is engineered to be stable within microenvironments at physiological pH (i.e. during transport), while the release of the drug can be triggered at the tumor site, where the pH is lower than that of normal cells. The EPR effect provides several benefits when compared to free diffusion of drug molecules into tumor tissues. However, EPR-based drug delivery systems as a passive targeting approach also face challenges. For instance, the EPR effect is limited to specific stages and types of tumors.[51] In addition, the complexity of the tumor micro-environment offers many barriers (e.g., high interstitial fluid pressure, dense collagen matrix, etc.) that hamper the effect of passively delivered drugs into the tumor. Moreover, the longer circulation times of the nanosystems could be associated with several chemotherapy-induced side effects, such as stomatitis and palmar-plantar erythrodysesthesia (also known as hand-foot syndrome) as found for a PEGylated liposomal doxorubicin.[52] A more promising way to overcome these limitations is to use site-targeted delivery systems discussed in the section below.

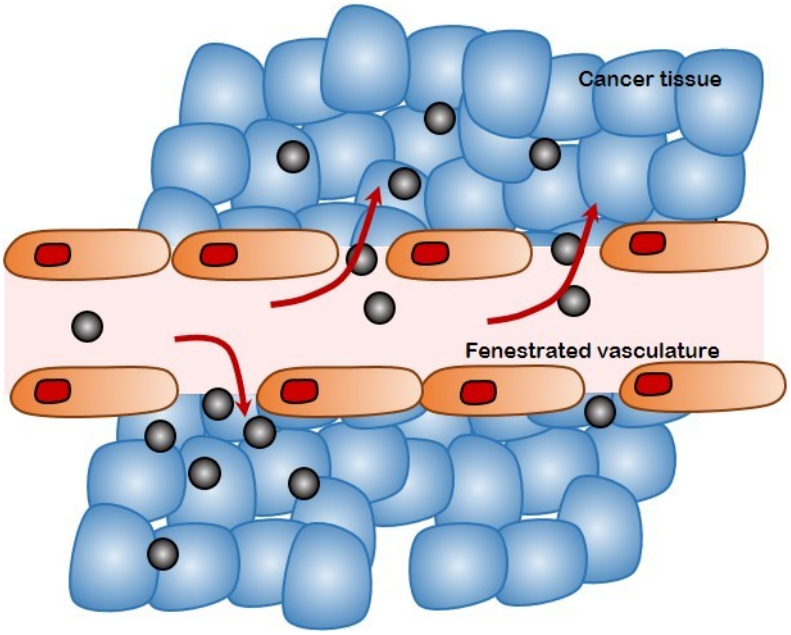

Figure 3: Schematic illustration of EPR effect: extravasation of nanoparticles through fenestrated vasculature leads to passive targeting of tumor tissue.

1.3.2 Active targeting

The concept of site-selective drug delivery has evolved since Nobelist Dr. Paul Ehrlich launched his idea of the "magic bullet", an active chemical substance delivered only at the disease site and left the healthy tissues intact, over a century ago.[53] Since then, the goal to develop safer therapeutical agents that are efficiently and selectively delivered to the desired site of action without affecting healty cells has begun an attractive and actively pursued task in pharmaceutical research. Over the years, engineered nanoparticles with selective targeting ligands that recognize particular receptors in target cells with subsequent uptake through receptor-mediated endocytosis have been developed.[2] The internalization process starts with the formation of the endosome by invagination of plasma membrane to envelop the conjugates formed by cell receptors and nanomaterials. Subsequently, newly formed endosomes inside the cell can fuse with lyososomes, which are highly acidic organelles rich in degrading enzymes. After endosomal escape, the cargo is released and the receptor free from the conjugate returns to the cell membrane to start a second round of transport through endocytic recycling pathways.[54] One of the most used strategy to cause the rupture of the lysosome is the so called "proton sponge effect"[55] in which the use of cationic polymers such as PEI (polyethylenimine) or PAMAM (polyamidoamine), acting as buffering molecules trigger a dual purpose: *(i)* to inhibit the activity of lysosomal nuclease avoiding the degradation of the cargo especially in the case of nucleic acids and *(ii)* to change the osmolarity of acidic vesicles resulting in endosomal swelling and rupture (Fig. 4). Meanwhile, to increase the specificity, the corresponding antigen or receptor should be expressed exclusively and homogeneously on all tumor cells but not present on healthy tissues.

Summarizing, the ideal features for smart anticancer nanosystems include long circulation time, selective tumor-cell targeting, the ability to enter target cells, escape endosomal entrapment and to trigger the release of cargoes in a controlled manner.

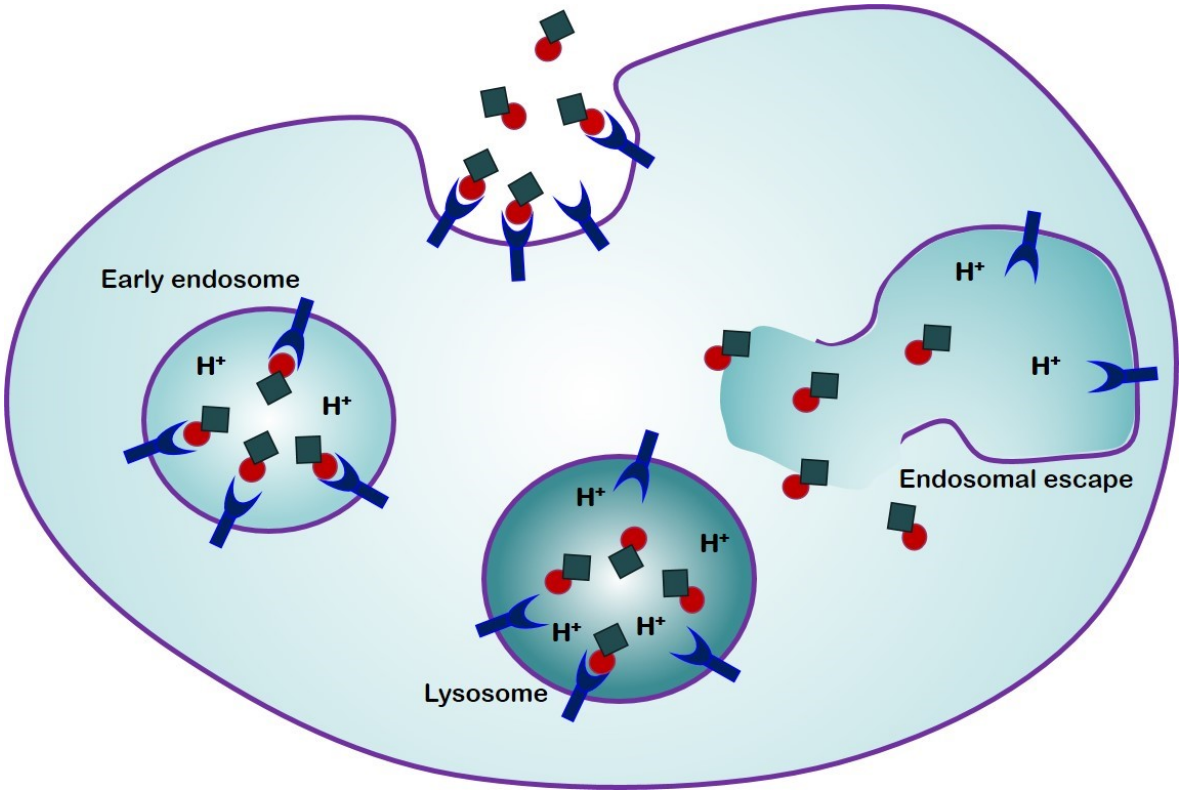

Figure 4: Schematic representation of ligand-meditated delivery of cargo. After endosomal escape, the nanoparticle can be engineered to target various cellular compartments such as mitochondria, endoplasmic reticulum, golgi, nucleus, and cytoplasm.

1.4 Biomolecules as cell targeting agents

To achieve significant therapeutic effect, NPs may need to deliver their cargoes inside cells. This is absolutely required when transported agents cannot diffuse freely through biological membranes (e.g. nucleic acids and proteins). Cell entry can be induced by decoration of NPs with biomolecules that not only function as determinants of cell targeting, but also promote the internalization of NPs upon binding with their specific receptors. Often, cell proliferation markers are a significant target for cancer therapeutics, as many of these markers are highly overexpressed on certain tumor cells. The most studied internalization strategy receptor-mediated are:

1) The transferrin receptor. The transferrin receptor is a membrane protein involved in iron homeostasis and the regulation of cell growth. Many factors make this receptor an attractive target for cancer therapy,[56] such as the high levels of expression of transferrin receptor in cancer cells (up to 100-fold higher than the average expression of normal cells), its extracellular accessibility, its ability to internalize and its central role in the

cellular pathology of human cancer. Transferrin receptor targeting for cancer therapeutics has been used in human clinical trials with adriamycin,[57] cisplatin,[58] and diphtheria toxin.[59]

2) Glycoproteins expressed on cell surfaces. Lectins are proteins of non-immunological origin which are able to recognize and bind the carbohydrate moieties of glycoproteins expressed on cell surface. Cancer cells often express different glycoproteins compared to normal cells; in addition, the lectins-carbohydrate interaction is very specific. Lectins can be incorporated into nanoparticles as targeting moieties that are directed to cell-surface carbohydrates (direct lectin targeting) or carbohydrates moieties can be coupled to nanoparticles to target lectins (reverse lectin targeting). These direct or reverse approaches are currently applied for colon drug targeting.[60]
3) The Epidermal growth factor receptor (EGFR). The EGFR is a member of the ErbB family, a family of tyrosine kinase receptors. Its activation stimulates key processes involved in tumor growth and progression, including proliferation, angiogenesis, invasion and metastasis. EGFR is frequently overexpressed in a lot of cancer, including colorectal, ovarian, kidney, pancreatic and prostate cancer.[61] A current cancer treatment that address EGFR is the monoclonal antibody Cetuximab (Imclone Systems Inc., New York, NY and Bristol-Myers Squibb, Princeton, NJ), which targets the extracellular domain of EGFR .[62,63] Thus, the conjugation of nanoparticles with Cetuximab could provide an effective tools for drug targeted delivery.
1) The folate receptor (FR). FR is a well-known tumor marker overexpressed on 40% of human cancers that binds to the vitamin folic acid and folate-drug conjugates with a high affinity and moves these bound molecules into the cells via receptor-mediated endocytosis.

1.5 Folic acid as targeting moiety

Folic acid (FA, vitamin B9) is a water-soluble vitamin essential in biosynthesis of nucleotide bases. The chemical structure of folic acid is reported in figure 5, in which three portions can be distinguished, more precisely, 2-amino-4-hydroxy-6-methyl-pterine (pteridine), para-amino-benzoic acid (PABA) and glutamic acid. FA can enter the cell through two different routes: 1) by the Reduced Folate Carrier (RFC), a bidirectional anion-exchange mechanism, which has low affinity for folate; and 2) by the Folate Receptor (FR) pathway, which has high-affinity for folate.

FR is a glycosyl-phosphatidylinositol-anchored glycoprotein, and is one of the most highly researched targets for cancer therapeutics.[64-67]

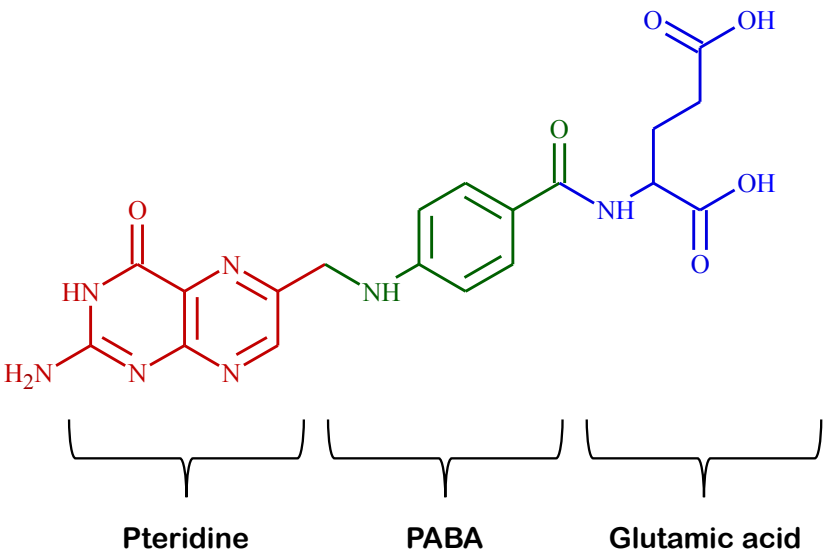

Figure 5: Chemical structure of folic acid.

The utility of folic acid as targeting moiety has arisen primarily for its ease conjugation to both therapeutic and diagnostic agents, its high affinity for the folate receptor (Kd 10^{-10} M), even after conjugation, and finally for the limited distribution of its FRs in normal tissues.[68] FRs include at least four isoforms, α , β , γ / γ ′ and δ, displaying divergent patterns of tissue expression,[69] however, to date most of the literature has been focused on FR- α and FR- β. These two isoforms share high amino acid sequence identity (~ 70%) and are distinguishable by differential affinities for folic acid and stereoisomers of reduced folates. In particular, FR- α is overexpressed in several carcinomas, especially in ovarian, breast, colon, and renal cell carcinomas.[70] Whereas, FR- β is a differentiation marker in the myelomonocytic lineage during neutrophil maturation[71] and is amplified in activated monocytes and macrophages.[72] In addition, FR- β is expressed in a functional form in chronic myelogenous leukemia (CML), in 70% of acute myelogenous leukemias (AML)[71,73] and in activated macrophages associated with rheumatoid arthritis and other chronic inflammatory diseases.[74] Tissue selective expression of FR- α and FR- β and the lack of normal tissue expression of FRs suggest that these can be used as markers for targeted drug delivery. Folate conjugates have been shown to retain affinity for FRs and interact with the target cells via high affinity binding and are internalized by receptor-mediated endocytosis.

Several chemotherapeutic agents have been conjugated to folate for targeted delivery to FR (+) cells. The functionalization have been achieved exploit the two carboxylic groups on the glutamic residue that can be functionalized through amide bond formation leading to γ- and α-FA derivatives. The γ-carboxylate derivatives are the major products because of steric and electronic

effects. Moreover, it has been demonstrated that the FR recognizes folate derivatized at the γ- but not at the α-carboxylate.[75] Therefore, the conjugation with FA is accompanied by a selectivity issue requiring the isolation of the γ-folate derivative.

Folate conjugates of platinum,[76] paclitaxel[77] or maytansinoids[78] have been reported and in all the cases, these conjugates have shown high affinities for FRs and selective cytotoxicity against FR(+) cells. In early works, FA has been conjugated to randomly methylated β-cyclodextrins, to give per- or mono-functionalized CyDs.[79] Folate- modified βCyDs[80] have been used as carriers of doxorubicin modified with an adamantyl residue. Generally, CyD-FA conjugates used as drug carriers were mixtures of α and γ regioisomers. Many other types of drug carriers have been conjugated to folate, including liposomes,[81] polymeric nanoparticles,[82] metal nanoparticles[83] or mesoporous silica nanoparticles.[84]

Generally, multiple folates molecules are conjugated to each particle, which enables high affinity multivalent interaction to the FRs. Among the different class of NPs, several studies reported on FA conjugation of mesoporous silica to achieve effective drug delivery to tumor cells.[85-87] In this context, it has been reported that FA-targeted camptothecin or paclitaxel-loaded mesoporous silica NPs could be effectively used for cancer imaging, targeting, and drug delivery in FR (+) human pancreatic cancer cells PANC-1 and BxPC-3.[88] In addition, Fan et al. have developed the pH-sensitive FA-conjugated DOX-loaded mesoporous silica NPs, which could selectively kill FR (+) HeLa cells, but not FR (-) A549 and L929 cells.[85] Also FA functionalized liposome are widely represented in literature, for instance folate targeted liposomes have been employed for the delivery of chemotherapeutic agents, such as paclitaxel and doxorubicin, avoiding the common multi-drug resistance experienced by cancer patients.[89,90]

1.6 Stimuli-responsive systems/triggered release

Stimuli-responsive systems promote the release of drugs exclusively in response to a trigger present in the neoplastic tissue, minimizing systemic exposure to the compound. Triggers can be divided into internal (patho-physiological condition) and external (physical stimuli such as temperature, light, ultrasound, magnetic force, and electric fields) stimuli. Internal stimuli include changes in pH, redox or ionic strength in damaged tissues.[35,36] It has been reported the pH profile of pathological tissues, such as upon acquisition of inflammation, infection, and cancer, is significantly different from that of the normal tissue.[91] The extracellular pH at systemic sites of infections, primary tumors, and metastasized tumors is lower than the pH of normal tissue.[37] In addition, the pH of intracellular organelles (e.g., endosomes and lysosomes) differs

from that of the cytoplasm or blood. The strategy of embedding pH-responsive compounds into nanocarriers or conjugated has been widely used to achieve efficient intracellular delivery and sub-cellular localization of macromolecules. For instance, Obata et al.[38] reported pH-responsive liposomes containing synthetic glutamic acid-based zwitterionic lipids used to trigger the release of doxorubicin (DOX) and therefore increase the therapeutic efficacy *in vitro* and *in vivo*. In addition, it has been widely adopted in literature the use of hydrazone-based prodrug endowed of self-hydrolysis behavior in the acid environment of lysosomes resulting in the release of active drug.[92] Also the hypoxic area of tumors could be considered a microenvironment able to trigger the drug release exhibiting low oxygen pressure and poor nutrient levels. Such an environment is rich in reductive agents (i.e. glutathione) which can be used for triggered release from redox-responsive nanocarriers.[93] Disulfide-containing nanocarriers are the most widely studied redox-responsive technology. Increased glutathione levels lead to a cleavage of disulfide bonds and hence trigger the release of drugs in the tumor tissue.[94] Several materials have been reported in the literature in which S-S cleavable bonds were introduced into framework of the nanoparticles to act as a self-destruction trigger in reducing media, such as: polymeric particles,[95,96]micelles,[97,98] mesoporous silica[99,100] and organosilica[101,102] nanoparticles.

Concerning physical stimuli to trigger the release of drugs, the use of hyperthermia has become an area of active investigation for the past 20 years,[103] to induce the release of drugs from thermo-responsive nanocarriers such as ThermoDox.[104] In addition, hyperthermia increases vascular permeability thus facilitating delivery of the anti-cancer agents deeply into the tumor.[105] The temperature range for local hyperthermia rande between normal body temperature (37 °C) and a maximum of 42 °C.[106] Magnetic and electric fields are other possible external stimuli. Inorganic and paramagnetic nanoparticles (iron oxide nanoparticles) are responsive to an applied magnetic field. Thus, the nanocarrier can be guided to the tumor with high specificity and release its cargo at the target side through a hyperthermic effect.

1.7 Drug carriers investigated in this thesis

1.7.1 Cyclodextrin- based drug carriers

Cyclodextrins (CyDs) are cyclic oligomers of D-(+) glucopyranosyl units 1-4 linked which have a toroidal structure (Fig. 6). The natural α-, β- and γ- cyclodextrin consist of six, seven, and eight glucopyranose units, respectively. The intrinsic nature of CyDs provides them an external hydrophilic surface and a hydrophobic cavity. The OH groups are disposed outside, the primary OHs are around the upper rim and the secondary 2, 3 OHs around the wider rim.

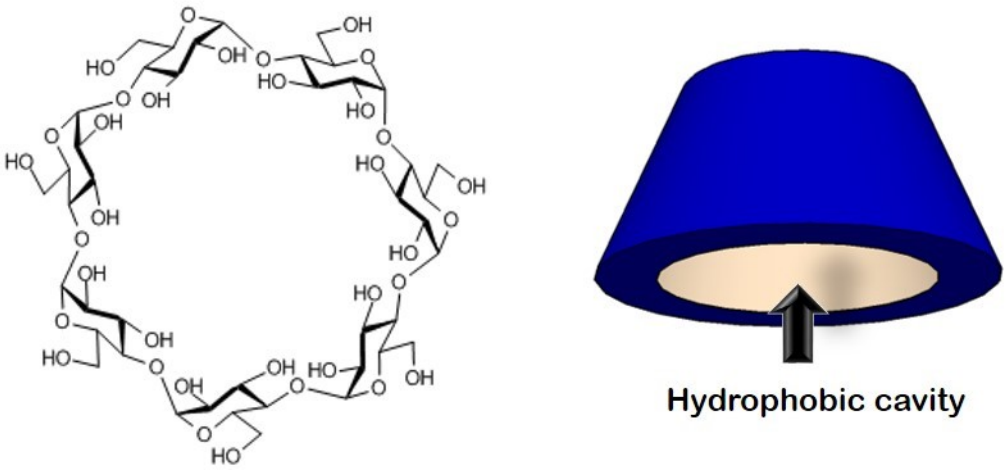

Figure 6: Chemical structure of β-CyD.

Cyclodextrin molecules have a large number of hydrogen donors and acceptors, and are poorly absorbed through biological membranes, and are non-toxic at low to moderate oral dosages. The presence of the hydrophobic cavity gives the ability of cyclodextrins to form inclusion complexes with a wide range of molecules. As a result, this class of molecules has found a number of applications in a wide range of fields and among them in pharmaceutical field as solubilizers and stabilizers.[107]

Modified CyDs can be obtained by functionalizing the OH groups. The replacement of CyD hydroxyl groups with other functional groups has been shown to improve markedly the field of application of CyDs, and the covalent conjugation of molecules with different properties provides an attractive approach in the building of multifunctional systems with applications in supramolecular, bioinorganic, organic, pharmaceutical and materials chemistry and separation sciences.[108] Thus, a number of CyD conjugates with amino acids,[109-112] peptides [113-115] and aromatic systems[116-120] have been reported over the years. In literature are reported a plenty of paper on the use of modified CyDs as nanocarries for the transport of low molecular-weight drugs. In addition, CyDs are also useful as active pharmaceutical ingredients (APIs) for various

diseases such as cancers, lysosomal diseases, amyloidosis and septic shock. For instance, sugammadex is one of the most relevant example of CyDs as APIs. It's a modified γ-CyD derivative designed to overcome the negative effect of rocuronium.[121] Furthermore, several cyclodextrins are used extensively to remove cholesterol from food and cultured cells and in 2010, the Food and Drug Administration (FDA) approved the intrathecal and intravenous administration of hydroxypropyl β-cyclodextrin (HPβ-CyD) in six-year-old twin girls suffering from Niemann-Pick disease type C (NPC).[122]

Meanwhile, the combination of CyDs and other functional materials have also been developed as drug carriers for low-molecular-weight drugs. For example, Shi et al. developed CyD-capped gold nanoparticles as carriers of oxoplatin.[123] Additionally, Li et al. constructed the novel polysaccharide-gold nanocluster consisting of gold nanoparticles bearing adamantane moieties and CyD-grafted hyaluronic acid and demonstrated its utility as tumor-selective carriers for various antitumor drugs, such as DOX, paclitaxel, camptothecin, irinotecan and topotecan.[124]

A number of CyD derivatives are FA-conjugated CyDs. For instance, Salmaso et al. reported that the conjugate of FA-β-CyD through a PEG spacer increases the uptake of rhodamine-B into KB cells, a human squamous carcinoma cell line FR (+), but not into MCF7 cells, human breast cancer cell lines FR (-).[125] In addition, Zhang et al. demonstrated that the β-CyD conjugate with FA having a PEG spacer through a click chemistry strategy spontaneously forms a nanoparticle with 5-fluorouracil in aqueous solution and shows efficient uptake in FR-α-overexpressing cells.[126] More recently, Okamatsu et al. prepared folate-appended CyDs possessing one or two caproic acids between FA and CyD molecules as spacer (Fol-c1-CyD and Fol-c2-CyD, respectively) and evaluated the inclusion complexation ability with DOX) and the antitumor effects of the DOX inclusion complexes *in vitro* and *in vivo*.[127,128] Meanwhile, Yin et al. synthesized folate-bearing CyD by direct condensation of FA with 6-amino-CyDs as delivery vehicle of an adamantyl-modified DOX. They demonstrated an efficient and preferentially targeted delivery of DOX into FR (+) tumor cells and a sustained drug release profile *in vitro*.[80] Recently, Motoyama et al. developed folate-appended methylβ-CyD (FA-M-β-CyD) as a novel antitumor drug carrier.[79] FA-M-β-CyD increased antitumor activity of DOX and paclitaxel in KB cells. Moreover, FA-M-β-CyD/DOX complex showed markedly high antitumor activity, compared to DOX alone and M-β-CyD/DOX complex *in vivo*.

These findings suggest that FA-appended β-CyD is potential as a tumor-selective drug carrier. Nevertheless, CyD-FA conjugates were used as mixtures of regioisomers at the α and γ position of the glutamic chain of FA. Furthermore, in all these conjugates CyD was functionalized at C-6 position.

1.7.2 CyD-based polymers

The ability of CyDs for complexation, as well as their capability to stabilize and solubilize guest compounds, makes these molecules great candidates for development of delivery systems. However, CyDs, in particular the most common β-CyD, have some limitations such as poor water solubility (1.85 g/100 ml H2O)[129] and the restriction of the single cavity size (diameter, 7 ˚A). To overcome these drawbacks, various CyDs derivatives have been developed.[130]

A solution to these challenges is the development of polymeric cyclodextrin structures (Fig. 7), which can simultaneously offer the advantages of both the amorphous state and CyD-type complexation without toxic effects.[131] The cyclodextrins fixed into polymeric structures behave differently from their monomeric counterparts; the polymeric structure can constrain the mobility of the CyDs. In addition, a high degree of branching may result in reduced complexation because of the steric hindrance. In contrast, a high number of adjacent CyD cavities within the polymeric structure, available to form inclusion complexes, can enhance their complexation ability in a synergistic way.[132, 133]

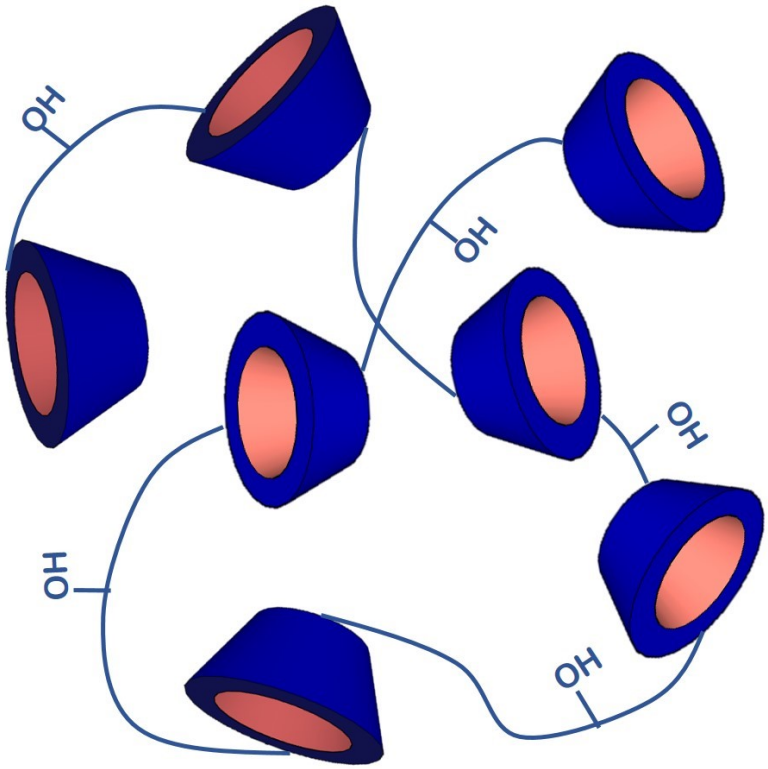

Figure 7: Schematic representation of β-CyD polymers.

1.7.2.1 Applications of CyD polymers in drug delivery

β-cyclodextrin- based polymer has been attracted by many researchers in recent years[134,] and a large variety of cross-linked CyD polymers exhibiting a dramatic enhancement of solubility and bioavailability towards various guests have been synthesized.[135,136] This systems appeared highly water-soluble and often more effectively than the parent β-CyD or dimethyl-β-CyD.[136]

Recently, Nie et al. evaluated the potential of a CyD polymer of 18 kDa for enhancing the dissolution rate and oral bioavailability of glipizide.[137] By mean of phase solubility studies they found CyD polymer 10-12 times more effective as solubilizer than HP-CyD. Furthermore, Jug et al. studied the interaction of triclosan (TR), a practically water-insoluble antimicrobial agent with β-CyD and CyD polymer, the stability constant of TR/CyD polymer complex calculated was 4.6 times higher than with the native β-CyD. Many other drug have been complexed with pCyD such as pedunculoside,[138] aceclofenac,[131] ketoprofen[139] or insulin.[140] All the above examples confirmed greater solubilizing and complexing ability of pCyD toward different lipophilic molecules.

CyD polymers have also been modified through the incorporation of anionic or cationic groups to increase their drug loading features.[141] Choline or carboxyl moieties have been added and their effect on the upload of charged drugs was investigated.[142,143]

Among the wide set of different classes of polymers that have been investigated, copolymers of cyclodextrin are extensively reported in literature as efficient drug delivery systems. One of the most promising with anticancer applications is CRLX-101 (Fig. 8). This latter is a polymeric nanoparticle (ca. 30−40 nm) made up of cyclodextrin-poly(ethylene glycol) copolymer conjugated to camptothecin (CTP, a potent anticancer drug), currently in phase II development.[24] CRLX-101 preclinical and clinical studies confirm that CyD copolymer can ameliorate not only solubility, formulation, toxicity, and pharmacokinetic challenges associated with administration of CPT, but more importantly, can impart unique biological properties that enhance camptothecin pharmacodynamics and efficacy.[144-146] CALAA-01 is another polymeric nanoparticle (50–70nm) based on CyD-PEG copolymers in clinical development for siRNA delivery. It is targeted to human transferrin receptors overexpressed on cancer cells to silence the expression of the M2 subunit of ribonucleotide reductase. Intracellular release of siRNA is triggered by an acidic endosomal pH.[147] Another examples concerns the anticancer drugs erlotinib that were loaded into β-CyD conjugated to dendritic polyamine polymer for brain cancer treatment. In this case the conjugation of β-CyD to dendritic polyamine polymer significantly reduced the cytotoxicity of polyamine.[148]

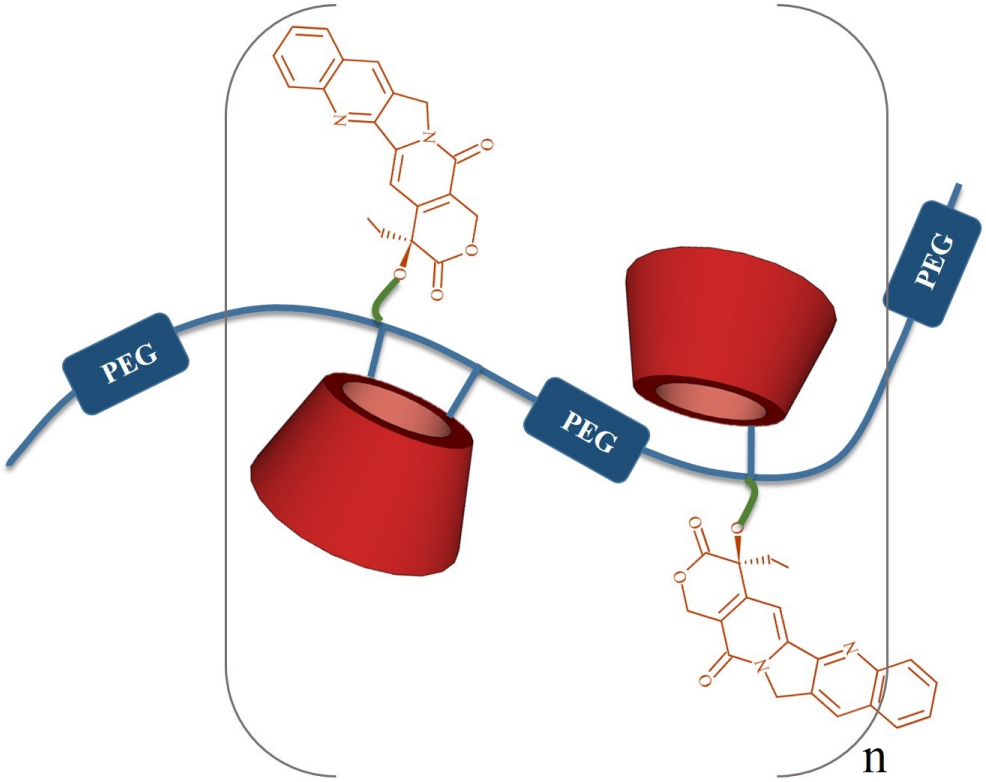

Figure 8: Structure of CRLX-101, a nanopharmaceutical product made of camptothecin conjugated to cyclodextrin-poly(ethylene glycol) (CyD-PEG) copolymer.

Although there is available a great amount of research studies on CyD polymers, just a few reports on CyD oligomers have been published to date.[135, 149] The oligomers are expected to possess intermediate properties between the monomeric and the polymeric counterpart and may have several advantages with respect to their higher MW polymeric analogues. A less branched architecture could provide a higher solubility and lower viscosity. Moreover, they can be more easily cleared from the body, after drug release, by renal excretion, whereas polymers with a higher molecular weight require a degradation process before removal (the MW threshold for renal excretion of polymeric drugs ranges from 30 to 50 kDa depending on the polymer structure).[150]

1.7.3 Mesoporous silica nanoparticles

In recent years, multifunctional mesoporous silica nanoparticles (MSNs) have attracted great attention due to their intriguing structural properties, such as a high internal surface area and pore volume, tunable pore sizes, colloidal stability and controllable particle morphology.[151] Moreover, it is possible to orthogonally functionalize either the inner pore system or the external particle surface with a variety of functional groups to further enhance drug loading and releasing ability.[152] The highly stable pore channels protect encapsulated drug molecules from degradation

in harsh environments during drug administration. For this reason, MSNs have been extensively employed to enhance the bioavailability of several hydrophobic drugs with limited applications due to their poor water solubility that results in poor absorption in the gastrointestinal tract after oral dosing. For instance, Zhang et al[153] discovered that MSNs improves the bioavailability of hydrophobic telmisartan (TEL) after oral administration compared with that unloaded product. The attractive features of MSNs made them a promising and widely applicable platform for diverse biomedical applications including bioimaging for diagnostics,[88] biosensing, [154] biocatalysis. [155] Moreover, MSNs have also emerged as appealing candidates for drug delivery.[156-158] MSNs with a particle size in the nanoscale range can accumulate in tumor tissues via the EPR effect.[159] In addition, specific drug delivery have been achieved via active targeting by decorating MSNs with targeting ligands such as FA.[84]

1.7.3.1 Synthesis and functionalization of MSMs

Since the 90's, mesoporous silica materials with different mesophases have been synthesized by varying experimental conditions such as pH, temperature, templates and molar ratios.[160,161] MCM-41 and SBA-15 are two of the most extensively investigated products, exhibiting a 2D hexagonal mesopore arrangement and differing for pore sizes, including 2-5 nm and 5-10 nm, respectively. Both types of MSN materials have found applications as drug delivery devices.[162-165]

Generally, the synthetic route to MSNs is based on cooperative self-assembly of silica precursors around a cationic surfactant template under basic conditions. It was proposed that the organic surfactant self-organizes into an hexagonal structure acting as template introducing the well-defined and uniform mesopore morphology, and the silica precursors co-condense with the cylindrical micelles to form MSNs (Fig. 9).[166] In a typical surfactant-silica precursor interaction, tetramethyl- (TMOS) or tetraethyl-orthosilicate (TEOS) is normally added as silica precursors, and cationic alkyltrimethylammonium salts (*i.e.* hexadecyltrimethylammonium bromide, CTAB) are used as templates under a basic reaction condition (NaOH orNH_4OH solution). In order to gain access to the pores, the templating surfactant molecules have to be removed, once the particles is formed. This can be achieved either by calcination or extraction methods.[166]

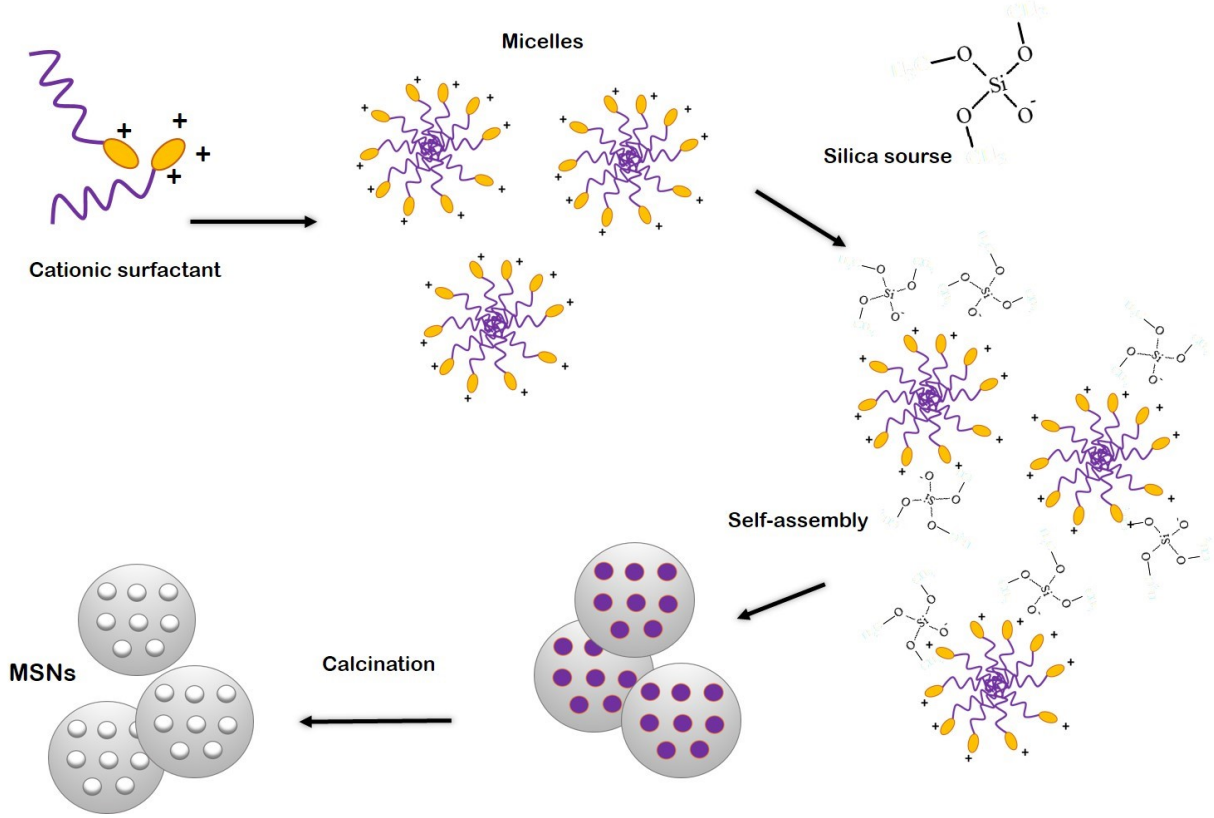

Figure 9: Synthetic scheme of MSNs.

Recent studies have further demonstrated that the porous structure of MSNs could be determined by controlling the relative amounts of silica source and surfactant molecules in the reaction mixture.[167] A variety of strategies have been proposed to achieve tunable pore sizes from less than 2 nm up to 30 nm, including the adjustment of the hydrocarbon chain length of the surfactant templates.[168,169]

In order to exploit the whole potential of MSNs for drug delivery applications, it is desirable to add functionality to the silica scaffold. Molecular functionality attached to the surfaces of inorganic silica can dramatically change the properties of the obtained material, which is important in host-guest interactions with the cargo.

The selective modification of the internal pore system and the external particle surface with organic and inorganic moieties is often an essential requirement for these materials to operate as multifunctional drug carriers exhibiting the required features. External surface functionalization is particularly important for colloidal and chemical stability as well as for interactions with the biological environment (i.e. specific cell targeting).[158,170] In general, is possible to achieve functionalization of silica materials *via* post-synthetic grafting [171] and co-condensation [172] reaction.

In order to increase the loading capacity of MSNs for enhanced drug delivery performance or to entrap large guest molecules such as protein or nucleic acid, a process of pore expansion could be necessary. Indeed, one critical drawback of MSN delivery systems is the limited pore dimension of mesopores, which usually ranges from 2 to 5 nm. One of the most used strategy to achieve pore expansion involves the use of hydrophobic pore expander molecules, which are also called swelling agents.[173] The most commonly used are 1,3,5-trimethylbenzene (TMB) and N,N-dimethylhexadecylamine (DMHA).

In addition, to improve the drug delivery action of MSNs is usual to apply controls such as 'gatekeepers' over the pore entrance, to avoid early drug leakage form the pores (Fig. 10). The drugs cannot leave the silica carriers unless the drug-loading system is exposed to external stimuli, such as pH, redox potential, temperature, photo-irradiation, or enzymes, which trigger the removal of the gatekeepers. Different types of gatekeepers have been used such us: metal NPs[174] polymers[175] or macrocyclic molecules such as CyDs.[176]

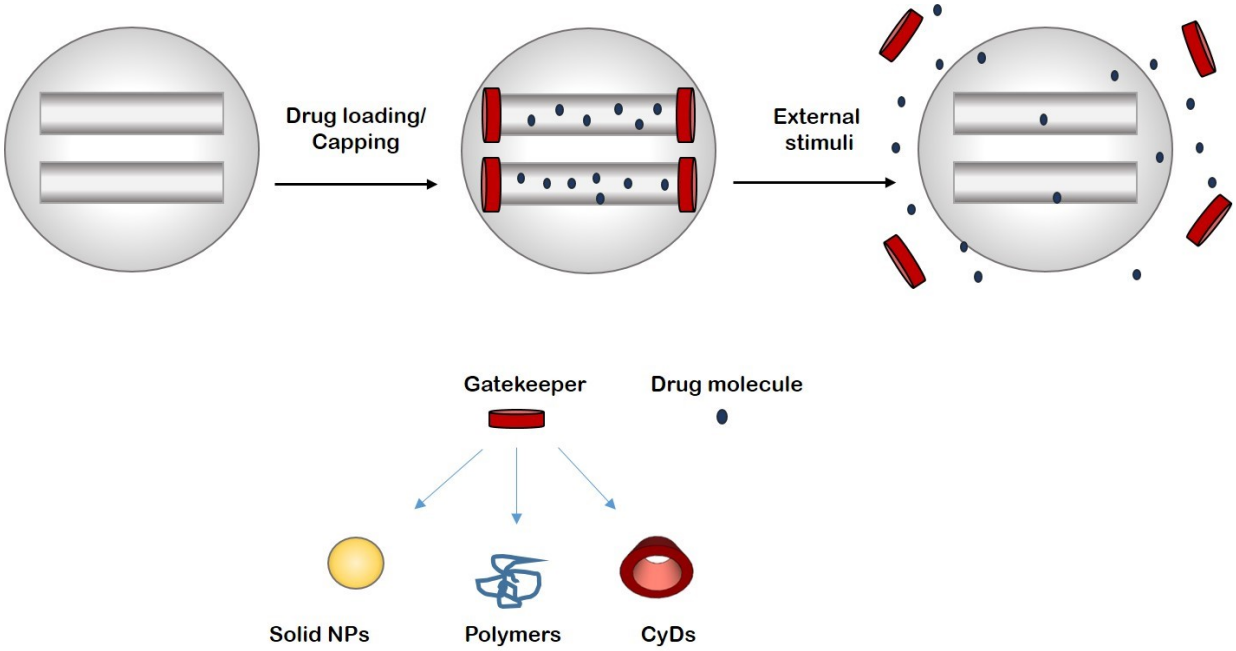

Figure 10 Mechanism of action and classes of gatekeeper

1.7.3.2 Cellular trafficking of MSNs

Many research groups have demonstrated that MSN materials can be efficiently internalized by a variety of mammalian cells, including cancer cells and non-cancer cells[174,177,178] Particles have been found to enter cells through endocytosis pathways in the majority of the cases.[156] Although, thorough understanding of cellular internalization mechanisms has not been fully unveiled.

Several factors have been outlined to influence the kinetics and efficiency of intracellular endocytosis of MSN materials. For instance, it has been found that positively charged MSN materials exhibited better endocytosis efficiency than the negatively charged MSN, owing to a higher electrostatic affinity to the negatively charged cell membranes.[178] In addition, the functionalization with targeting moiety such as folic acid could enhance the uptake efficiency through a folate-receptor mediated endocytosis pathway.[178]

The particle size and morphology also play a key role on the endocytosis of MSNs. Generally, the size of nanoparticles for nanomedical applications should be designed to avoid immediate elimination by the immune system, which occurs more strongly in the larger size than at the lower size. On the other hand, nanoparticles should be larger than 8 nm to avoid fast renal clearance.[179]

Concerning the morphology, it has been demonstrated that rod-shaped particles were more easily internalized into cells compared to spherical counterparts.[180] In addition, Agarwal et al.[181] reported that disc-shaped hydrophilic nanoparticles were internalized more efficiently than nanorods. Interestingly, larger nanodiscs and long rods had higher uptake compared with the smallest particles tested. The effect of shape and size is manifested through the interplay of three parameters: *i)* contact area or adhesion forces between the particle surface and cell membranes, *ii)* the strain energy required for membrane deformation around the particle, and *iii)* effect of sedimentation or local particle concentration at the cell surface.

It has been recently reviewed[9] that although spherical architecture remains the dominant shape described in literature due to synthesis and testing facilities, non-spherical shape, such as worm-like or other unusual morphologies as needles or disc-shape NPs may become the practice for the next generation of nanocarrier.

Another important issue that make a nanovector a good therapeutic agent is its externalization after the accomplishing of its action. Unfortunately, despite the verified biodegradability of silica,[182] the issue of complete and safe excretion of MSNs from the biological system after fulfilment of their diagnostic and therapeutic functions has not yet been entirely addressed, remaining one of the major obstacles impeding their potential clinical translation as nanomedical tools.

Control on the fate of the nanocarrier once internalized in the cells is of focal importance in order to avoid toxic bio-accumulation phenomena. For this reason, a lot of effort has been devoted to investigate the degradation of the particles inside the cells.[183-186]

To enhance the degradation and consequently decrease the toxicity of nanocarriers, a useful strategy could be to dope them in order to respond with a self-destructive behavior to stimuli present in the intracellular environment once reached the target. [187-190]

An example of this approach are redox-responsive disulfide -based systems, being S-S, one of the most cleavable linker from intra/extracellular redox reactions.[191,192] Several materials have been reported in the literature in which S-S cleavable bonds were introduced into framework of the nanoparticles to act as a self-destruction trigger in reducing media, such as: polymeric particles,[95,96] micelles,[97,98] mesoporous silica[99,100] and organosilica[101,102] nanoparticles.

2 AIMS OF THE RESEARCH

The “war on cancer” is now in its fourth decade, since then a lot of efforts have been devoted to the development of novel nanotechnologies in order to reduce cancer mortality. Although localized primary solid tumors can be successfully removed surgically, the treatment of spreading tumors and tumor metastases requires extensive chemotherapy which aims to kill tumor cells or to inhibit their proliferation while preserving the normal cells in the body. However, two main obstacles limit the success of chemotherapy: the lack of tumor selectivity and limited antitumor activity. One of the most important goals of pharmaceutical science is addressing the pharmacological activity of the drug to needed site of action through drug delivery systems (DDS).

In this context, the main aim of this research was to design novel carriers systems for targeted cancer therapy. For this purpose, CyDs were chosen as scaffold to build effective drug carriers exploiting their remarkable properties as solubilizer and stabilizer agents through the formation of inclusion complexes at high stability. Aiming to develop useful tools for active targeting therapy the covalently functionalization with FA as targeting moiety was carried out. Although folate-cyclodextrin conjugates have been already reported in literature, in this doctoral research work for the first time, the FA-conjugates at secondary side of CyD was investigated and compared with the corresponding FA-conjugates at the upper rim of CyD in order to widely explore the different behavior of the 3- and 6- derivatives (Fig 11). In order to explore the targeting ability of these novel CyD carriers antiproliferative assays were performed.

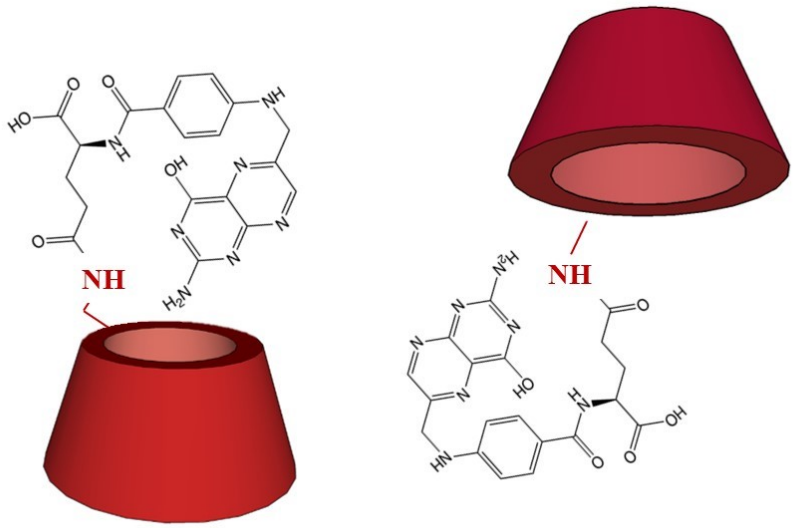

Figure 11: γ regioisomers of CyD3FA and CyD6FA derivatives

Another goal of this work was the development of nanoparticles based on polymers of CyDs which can simultaneously offer the advantages of CyD-type complexation in a synergistic way, resulting more effective than the parent CyDs. Both CyD polymers and oligomers (Fig. 12) differing on the number of CyD cavities in the framework of nanoparticles as well as for the ramification rate were synthesized and functionalized with FA. Furthermore, these systems were tested as delivery vehicles towards different hydrophobic anticancer or anti-inflammatory agents, highlighting the unique inclusion ability of these novel polymeric particles compared with their monomeric counterpart. In addition, the oligomers, may have several advantages respect to their higher MW polymeric analogues.

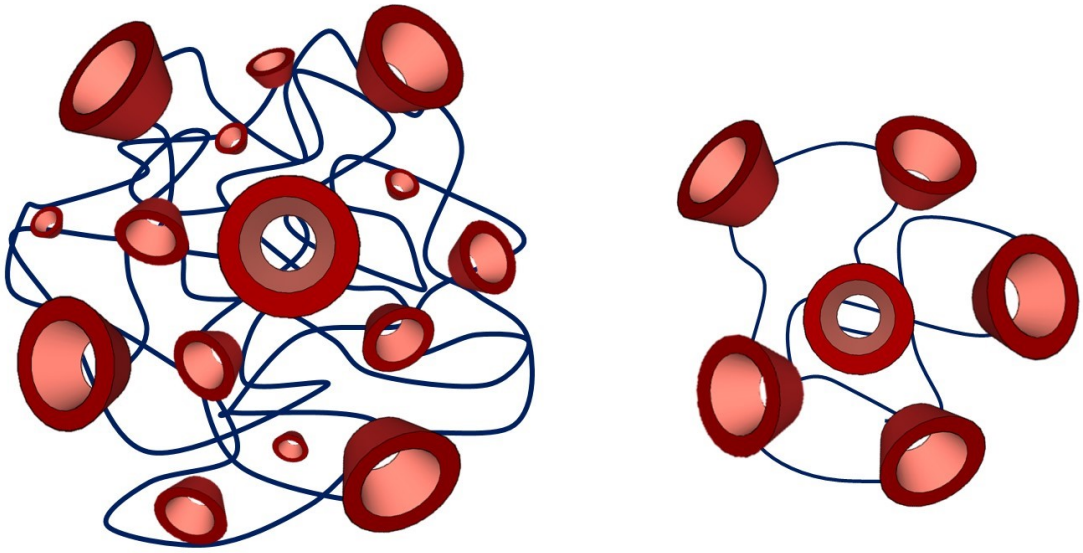

Figure 12: Schematic representation of CyD polymer and oligomer.

Also the field of hard materials was taking into account for the development of novel drug delivery systems and in particular MSNs have been investigated. This study was carried out at the Laboratoire de Chimie et des Biomatériaux Supramoléculaires at the University of Strasbourg under the supervision of the Professor Luisa De Cola. MSNs have attracted great attention due to their intriguing structural properties, such as a high internal surface area and pore volume, tunable pore sizes, colloidal stability and controllable particle morphology. In this context, the attention have been focused on the development of new disc-shaped mesoporous material, the nanodiscs (NDs, Fig. 13), that taking advance of their peculiar morphology were firstly used for the preparation of self-assembled monolayers (SAM), to be employed in targeted cancer cell adhesion and *in-situ* drug delivery. For this purpose, the NDs-monolayers were functionalized with FA as the targeting moiety. Thanks to their large surface area and the possibility of high density of superficial functionalization with bioactive molecules, these systems resulted effective

in binding cancer cells even upon short contact times. Moreover, exploiting the porosity of the synthesized particles, the intracellular release of small hydrophobic molecules pre-loaded in the channels of the NDs were tested.

In addition, in order to highlight the high tendency of these particles to enter within cells, probably thanks to their unusual morphology preliminary biological experiments were carried out to test the cellular uptake of NDs, and the drug-carrier ability were performed.

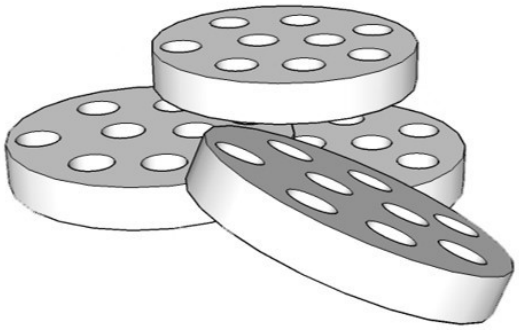

Figure 13: Schematic representation of NDs.

The last aim of this study was to improve the biodegradability of these interesting structures, and for this purpose disulfide-doped mesoporous silica nanodiscs (ss-NDs, Fig.14) was also prepared. Full characterization and preliminary biological assays of these hybrid materials were also performed, and their degradation in redox conditions was investigated.

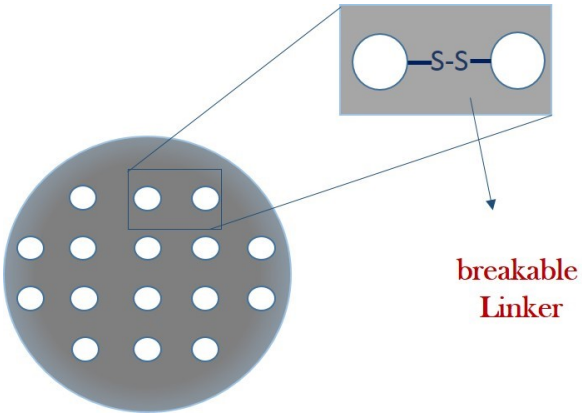

Figure 14: Schematic representation of ss-NDs.

3 RESULTS AND DISCUSSION

3.1 Functionalized cyclodextrins as selective nanocarriers of LA-12

3.1.1 Synthetic aspects

Water-soluble CyD-FA conjugates (Fig. 15) CyD6-FAγ, CyD6-FAα, CyD3-FAγ and CyD3-FAα were synthesized through amide condensation reactions starting from 3A-amino-3A-deoxy- 2A(S),3A(R)-βCyD or 6A-amino-6A-deoxy-βCyD and folate N-hydroxysuccinimide (FA-NHS). It is known that the activation of FA occurs by 80% to the γ-carboxyl group and by 20% to the α-carboxyl group of the glutamate residue.[193] Therefore, the reaction of amino-βCyD and FA-NHS leads to a mixture of two regioisomers with the folate linked either through its α-carboxyl group or its γ-carboxyl group. The CyD-FA regioisomers were isolated through anion-exchange chromatography and fully characterized by ESI-MS, NMR and CD spectroscopy.

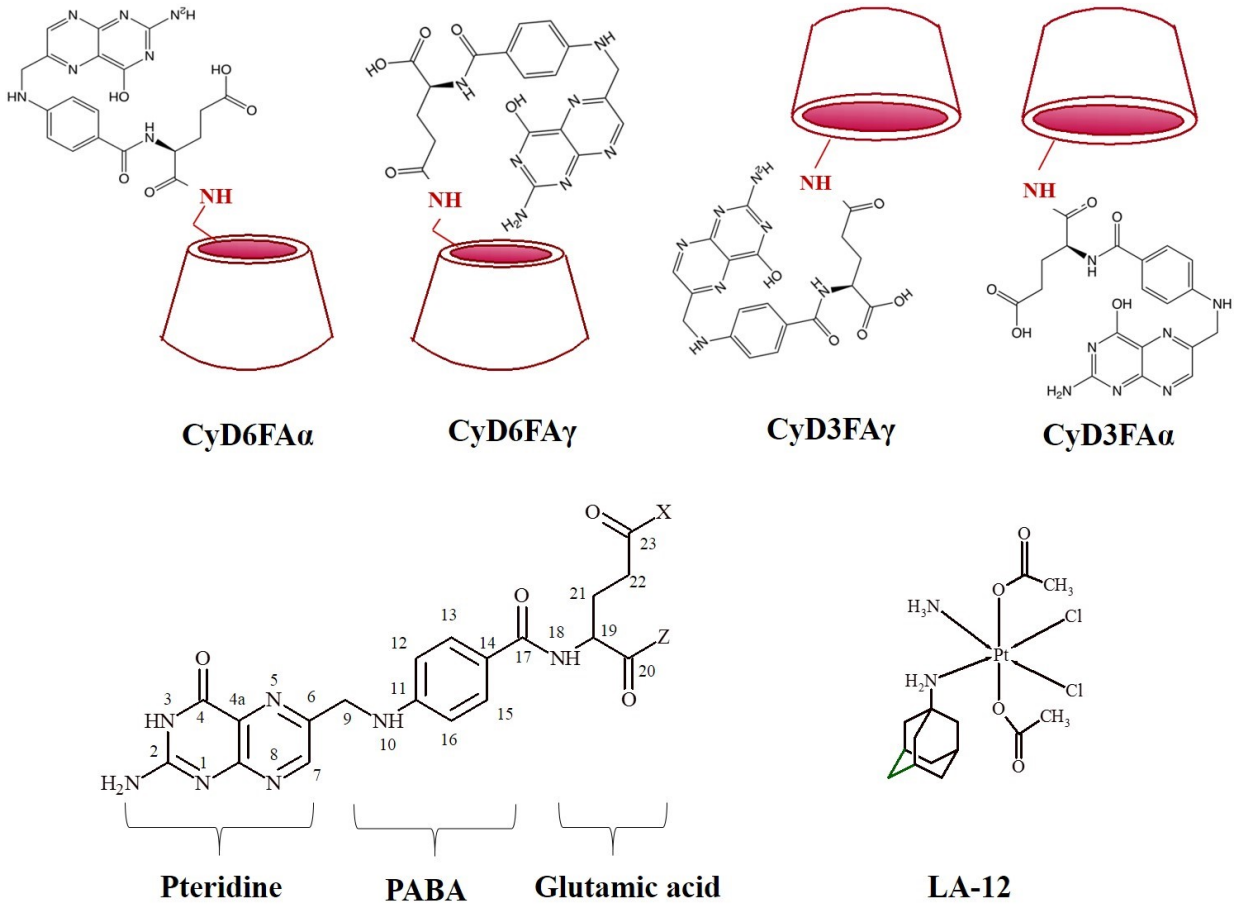

Figure 15: Structures of CyD-FA conjugates, FA and LA-12.

3.1.1.1 NMR spectroscopy

NMR spectra were assigned by 2D COSY, TOCSY, ROESY and HSQC NMR spectroscopy. The NMR spectra were not affected by the CyD-FA conjugates concentration.

<u>*CyD6-FAs*</u>: The ^{1}H NMR spectra of CyD6-FAs are shown in figure 16. In the CyD6-FAα spectrum, the aromatic protons of the p-aminobenzoic acid residue (PABA, Fig. 15) resonate at 6.57 and 7.57 ppm; H-19 resonates at 4.0 ppm whereas diastereotopic Hs-21 resonate at 2.63 ppm and diastereotopic Hs-22 resonate at 1.99 and 2.16 ppm. The Hs-1 of the β-CyD moiety are split into six groups as a consequence of the functionalization, as observed for similar derivatives. [194 , 195] Also the other protons of the CyD moiety are spread upon the functionalization. The diastereotopic 6A protons are shifted upfield (to 2.66 and 3.14 ppm), whereas other 6X protons are shifted upfield or downfield, depending upon the interaction with the aromatic moiety of FA. In particular, two H-6 protons, assigned to the G glucose ring, appear at about 4 ppm. Two H-3 protons (H-3B an H-3X) are shifted upfield at about 3.02 and 2.87 ppm, respectively. The overall trend of the CyD6-FAα spectra suggests the inclusion of the folate moiety into the cavity. Such an inclusion is also supported by the ROESY spectrum (Fig. 18), which shows cross-peak correlations between PABA ring protons and protons H-3 and H-5 inside the CyD cavity. PABA protons also correlate with the H-3B and H-3X protons that are shifted significantly upfield because of the ring current effect. The overall disposition of the FA is such to bring the PABA ring inside the cavity and the pteryl moiety out of the cavity, next to the upper rim.[196] In the spectrum of regioisomer CyD6-FAγ the chemical shifts of the aromatic PABA protons are quite similar to those of the α isomer. In addition, H-9 of FA resonates at 4.25 ppm, Hs-21 at 1.92 and 2.49 ppm and Hs-22 at 2.10 and 2.25 ppm. The signals of the CyD protons are spread over a wider range. Overall, the ^{1}H NMR spectrum suggests the inclusion of the FA moiety into the CyD cavity. Some H-3 protons are shifted upfield and two H-6 protons are shifted downfield because of the ring current effects. Moreover, H-5A is shifted upfield at 3.52 ppm whereas one H-6A is shifted downfield at 4.04 ppm. Also, the ROESY spectrum suggests the inclusion of the chain into the CyD cavity with correlations between PABA protons and CyD inner protons.

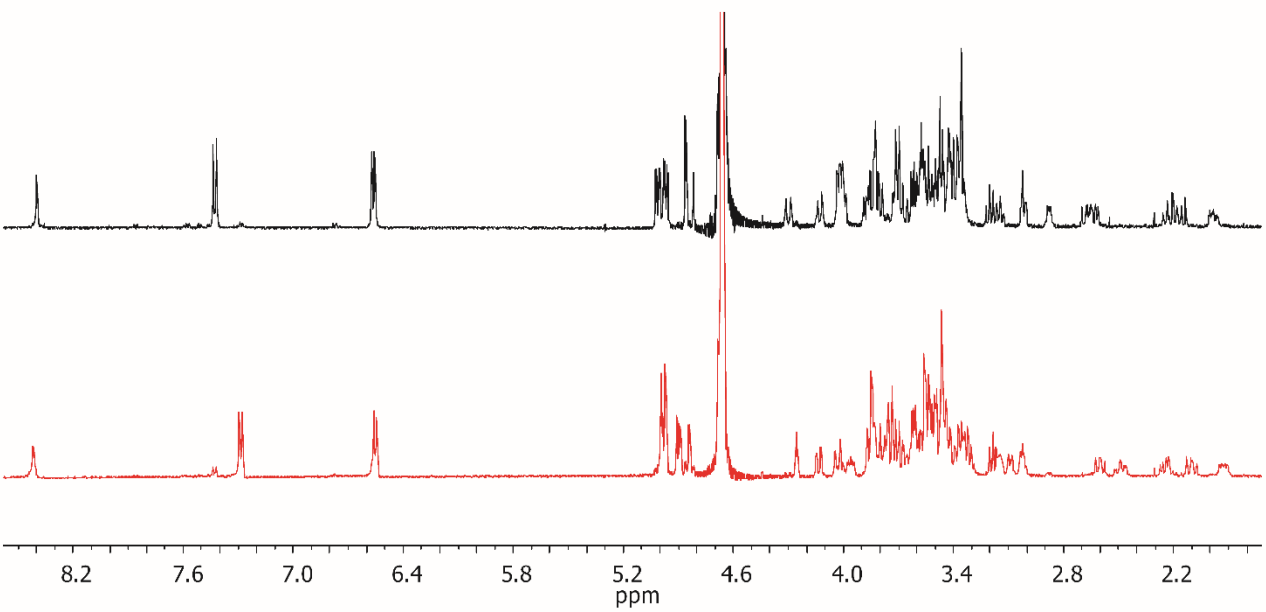

Figure 16: ^{1}H NMR (500 MHz, D_2O) spectra: CyD6-FAα (black) and CyD6-FAγ (red).

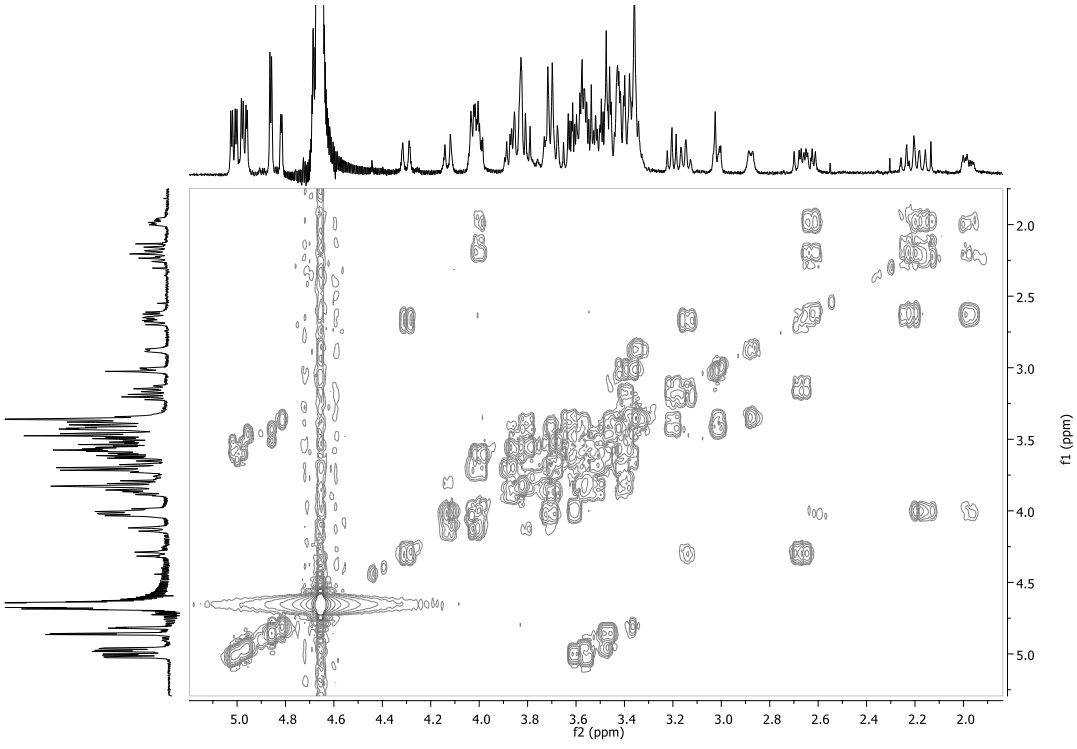

Figure 17: COSY spectrum (500 MHz, D_2O) of CyD6FAα.

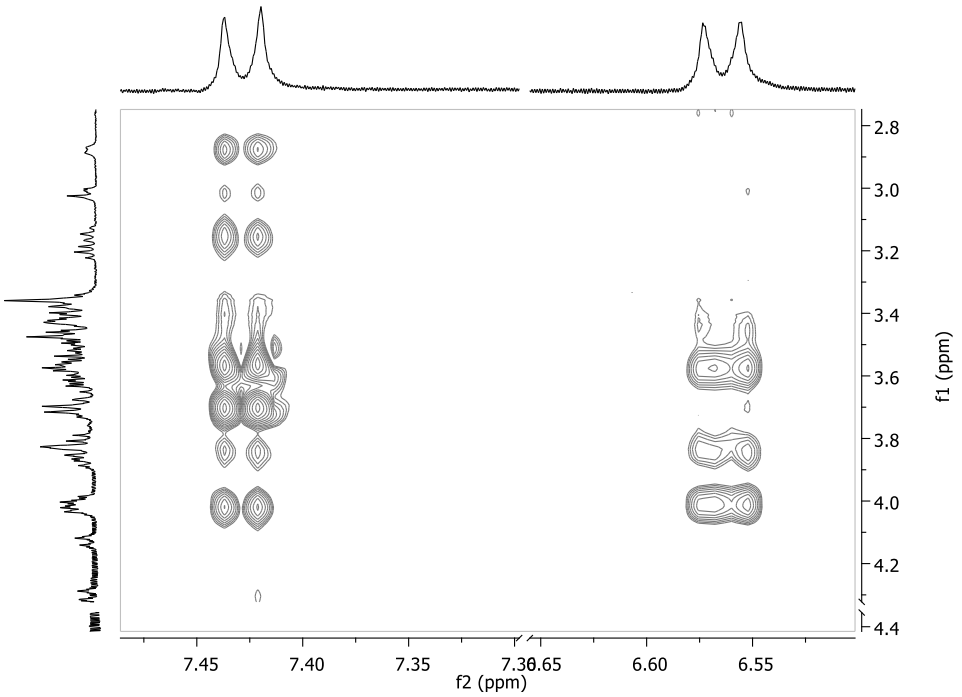

Figure 18: ROESY spectrum (500 MHz, D_2O) of CyD6FAα.

CyD3-FAs: Unlike 6-functionalized CyD6-FA derivatives, the ^{1}H NMR spectra of 3-functionalized CyD3-FA derivatives (Fig. 19) are very different for the α and γ isomers. In the case of CyD3-FAα, the CyD protons are spread in a way quite similar to those of the CyD6-FAs thus suggesting the self-inclusion of the side chain. Of the H-1 signals, only the H-1A could be assigned. The functionalization at position 3 modifies a glucose unit in an altrose residue, thereby increasing the non-equivalence of the sugar units in the NMR spectrum. The $J_{1A,2A}$ value of CyD3-FAα (about 3 Hz) is smaller than the $J_{1A,2A}$ value (about 7 Hz) of the precursor 3A-amino-3A-deoxy-2A(S),3A(R)- βCyD.[197] This suggests that the altrose residue, which is in the 1C4 conformation in the 3-amino-CyD, has a different conformation (4C1 or OS2) in CyD3-FAα because of the interaction with the cavity of the side chain, as reported for similar cases.[198] In addition to the downfield shift of the H-3A proton, as a consequence of the OH substitution by NH, the other two H-3 protons are shifted downfield whereas two H-6 protons are shifted upfield. This trend suggests the inclusion of the aromatic ring, which therefore influences the chemical shifts of CyD inner protons owing to the ring current effect. The ROESY spectrum show cross-peak correlations between the PABA aromatic protons and the inner protons of the CyD cavity, thus confirming the self-inclusion of the FA residue. In accord with a self-inclusion mechanism, the spectra do not depend upon the concentration of

CyD3-FAα in the analyzed sample. Unlike the α isomer, the ^{1}H NMR spectrum of CyD3-FAγ show broad signals with less spreading of the signals. Presumptively the moiety is not self-included owing to the glutamate chain and the wide secondary rim of CyD, but some intermolecular interactions may occur leading to colloidal solutions. Similar colloidal solutions have been reported for related systems.[199]

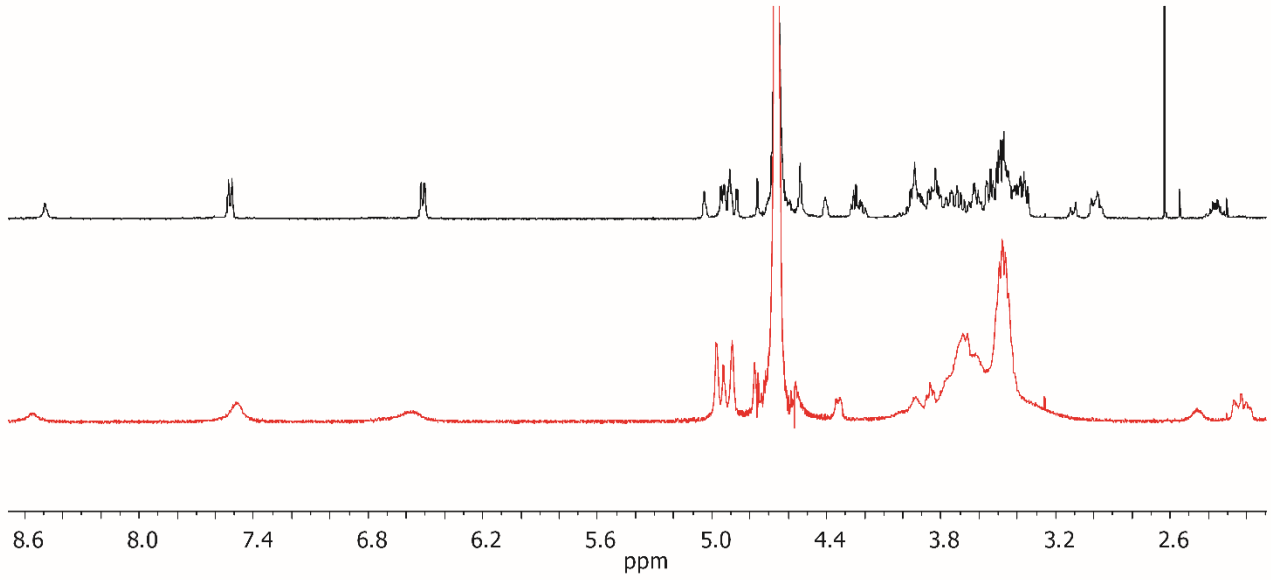

Figure 19: ^{1}H NMR (500 MHz, D_2O) spectra: CyD3-FAα (black) and CyD3-FAγ (red).

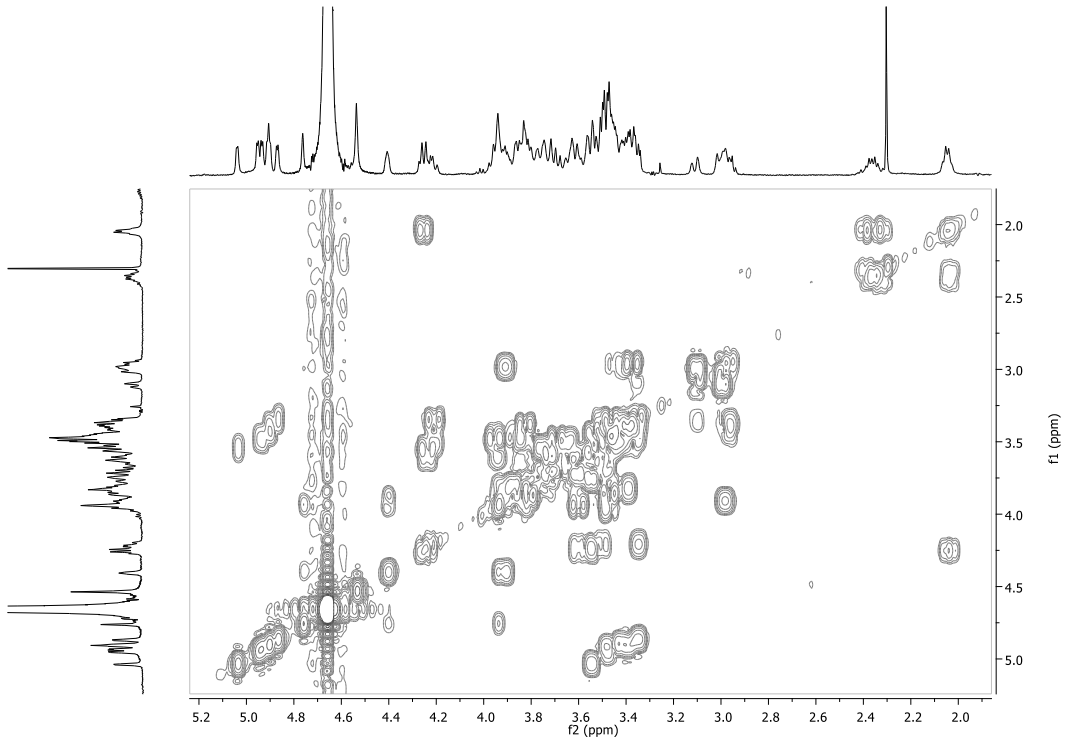

Figure 20: COSY (500 MHz, D_2O) spectrum of CyD3FAα.

3.1.1.2 CD spectroscopy

All compounds were also characterized by CD spectroscopy to further investigate the interaction of FA with the β-CyD cavity.

CyD6-FAs: CD spectra of CyD6-FAs show bands in the absorption region of the folate moiety. The CD spectrum of CyD6-FAγ (Figure 21) is characterized by an intense positive band at 205 nm, two positive bands at 280 and 310 nm and two small negative bands at 230 and 290 nm. A similar spectrum is obtained for CyD6-FAα (Fig. 21 inset dot plot). The intensities of the CD bands in the CyD-FA conjugates are higher than those in free FA. This behavior suggests an interaction of the folate moiety with the cavity in accord with the NMR results.[200] When the competitive guest 1-adamanthanol (ADM) was added to the CyD6-FA solution, the intensities of the CD bands decreased, suggesting the displacement of FA from CyD cavity. This result confirms the inclusion of the folate moiety into the cavity highlighted from NMR experiments.

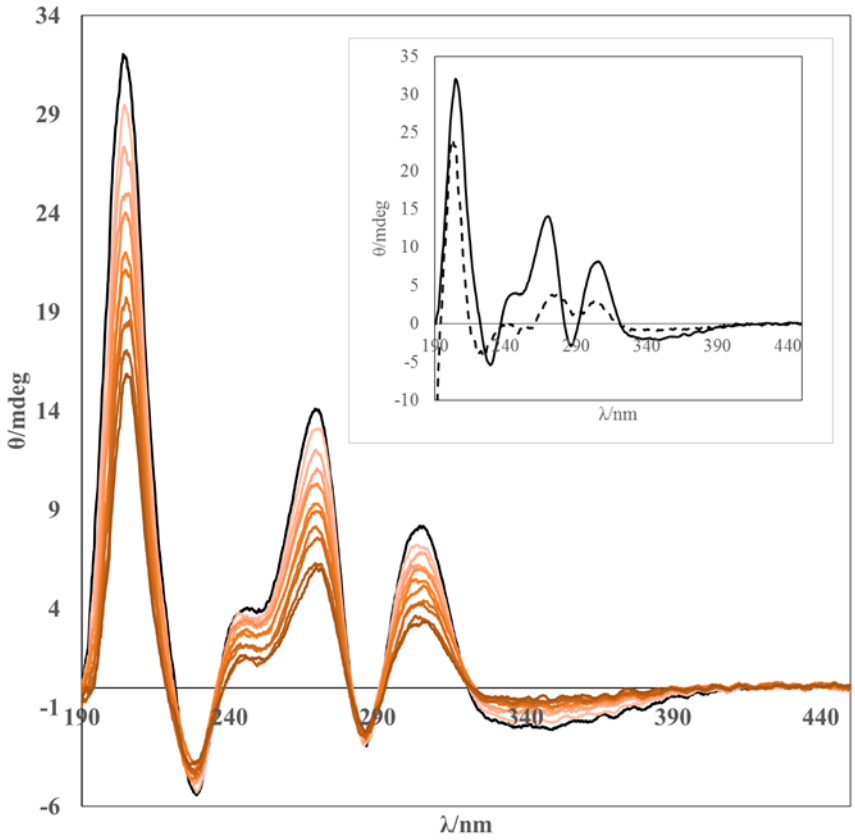

Figure 21: CD spectra of CyD6-FAγ (1×10^{-4} M, black) at increasing concentrations of ADM (red, from 1×10^{-4} to 5×10^{-3} M); inset: CD spectra of CyD6FAα (- - - -) and CyD6FAγ (____) (1×10^{-4} M) in H_2O.

CyD3-FAs: βCyD3-FAα has a CD spectrum resembling that of CyD6-FA (Fig. 22). When ADM was added, the CD spectrum of CyD3-FAα changed significantly and, at high molar ratio (1:10 CyD/ ADM), the CD spectrum became similar to that of free FA (Fig. 22 dot plot in red) in keeping with the exclusion of the folate moiety from the cavity. Differently, the CyD3-FAγ regioisomer has a CD spectrum with weak bands and is very similar to that of free FA (Fig. 22 inset): in particular, two small positive bands at 220 and 290 nm can be observed. This suggests that the folate moiety does not interact significantly with the cavity or has a different orientation in the cavity. Accordingly, the CD spectrum of CyD3-FAγ did not change by addition of ADM.

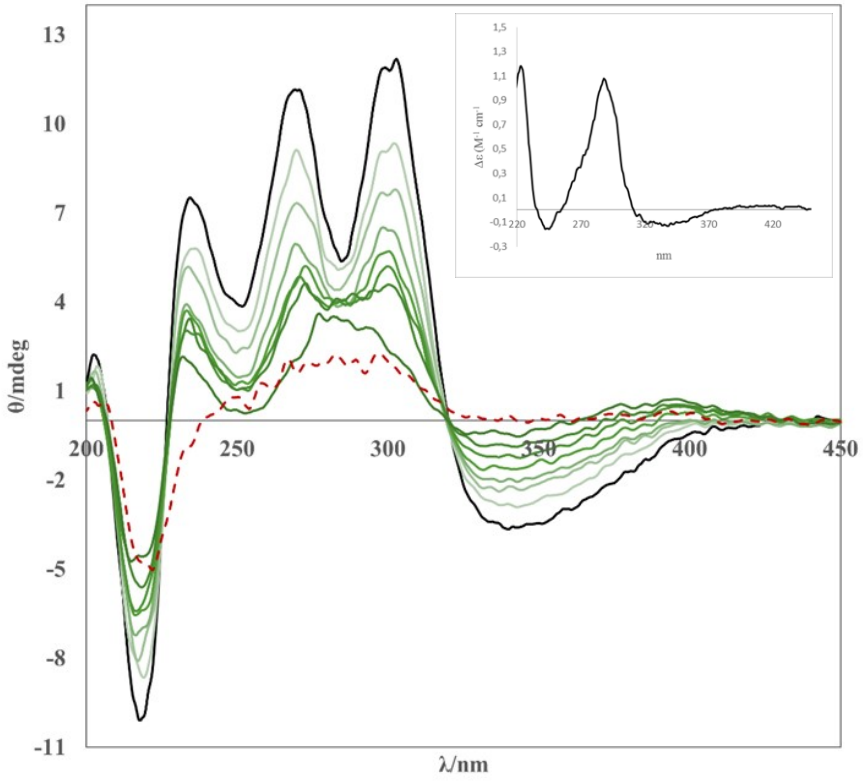

Figure 22: CD spectra of CyD3-FAα (1×10^{-4} M, black) at increasing concentrations of ADM (green, from 1×10^{-4} to 5×10^{-3} M); FA (1×10^{-4} M, red). In inset CD spectrum of CyD3-FAγ.

Probably the different chain length in the α and γ isomers determines a different disposition of the FA moiety in the case of CyD3 derivatives. In the α isomer the chain is longer and the moiety could interact intramolecularly with the cavity. In the γ isomer intermolecular interactions might be preferred, as also suggested by the NMR data.

3.1.2 Interaction of CyD-FA conjugates with LA-12

The ability of CyD‑FA conjugates to form inclusion complexes with hydrophobic drugs was investigated by using the anticancer agent cis-trans-cis[$PtCl_2(CH_3CO_2)_2$(adamantylamine(NH_3)] (LA-12, Fig. 15). LA-12 is an antitumor drug[201] that acts as a pro-drug of cisplatin, this latter represent a cornerstone in present-day chemotherapy. Unfortunately, significant side effects, such as nephrotoxicity, neurotoxicity and tumour resistance, have considerably limited the use of cisplatin in cancer therapy. For these reasons, the development of novel platinum-based cancer chemotherapeutics, active even on cisplatin-resistant cancer types, would be highly desirable. One of the promising new drugs is the complex LA-12 which has displayed a high degree of cytotoxicity against both cisplatin-sensitive and cisplatin-resistant ovarian cancer cells.[202,203] LA-12 has reached phase I clinical trials and its oral dose regimen has been studied in mouse models and in intrinsically cisplatin-resistant ovarian adenocarcinoma.[204] However, LA-12 is poorly soluble in water (0.03 $mgmL^{-1}$), which represents a severe limitation for its administration. The adamantane residue present in LA-12 is known to have high affinity for the β-CyD cavity (Ka of about 5000 M^{-1}).[205] therefore a great number of drugs have been functionalized with adamantane to form inclusion complexes with CyDs. [206] Moreover, the inclusion of LA-12 into CyDs, to obtain a pharmaceutical formulation suitable for intravenous administration, has been patented.[207] A well-known case is that of doxorubicin, although in this case functionalization has led to reduced pharmacological activity.[80] In addition, LA-12 is a platinum (IV) complex rather inert and does not undergo ligand substitution in the presence of FA conjugates as confirmed by NMR spectra.

The inclusion complexes of LA-12 with CyD‑FA conjugates were investigated by NMR spectroscopy through addition of a concentrated dimethyl sulfoxide (DMSO) solution of LA-12 to an aqueous solution of CyD‑FAs. The stability of the inclusion complexes was measured as a function of time. The ROESY spectrum (Fig. 23) showed that the signals of the adamantane residue at 1.90 and 1.60 ppm have cross-peak correlations with the signals in the range 3.90‑3.40 ppm at which CyD protons H-3 and H-5, located inside the β-CyD cavity, resonate. Therefore, the NMR data support the formation of an inclusion complex between LA-12 and the CyD cavity with displacement of the self-included folate moiety.

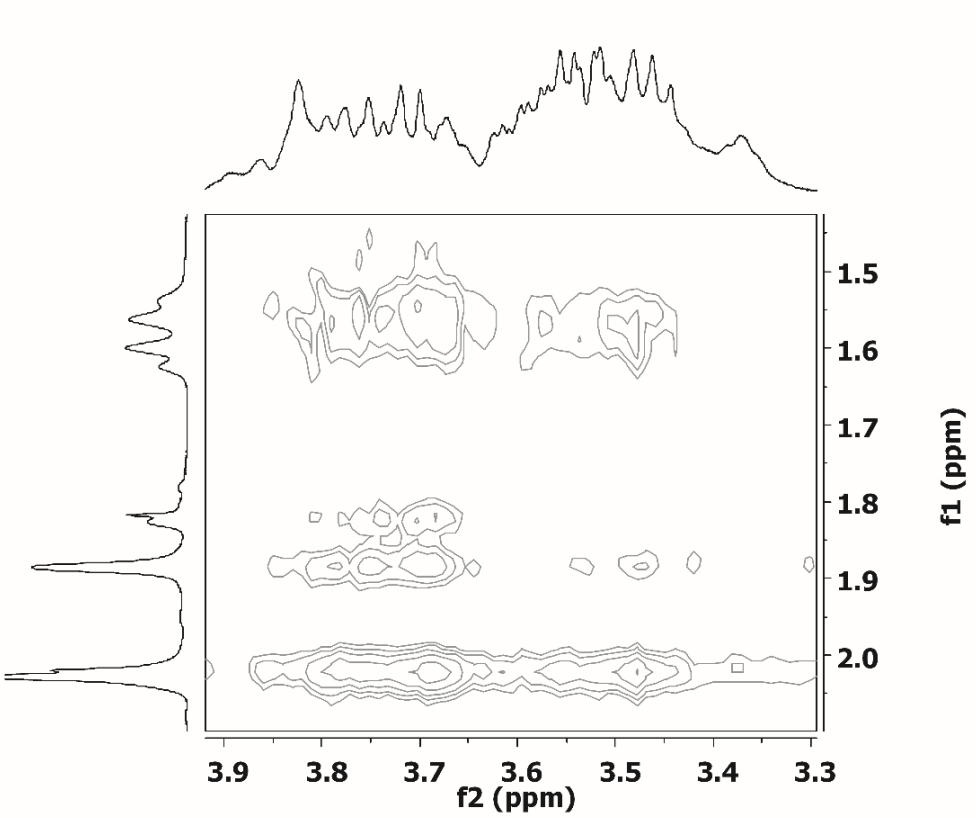

Figure 23: ROESY spectrum (500 MHz, D_2O) of CyD6-FAγ with LA-12.

3.1.3 Antiproliferative activity study (MTT assay)

To verify if the functionalized β-CyDs can favor the cellular uptake of LA-12, we investigated the antiproliferative activity of LA-12 in the presence of CyD-FAs. These measurements were carried out at the Department of Integrated Oncological Therapies, IRCCS AOU S. Martino-IST (Genoa). The inclusion complexes between CyD conjugate and LA-12 were freshly prepared in aqueous solution containing 0.2 % DMSO and at molar ratio of host and guest molecules of 1:1 and 5:1. Furthermore, for this set of experiments only the CyD conjugates at γ position of glutamic chain of FA were assessed, as has been demonstrated that the folate receptor (FR) recognizes folate derivatized at the γ- but not at the α-carboxylate.[75] Cell proliferation assays were performed on cancer cell lines differing in the degree of FR expression. More precisely A2780 (ovarian cancer), MDA-MB-231 (breast cancer) and T47-D (breast cancer) have been employed.[208-210] MCF-7 (breast cancer) cells were used as negative control. The most remarkable results were obtained with MDA-MB-231 cells, for which the IC_{50} values of LA-12 co-administered with CyD6-FAγ (1:5) were notably smaller than those obtained with LA-12 alone or LA-12 co-administered with un-functionalized β-CyD (1:5) (Table 2). The effect of co-administration with CyD-FAs was also observed in the case of

A2780 (with lower degree of FR overexpression), but in less extent than for MDA-MB-231. T47-D cells seemed to be more sensitive to the presence of CyD-FAs than to β-CyD but with a lower cytotoxic activity than that of LA-12. As expected, in the control cell line (MCF-7) no variation in cytotoxicity was observed upon co-administration of LA-12 with β-CyD or CyD-FAs.

The molar ratio between CyD and LA-12 play an important role in the cytotoxic activity. Indeed, when CyD-FAs and LA-12 were administered in a 1:1 ratio, the cytotoxicity of LA-12 did not change. This result is in agreement with the fact that higher concentrations of host molecule with respect to LA-12 (e.g. 5:1), promote the formation of inclusion complexes with higher antiproliferative activity. Possibly higher molar ratios could be necessary to promote the displacement of FA from the CyD cavity, favoring more stable inclusion complexes involving AMA of LA-12 and CyD cavity. These data confirm the ability of the folate derivatives of CyDs to act as targeted drug carriers when the drug can form inclusion complexes with CyDs.

Table 2: Summary of IC_{50} values [μM] of CyD-FAs on human tumour cell lines.

Cyclodextrin conjugates [b]	A2780	MDA-MB-231	T47-D	MCF-7
LA-12	0.59±0.15[a]	2.40±0.45	1.61±0.36	4.29±0.86
CyD3FAγ-LA-12 (1:1)	0.51±0.13	3.02±0.36	1.61±0.41	3.50±0.40
CyD3FAγ-LA-12 (5:1)	0.34±0.15	**0.70±0.11[c]**	1.48±0.11	4.07±0.71
CyD6FAγ-LA-12 (1:1)	0.80±0.22	2.39±0.45	1.99±0.62	4.17±0.62
CyD6FAγ-LA-12 (5:1)	0.29±0.14[d]	**0.84±0.28[f]**	2.45±0.30	5.59±0.49
CyD-LA-12 (1:1)	0.46±0.21	2.20±0.45	3.25±0.23	5.40±0.36
CyD-LA-12 (5:1)	0.58±0.16	2.79±0.20	3.76±0.75	5.52±0.57

The values are the mean ± standard deviation [μM] of 4–7 data points. [a] The ratio CyD/LA-12 is given in parentheses. [b] CyD3-FAγ–LA-12 (5:1) versus LA-12, p=0.005. [c] CyD6-FAγ–LA-12 (5:1) versus LA-12, p=0.010. [d] CyD6-FAγ–LA-12 (5:1) versus LA-12, p<0.001.

3.2 Cyclodextrin polymers and oligomers

The promising results obtained with CyD-FA conjugates as nanocarriers of the anticancer drug LA-12[211] prompted us to extend the investigation to CyD polymers and oligomers, which can offer the advantage of CyD-type complexation in a synergistic way without toxic effects, resulting more effective than the parent CyDs. Different polymeric systems were taken into

account differing in size and consequently in the contents of CyD cavities inside the polymeric structures, and their behavior towards different guest molecules were explored.

3.2.1 Synthetic aspects

For the synthesis of CyD polymers, epichlorohydrin (EPI, 1-chloro-2,3-epoxypropane, Fig. 24) were used as cross-linking reagent for the production of branched CyD polymers. This branching agent is known from past 50 years and is relatively easy to use.[212-214] EPI is a bi-functional agent containing two reactive functional groups, an epoxide group and a chloroalkyl moiety, which can form bonds with CyD molecules and/or itself.

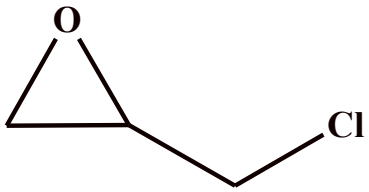

Figure 24: Epichlorohydrin (EPI).

Depending on the requirements of application both highly soluble and water-insoluble polymers (gels, resins) can be produced simply modulating the CyD/EPI molar ratio.[215] Usually the synthesis requires a single step condensation and polymerization reaction. Generally, cyclodextrin polymers were prepared from CyD and EPI in strong alkaline medium requiring a purification step usually through ultrafiltration. The reaction was affected by change in the concentration and amount of NaOH, EPI and CyD used.

In figure 25 are listed the CyD polymers and oligomers synthesized.

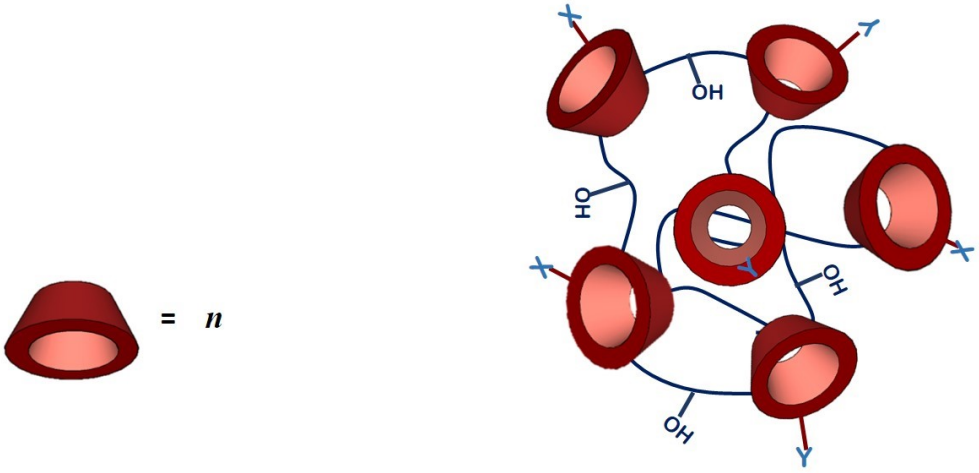

Compounds	X	Y	*n*	X/Y
oCyD	OH	OH	7-8	
oCyDNH$_2$	NH$_2$	NH$_2$	7-8	
oCyDNH$_2$30	NH$_2$	OH	7-8	0.3
oCyDFA	NH-FA	OH	7-8	0.12
pCyD	OH	OH	55-60	
pCyDFA	NH-FA	OH	55-60	0.12

Figure 25: Schematic representation of CyD polymers and oligomers synthesized.

Three novel water-soluble CyD oligomers were synthesized and fully characterized. In particular, oCyD an oligomer of β-CyD units, and two amino-oligomers of β-CyD differing on the percentage of amino groups in the architecture of the oligomers, 30 and 100%, (oCyDNH$_2$30 and oCyDNH$_2$ respectively) were synthesized. oCyDNH$_2$ and a commercial CyD polymer of 90 kDa (pCyD) were also functionalized with FA (oCyDFA and pCyDFA respectively, see Fig. 25) for active targeting purpose.

oCyD was synthesized starting from β-cyclodextrin. The polymerization reaction was carried out under basic conditions using epichlorohydrin (EPI) as a cross-linking agent. The low EPI/monomer ratio (EPI/CyD = 5) ensured the obtainment of an oligomer as reported elsewhere.[134] oCyD was characterized by NMR and light scattering spectroscopy.

The NMR spectrum of oCyD (Fig. 26) gave broad peaks, as typically observed for these class of compounds.[134] The integrated intensities of the signal of Hs-1 of CyD at 5.2-4.8 ppm and the broad signal at 4.2-3.2 ppm provide the ratio of the number of hydrogens of CyDs to that of the cross linker propylenic chains in the oligomer. The obtained value suggests that the oligomer has a CyD content of about 65%.

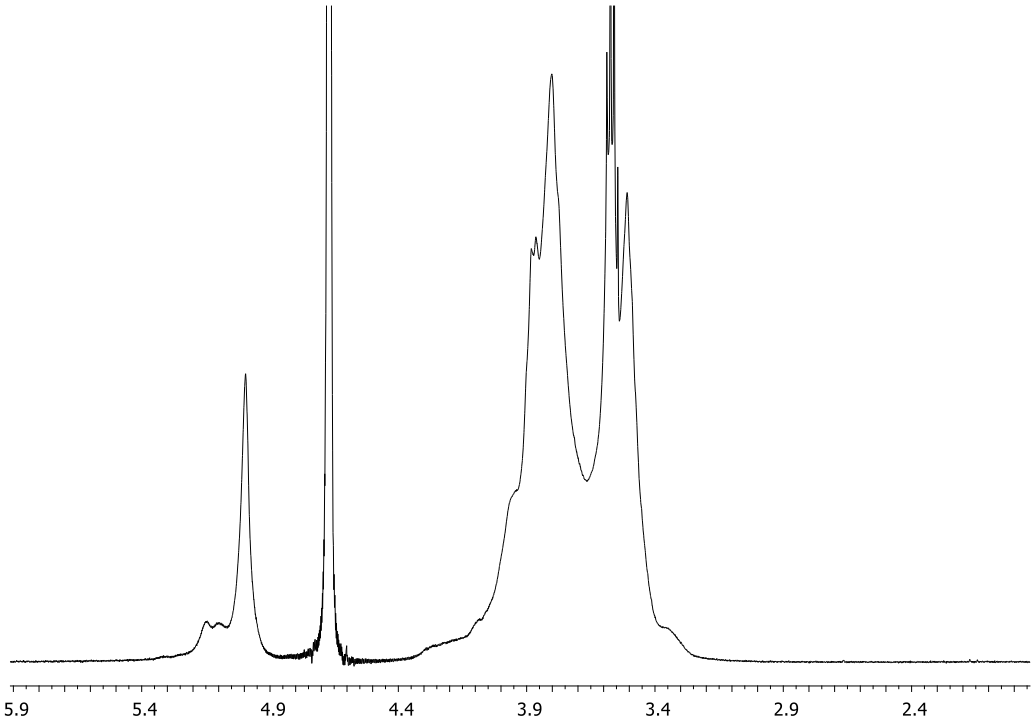

Figure 26: ^{1}H NMR spectrum (500 MHz, D_2O) of oCyD.

DLS measurements show that oCyD forms stable nanoparticles of about 4 nm diameter (Fig. 27a in red). The weight-averaged molecular weight (Mw) of the oligomer was determined through light scattering measurements. The plot of $Kc/R_\theta P$ *vs.* the concentration of oligomer is shown in figure 27b. The intercept of the straight line was used to determine the Mw value, which was found to be 12 ±1 kDa. This Mw corresponds to an average number of 8 cavities per molecule.

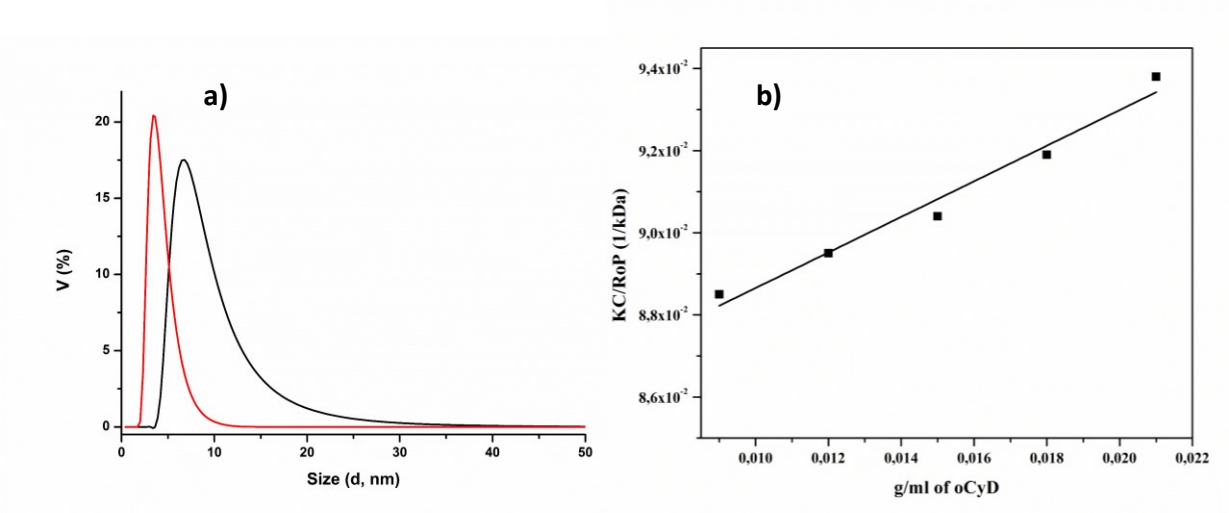

Figure 27: A) Volume size distribution of oCyD (red) and pCyD (black) in Tris buffer pH 7.4 at 25°C; B) intensity of scattered light ($Kc/R_\theta P_\theta$) *vs.* oCyD concentration.

Amino-cyclodextrin oligolymers (oCyDNH$_2$30 and oCyDNH$_2$) were synthesized starting from 3A-tert-Butoxycarbonyl-amino-3A-deoxy-2A(S),3A(R)-β-cyclodextrin (CyD3NHBoc). The polymerization reaction was carried out under basic condition, using EPI. Also in this case a low EPI/CyD derivatives ratio (EPI/CyD3NHBoc = 5) was used in order to obtain an oligomer. In the case of copolymer oCyDNH$_2$30, CyD and CyD3NHBoc (2:1 w/w, respectively) were used. Boc protected 3- amino-CyD was used to avoid the collateral reaction of the amino group with EPI. After Boc deprotection under acid-catalyzed hydrolysis conditions using trifluoroacetic acid (TFA), water-soluble products were purified through ultrafiltration (cut-off 5000 Da) and recovered by freeze-drying process. Their solubility was more than 100 mg/mL. These polymers were characterized by mean of spectroscopic tools such as NMR and DLS.

In the NMR spectra of oCyDNH$_2$ and the Boc protected counterpart peaks are broad, as typically observed for these classes of compounds.**Errore. Il segnalibro non è definito.** In the ^{1}H NMR spectrum of oCyDNHBoc (Fig. 28 in black) the t-butyl protons resonate at 1.45 ppm. Cross-peak correlations between t-butyl Boc protons and CyD protons at 4.2-3.2 ppm can be observed in the ROESY spectra as expected (Fig. 29). Moreover, the Hs of the cross linker chains can be identified in the region around 3.46 and 3.50 ppm together with the broad signal of CyD protons. In the ^{13}C and HSQC spectra is possible to identify the carbons of cyclodextrins as well as those of the cross linker chains (CH and CH$_2$ at 71.8 ppm and 80.5 ppm respectively) (Fig. 30). The integrated intensities of the signal of Hs-1 of CyD and the broad signal at 4.2-3.2 ppm provide the ratio of the number of hydrogens of CyDs to that of the cross linker propylenic chains in the oligomer; this value was used to determine the number of protons of the linker chains in the oligomer. This value suggests that about 70% of CyDNHBoc was contained in the oligomer. The spectrum of oCyDNH$_2$ is very similar to that of the Boc protected oligomer. The signals due to the t-butyl group disappeared in the spectra as expected. In the case of oCyDNH30Boc (Fig. 28 in red) the integral of the peaks confirm the 30% number of cavities containing Boc moiety. NMR characterization highlight the advantage of the synthetic procedure adopted. More precisely, the fine-tuning of molar ratio between the reactants leads to an accurate control of the amount of amino functional moieties inside the architecture of the oligomer.

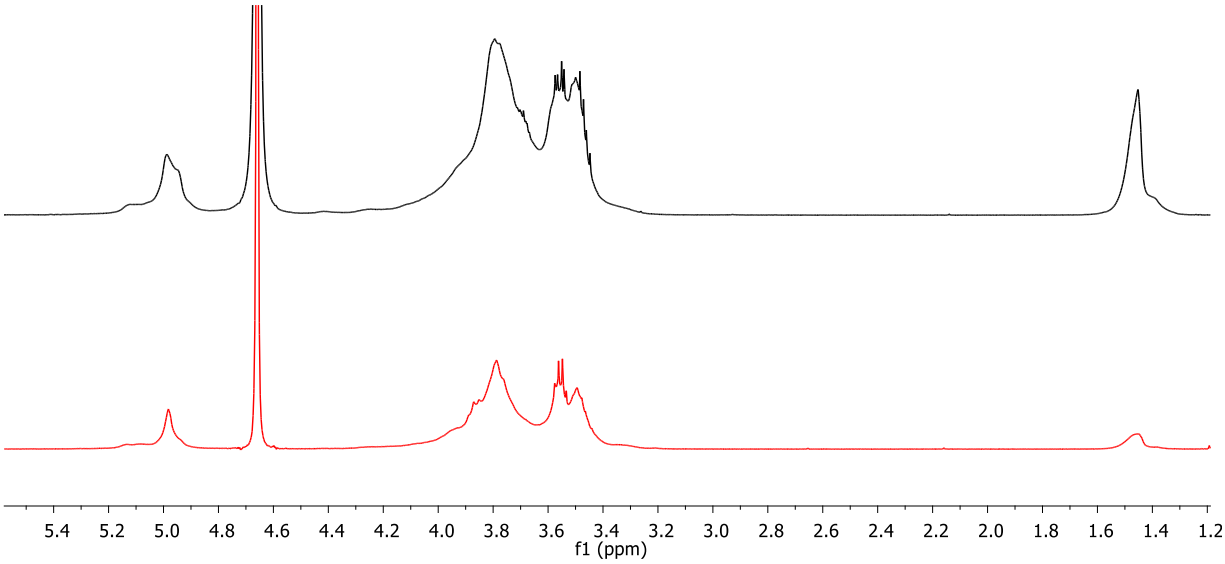

Figure 28: ^{1}H NMR (500 MHz, D_2O) spectra: oCyDNHBoc (black) and oCyDNH30Boc (red).

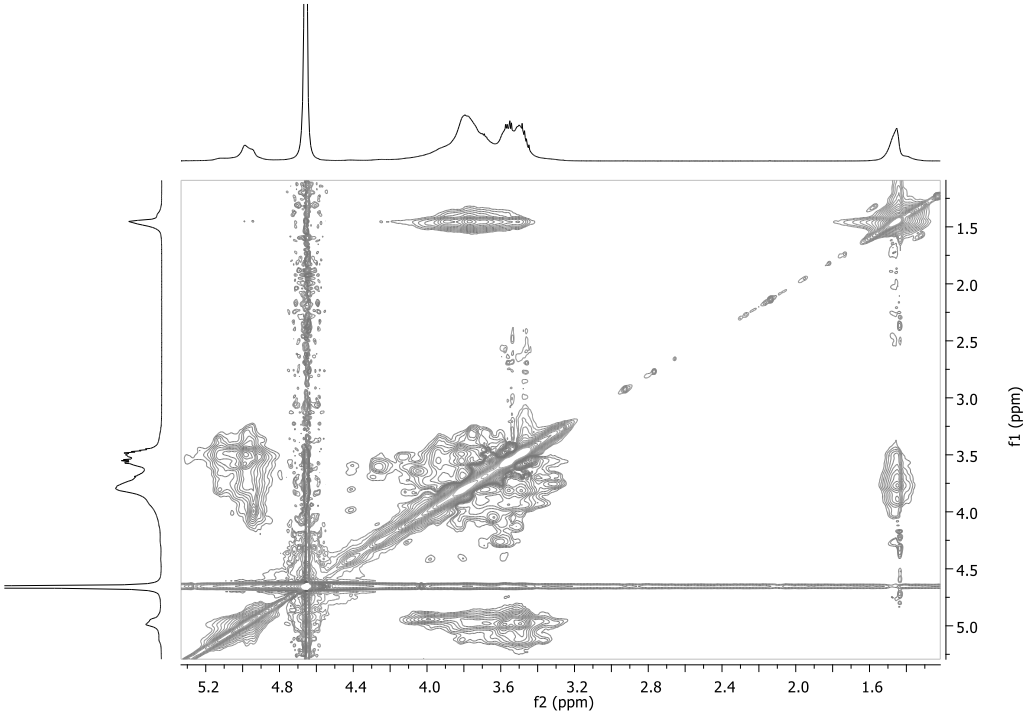

Figure 29: ROESY spectrum (500 MHz, D_2O) of oCyDNHboc.

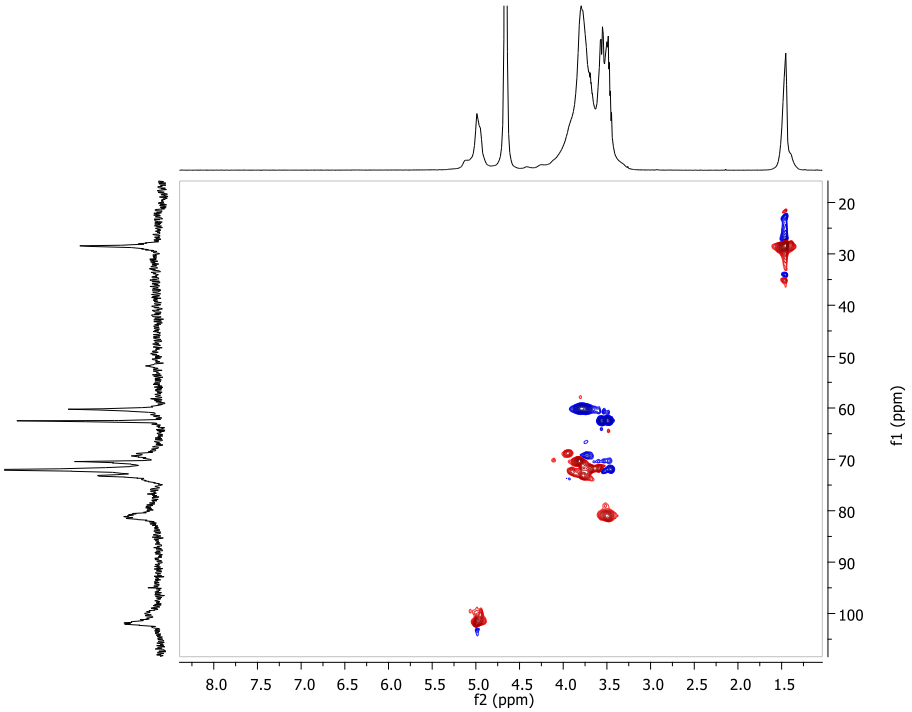

Figure 30: gHSQC spectrum (500 MHz, D_2O) of oCyDNHBoc.

DLS measurements showed that oCyDNH$_2$ derivatives form stable nanoparticles of about 3 nm diameter (Fig. 31b). The ζ potential values were measured and the values obtained were in agreement with the protonation state of the amino groups at different pHs (Fig. 31c). The weight-averaged molecular weight (Mw) of the oligomer was determined for oCyDNH$_2$ through light scattering measurements. The best set of data was obtained in the case of oCyDNHBoc. The Boc deprotection does not modify the number of cavities in the oligomer and thus the Mw was determined for oCyDNHBoc. The plot of $Kc/R_\theta P$ vs. the concentration of oCyDNHBoc is shown in Fig. 31d. The intercept of the straight line was used to obtain the Mw value, which was found to be 12 ±1 kDa.

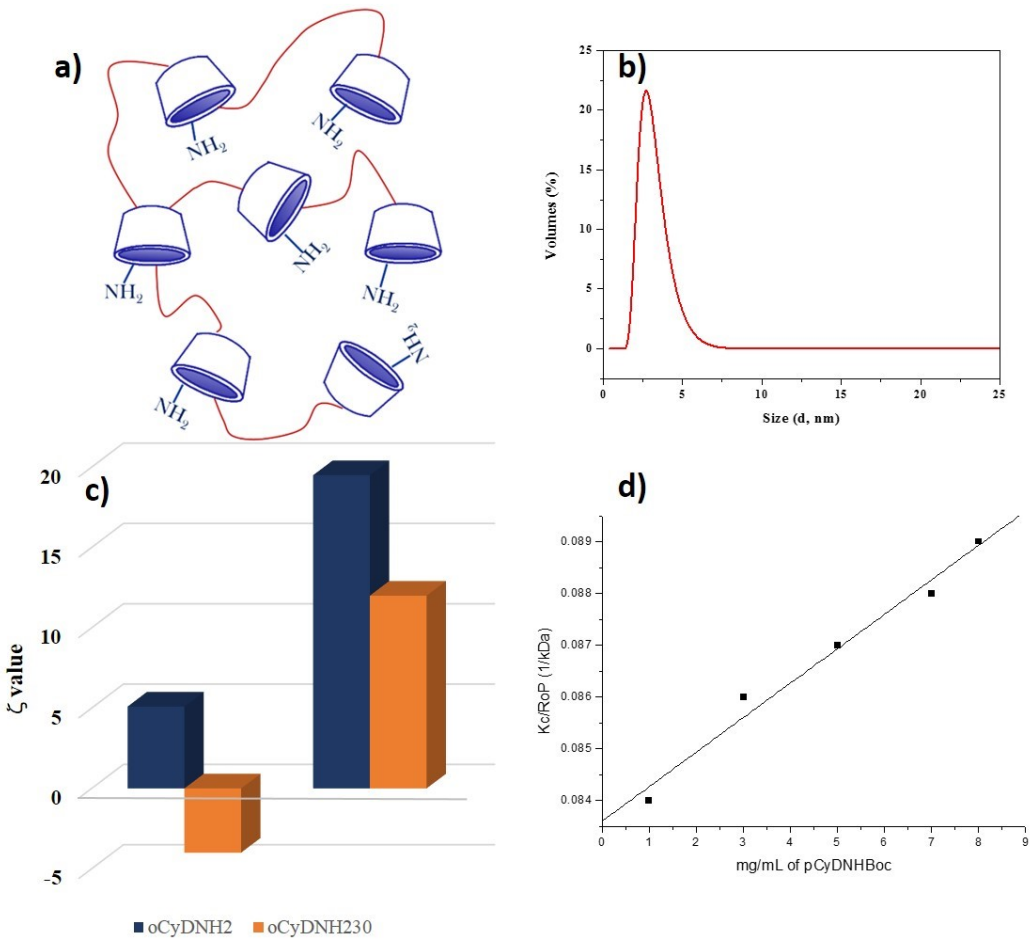

Figure 31: a) Schematic representation of the synthesized oCyDNH$_2$; b) size distribution of oCyDNH2; c) ζ potential at neutral and acid pH values measurer for oCyDNH$_2$ and oCyDNH$_2$30; d) Intensity of scattered light (Kc/R$_0$P) *vs.* pCyDNHBoc concentration.

An average number of about 8 cavities can be hypothesized on the basis of the 70% of CyDNH$_2$ in the oligomer obtained from NMR data and the Mw of 12 kDa. The weight-averaged molecular weight of oCyDNH$_2$ can be calculated by subtracting the molecular weight of the Boc groups and the estimated value is about 11 kDa.

To synthesize amino-polymers, a commercial CyD polymers (pCyD) of 90 KDa and forming nanoparticles of 8.5 nm (Fig. 27a in black) was tosylated using the same procedure used for the synthesis of 3-tosyl-β-cyclodextrin.[216] The tosylate was not isolated and was converted into an amino group, according to the synthetic procedure reported for 3A-amine-3A-dideoxy-2A(S),3A(R)-β-cyclodextrin.[197]

Both the amino polymer and the amino oligomer, previously discussed, were functionalized with FA-NHS using the same condition discussed for monomeric amino-CyDs and purified by dialysis.

The ^{1}H NMR spectrum of pCyDFA (Fig. 32) shows broad bands as typically found in the case of CyD polymers. The aromatic protons of a pterine and PABA moieties of FA resonate in the aromatic region of the spectrum, the peaks are broad in comparison to that of folic acid alone. From integration of the signals of the folic acid moiety and that of the H-1 cyclodextrin protons it is possible to estimate that 12-15% of CyD cavities were functionalized with folic acid. Similar amount of FA was found when oCyDNH$_2$ was used as scaffold for the conjugation with FA.

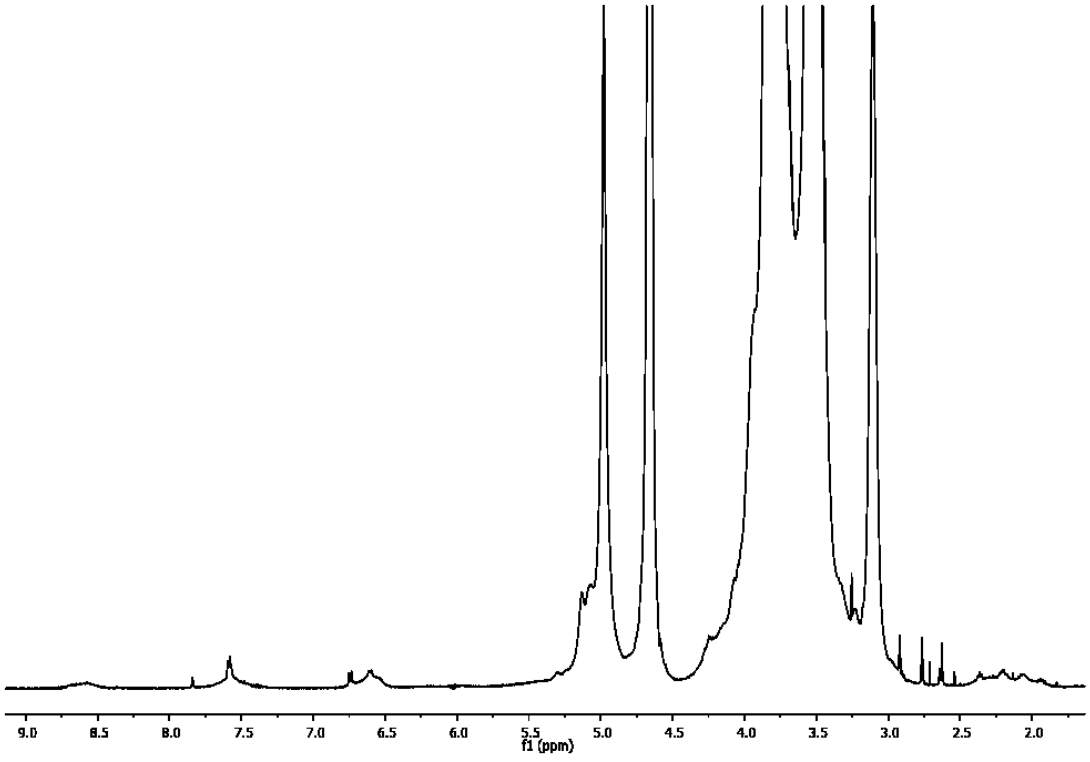

Figure 32: ^{1}H NMR spectrum (500 MHz, D$_2$O) of pCyDFA.

3.3 Cyclodextrin polymers ad oligomers as nanocarrier for anionic drugs

oCyDNH$_2$ (Fig. 31a) bearing amino groups that are ionizable as function of pH values, could be suitable tool as delivery systems towards negatively charged drugs. The occurrence of electrostatic interaction could support the formation of a more stable host/guest inclusion complex. For this purpose, the inclusion ability of oCyDNH$_2$ towards the well know anti-inflammatory agent diclofenac (DCF, Fig. 33) was investigated in neutral aqueous solution by mean of spectroscopy (CD and UV/Vis) and nano-isothermal titration calorimetry (ITC). In particular, the latter technique allowed for the determination of the binding constants and the

energetics of the complex formation by direct measurements of the reaction heats thus providing a complete thermodynamic characterization of the host-DCF systems.

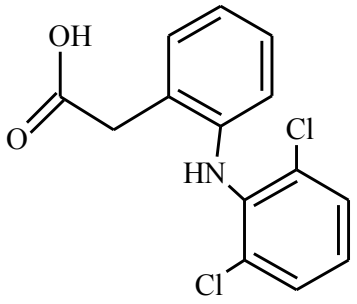

Figure 33: Chemical structure of diclofenac (DCF).

3.3.1 CD spectroscopy

The inclusion ability of $oCyDNH_2$ for DCF was investigated by CD spectroscopy. β-CyD, an uncharged and soluble commercial CyD polymer (pCyD) and oCyDNHBoc were also tested for comparison. Figure 34 shows the induced CD (ICD) spectra obtained when DCF was added to a $oCyDNH_2$ solution at pH 7.4. The spectra show a negative band at 285 nm and a positive band at 310 nm. The intensity of the bands increased when the guest/host molar ratio increased thus suggesting that DCF can interact with the oligomer. The ICD spectra obtained in the presence of either β-CyD, pCyD or oCyDNHBoc were recorded and shown in figure 35. For an easier comparison among hosts which have a different number of cavities, CD spectra were carried out at the same concentration of CyD cavities in the samples. The highest intensity of the CD bands was observed in the case of $oCyDNH_2$. This is about twice the intensity detected for the DCF-pCyD system. Indeed, when oCyDNHBoc was used as the host, a lower intensity in the CD bands was observed (Fig. 35). The different intensity of the CD spectra suggests that the amino groups play a key role in the inclusion process of DCF.

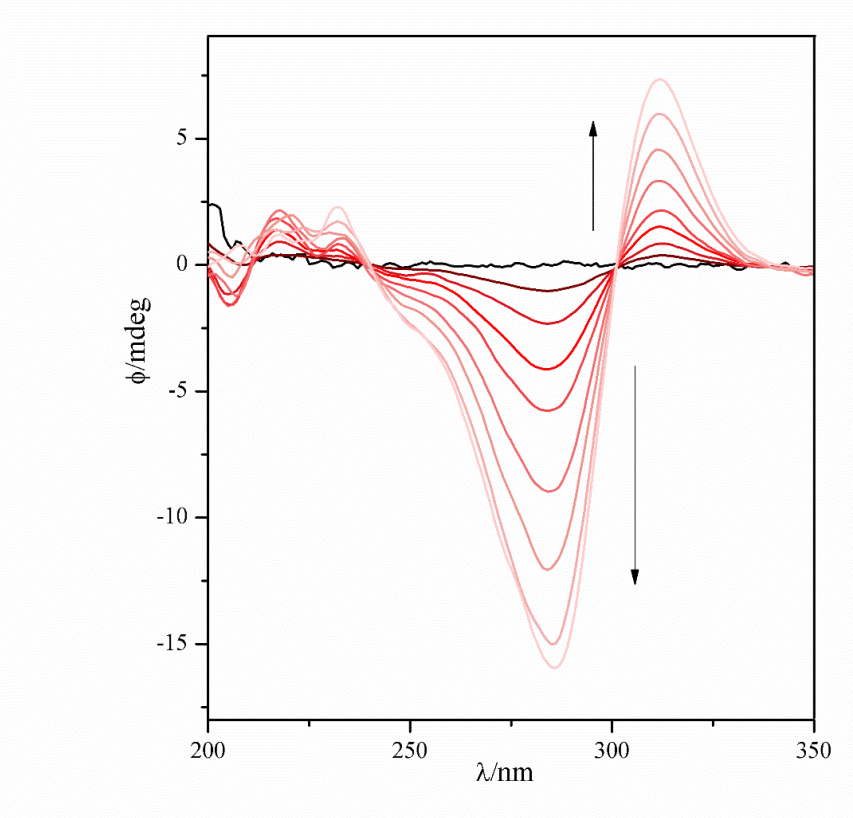

Figure 34 CD spectra of DCF (read from black to light red: 0, 0.5, 1.0, 2.0, 3.0, 5.0, 7.0, 10, 13 × 10^{-5} M) with oCyDNH$_2$ (β-CyD cavity concentration: 1.3 × 10^{-3} M) at pH 7.4 (10 mM Tris buffer).

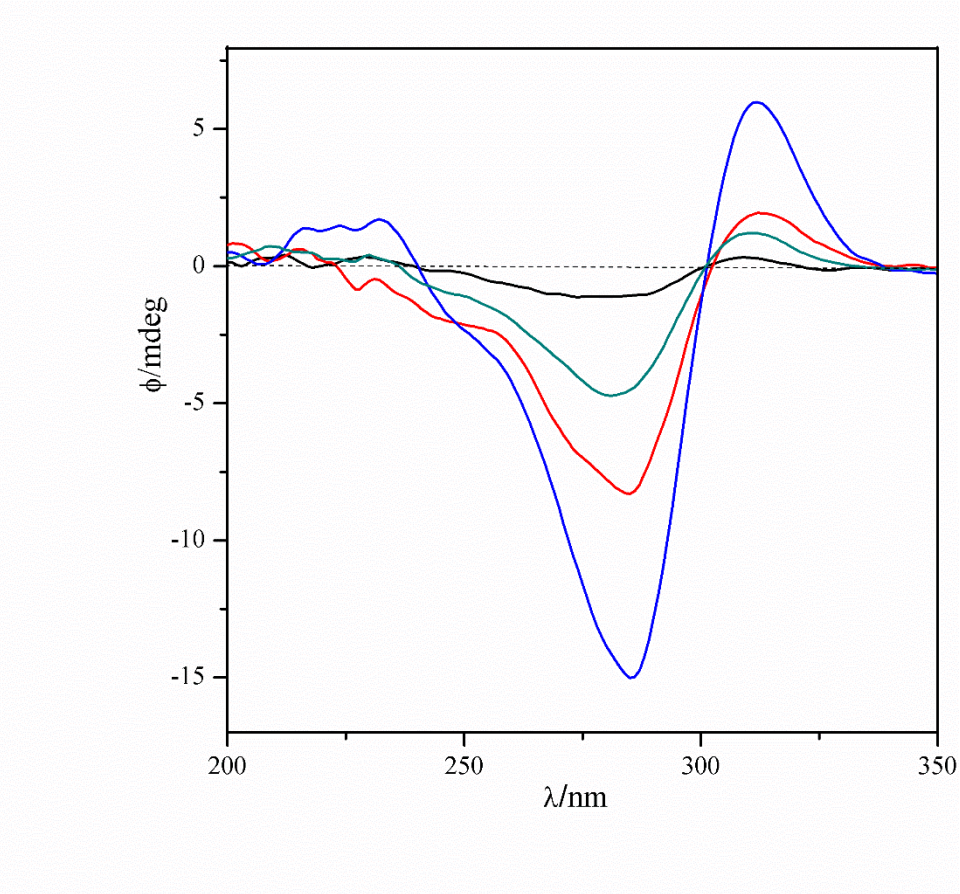

Figure 35: CD spectra of DCF (7.0×10^{-5} M) with different hosts (β-CyD cavity concentration: 1.3×10^{-3} M): oCyDNH$_2$ (black); pCyD (blue); oCyDNHBoc (red); β-CyD (green).

3.3.2 Binding features and thermodynamic parameters

Spectroscopic titrations carried out for the determination of the binding affinity of DCF with either β-CyD (used as a reference compound) or pCyD in neutral aqueous solution (40 mM phosphate buffer, pH 6.9) resulted in changes of the observable which were not appropriate for the determination of binding constant. Consequently, nano-ITC was used as a powerful tool for the evaluation of the energetics of molecular recognition processes in solution.

Calorimetric experiments were carried out in buffered aqueous solution (40 mM phosphate buffer, pH 6.9) to minimize any contribution resulting from the interaction of either the guest or the host with protons.

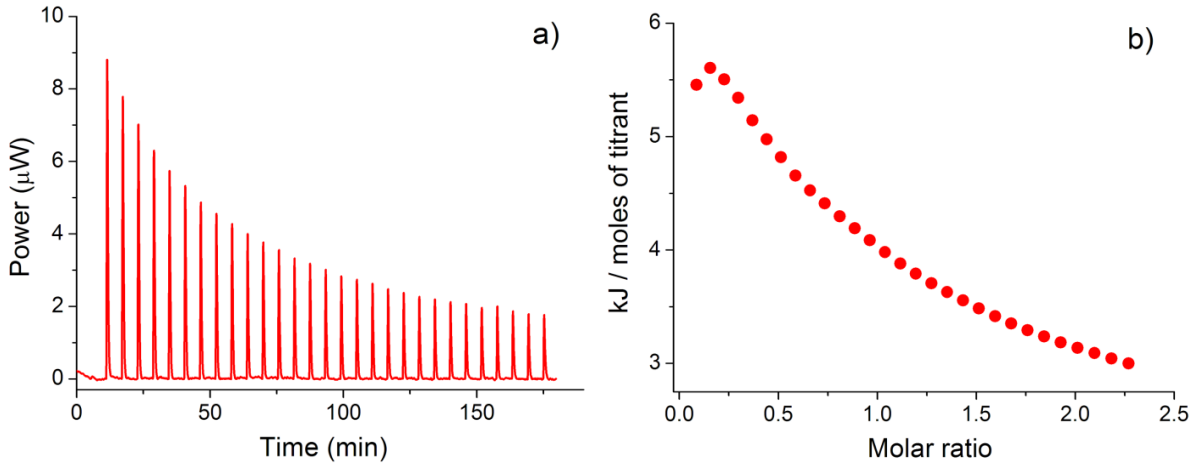

Figure 36: a) Typical ITC titration of diclofenac into pCyD in buffered aqueous solution (pH 6.9) at 25 °C; b) integrated heat data (the molar ratio is referred to the "average β-CyD cavities" concentration of the host).

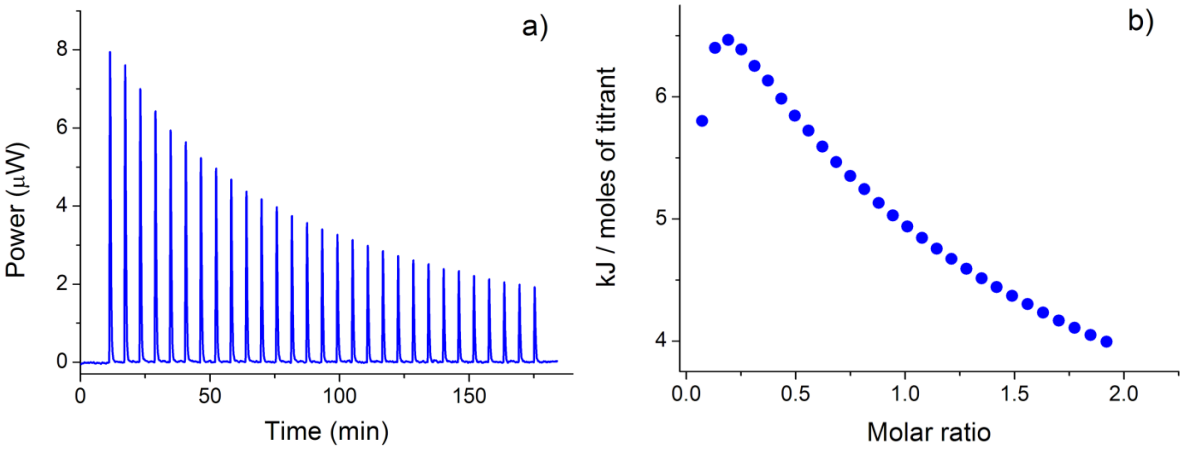

Figure 37: a) Typical ITC titration of diclofenac into oCyDNH$_2$ in buffered aqueous solution (pH 6.9) at 25 °C; b) integrated heat data (the molar ratio is referred to the "average β-CyD cavities" concentration of the host).

Initially, ITC titrations of β-CyD into a DCF solution were run to obtain thermodynamic data to be used as reference values for the study of the binding features of the CyD polymers with the guest under homogeneous experimental conditions. Values found for the DCF-β-CyD 1:1 inclusion complex (see Table 3) are in good agreement with those previously reported.[217] Typical thermograms for the interaction of DCF with pCyD or oCyDNH$_2$ at 25 °C are shown in figure 36 and 37, respectively.

Titrations were carried out by adding a number of equivalents of DCF (used as the titrant) to the host in the ITC sample cell in order to satisfy the saturation fraction criteria proposed for the formation of a 1:1 complex. Usually, a 5 mM DCF solution was used to titrate CyD derivative solutions having a 0.01 - 0.08 mM total polymer concentration. Such small

concentration values emphasize the advantage of nano-ITC technique for the study of binding interactions in solution by using amounts of reactants which are comparable to those commonly employed for spectrophotometric measurements. The simultaneous host-guest equilibria occurring in solution between DCF and the multiple binding sites (cavities) present on the CyD polymer structure make the data fitting process rather cumbersome. Consequently, a simplified model which assumes the formation of a formal 1:1 complex stoichiometry was chosen. For data analysis, the host concentration was expressed as "β-CyD cavity" concentration, calculated on the base of the estimated average Mw and β-CyD % content (w/w) of the polymer. According to this 1:1 complex model, the equilibrium constant is referred to a single host-guest interaction regardless of the number of binding sites (cavities) actually accessible on the host structure. Assuming that all the binding sites for the guest are identical within the polymer, logK values are expected to be nearly comparable along the whole set of cavities, if progressive saturation of the binding sites is not considered. This approach seems reasonable when assuming that, on average, some of the CyD cavities of the polymer will not be fully available or properly exposed for guest inclusion whereas others may act in a cooperative way resulting in a more effective guest binding.[218] As reported for similar multi-site polymeric hosts,[219] when CyD cavity concentration is used as the input value for data analysis, convenient "ΔH° per host site" values (expressed in terms of kJ/mol of host site) may be obtained by the refinement process. On the other hand, the use of the total polymer concentration for data analysis does not take into account the effective number of binding sites of the host and, in the absence of any cooperative effect among the cavities, would provide an "overall enthalpy of complexation" value which should be *n* times that obtained for a single β-CyD unit, with *n* = number of cavities of the polymer. Intriguingly, the value of *n* calculated both for pCyD and oCyDNH$_2$ by simply dividing the "overall enthalpy of complexation" by the ΔH° of formation of the DCF-β-CyD 1:1 complex (-12.69 kJ/mol) is according with with the number of cavities (55-58 and 7-8, respectively) estimated for the two different CyD polymers by DLS measurements (see Table 3).

The logK values and the thermodynamic parameters for the interaction of DCF with pCyD and oCyDNH$_2$ are reported in Table 3. The binding constants of the two CyD polymers, assuming a 1:1 complex stoichiometry, are comparable with that of the complex formed by β-CyD with DCF thus indicating that the polymerization process does not affect the molecular recognition ability of the CyD cavities on the polymer backbone.

Table 3: Stability constant values and thermodynamic parameters for the inclusion of diclofenac in β-CyD, pCyD and oCyDNH$_2$ at 25 °C in buffered aqueous solution (pH 6.9)

Hosts	logK	ΔH° (kJ mol^{-1})	ΔS° (J deg^{-1} mol^{-1})[a]	Number of CyD cavities[b]
β-CyD	2.41 ± 3	-12.69 ± 2	3.6 ± 5	
pCyD	2.8 ± 1	-17.54 ± 8[a]	-5 ± 1[a]	55-58
oCyDNH$_2$	3.47 ± 6	-9.58 ± 2[a]	34 ± 2[a]	7-8

[a] Units are to be intended as "per moles of host site"
[b] Number of cavities estimated by dividing the "overall enthalpy of complexation" by the ΔH° of formation of a single β-CyD-guest complex (-12.69 kJ mol^{-1}).

Similar results has been observed for other drug - CyD polymer systems in which the presence of a macromolecular arrangement does not weaken or negatively influence the stability and efficiency of the inclusion complexes.[220,221] The larger logK value found for the DCF-oCyDNH$_2$ complex may be ascribed to the supplementary contribution provided by the interactions between the negatively charged guest and the amino groups present on the CyD cavities of the oligomer, in addition to hydrogen bonds and van der Waals forces. In fact, the pKa value reported[222] for the carboxylic group of DCF is 4.84 while the amino moieties on the CyD units are expected to be nearly protonated at pH 6.9. On the whole, the favorable combination of different attractive forces makes oCyDNH$_2$ an efficient receptor for the simultaneous complexation of several target guests. The enthalpic and entropic contribution to the free energy term of each host-guest complex are shown in figure 38. The complexation of DCF is enthalpically favored (ΔH°<0) for all CyD derivatives and driven by enthalpy (|ΔH°|>|TΔS°|) for both β-CyD and pCyD and by entropy (although by a small extent) in the case of oCyDNH$_2$.

Factors affecting the thermodynamic parameters due to guest inclusion into CyDs are the result of a balance of several effects: the insertion of the hydrophobic portion of the guest molecule into the CyD cavity, the formation of weak interactions (such as hydrogen bonds, van der Waals and/or electrostatic forces), the desolvation of the guest, the release of water molecules from the CyD cavity and conformational changes of the host upon guest complexation.[223]

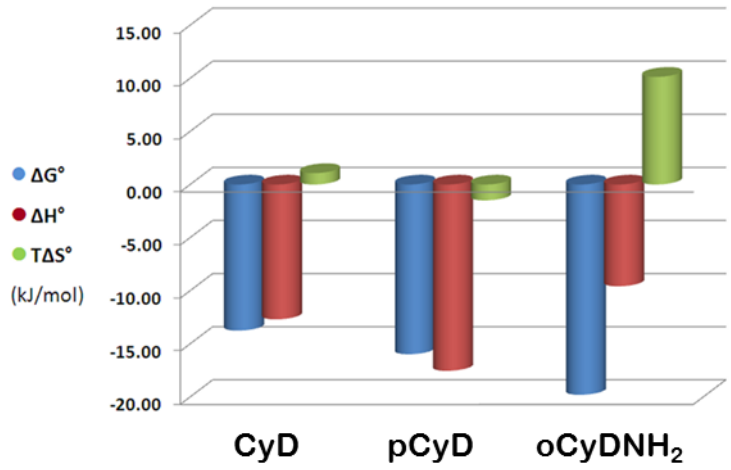

Figure 38: Thermodynamic parameters for the different host-guest complexes at 25 °C in buffered aqueous solution (pH 6.9).

For both CyD polymer and oligomer, a combination of hydrogen bonds and van der Waals interactions between DCF and the CyD cavities triggers the host-guest complex formation. These enthalpically favorable contributions override the cost in energy needed for the desolvation of all the interacting components. However, the differences observed in both the enthalpy and entropy values suggest that the mechanism of binding is slightly different for the two CyD polymers. In particular, the larger amount of cavities of pCyD enhances the enthalpically favorable attractive interactions with the guest resulting in ΔH° value larger than that found both for the shorter oCyDNH$_2$ polymer and the simple β-CyD. On the other hand, the large and favorable ΔS° value obtained for the DCF-oCyDNH$_2$ complex may be ascribed to a combination of *i*. a reorganization of water molecules released upon guest inclusion and *ii*. a significant translational and conformational freedom experienced by this flexible and less constrained polymer when guest molecules are entrapped within its cavities. Such increase of the entropic gain, along with a small decrease of the ΔH° value, has been reported in the literature in the case of similar host-guest complexes employing β-CyD oligo-polymeric structures as multi-site receptors.[219,224]

3.3.3 DFC solubility study

The effect of the oCyDNH$_2$ oligomer on the DCF solubility was investigated at pH 5.5 at 25 °C since the solubility of DCF is very low (about 2.5×10^{-5} M) at this pH value. pCyD and β-CyD were used for comparison. Results of the phase solubility studies are reported in figure 39 that shows the solubility profiles of DCF as a function of increasing concentrations of β-CyD, pCyD or oCyDNH$_2$ in aqueous solution at pH 5.5. The host concentration has been reported as β-CyD cavity concentration for a more appropriate comparison among the different systems.

Interestingly the solubility of the drug increased linearly with the increase of the host concentration. This linear correlation between DCF and host concentration, with a slope < 1, suggests the formation of a 1:1 host/guest inclusion complex with the CyD unit. The solubility of DCF in the presence of either $oCyDNH_2$ or pCyD increases of about 10 times. The oligomer is a slightly more efficient solubilizing agent than pCyD. Interestingly, the length and size of the polymeric chain seem to not improve the solubilizing effect of the polymer in comparison with that of the oligomer.

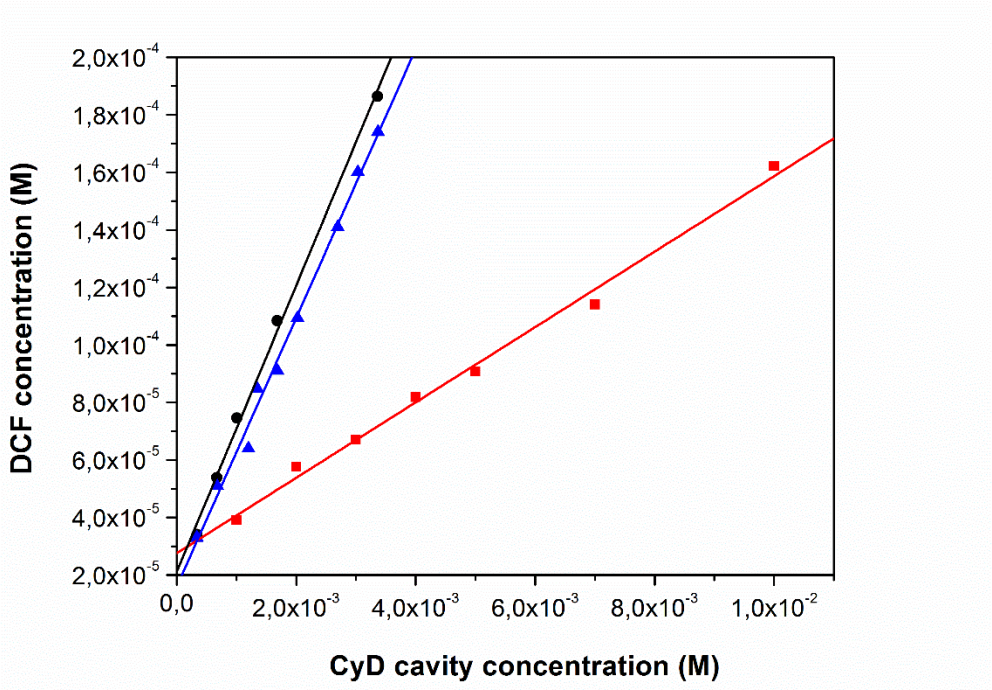

Figure 39: Solubility of DCF *vs.* b-CyD cavity concentration of different hosts at pH 5.5: $oCyDNH_2$ (black); pCyD (blue); β-CyD (red).

3.4 Cyclodextrin polymers as nanocarriers of anticancer agents

Since the well established talent of CyD polymers in the formation of inclusion complexes more effective than the parent CyDs, we tested the ability of these polymeric NPs as drug delivery systems of hydrophobic anticancer agents, improving their water solubility and consequently their bioavailability.

3.4.1 CyD polymers as nanocarriers of LA-12

The inclusion ability of the newly synthesized CyD polymers and oligomers toward the anticancer prodrug LA-12 was investigated by mean of NMR spectroscopy. In particular, oCyD,

oCyDFA, pCyD and pCyDFA (see Fig. 25) were taking into account for this study. Moreover, antiproliferative experiments to test the targeting ability of the FA-functionalized systems were performed.

3.4.1.1 Interaction with LA-12

The water solubility of LA-12 increased markedly both in the presence of the polymer or oligomer, due to its inclusion in the CyD cavity. The inclusion of LA-12 into pCyDFA and oCyDFA was investigated by NMR spectroscopy. The NOESY spectrum of a mixture of pCyDFA and LA-12 is shown in figure 40. The NOE cross peaks between the adamantane protons of LA-12 and the CyD protons confirm the formation of the inclusion complex. A similar behavior was found for oCyDFA.

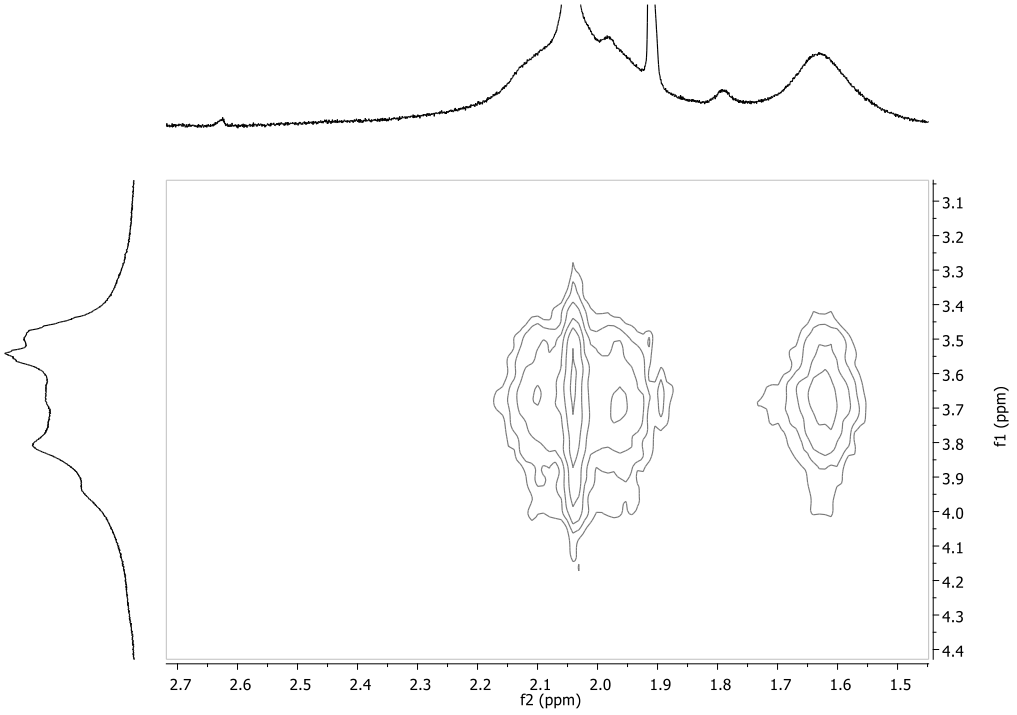

Figure 40: NOESY spectrum (500 MHz, D_20) of pCyDFA/LA-12.

3.4.1.2 Antiproliferative activity study (MTT assay)

Cell proliferation assays were performed on cancer cell lines differing for the degree of FR expression (A2780, MDA-MB-231). MCF-7 cells were used as a negative control. pCyDFA/LA-12, oCyDFA/LA-12, pCyD/LA-12 and oCyD/LA-12 complexes were tested in all the cell lines (Table 4). When the cells were incubated with pCyD or oCyD at 50 μM no

toxicity effect was observed. Toxicity of β-CyD/LA is also reported in table 4 for comparison purposes.

As shown in Table 4, MCF-7 cells did not show a great sensitivity to LA-12 and thus to any of the complexes tested. In A2780 cells, the most sensitive cell line to LA-12, and MDA-MB-231 cells pCyDFA/LA-12 and pCyD/LA-12 complexes were the most active formulation and showed an increased toxicity in comparison to the free drug. IC_{50} values were reduced of 59% and 68% in comparison to LA-12, in A2780 and MDA-MB-231, respectively. The administration of the complex oCyD/LA-12 or oCyDFA/LA-12 did not significantly changed the activity in comparison to LA-12 in A2780 and MCF-7 cells but they shied a slight decrease of IC_{50} values in MDA-MB-231 cell when the oCyDFA or oCyD was in higher molar ratio with respect to LA-12. It is noteworthy that the complex of LA-12 with high molecular weights (pCyDFA and pCyD) are significantly more active than the complexes with CyD oligomers.

Table 4: IC_{50}s (μM) of LA-12/CyD polymers in human tumor cells.

CyD polymers	A2780	MDA-MB-231	MCF-7
LA-12	0.59±0.15[a]	2.40±0.45	4.29±0.86
pCyDFA/LA-12 (5:1)	0.24±0.05[b,c]	**0.78±0.24[d]**	5.55±0.76
oCyDFA/LA-12 (5:1)	0.66±0.18	1.41±0.12[g]	5.62±0.45
oCyDFA/LA-12 (1:1)	0.36±0.13[e]	2.86±0.44	6.91±1.68
pCyD/LA-12 (1:1)	0.44±0.08[e]	**0.67±0.18[d]**	4.04±0.51
pCyD/LA-12 (5:1)	0.34±0.10[f,h]	**0.53±0.07[d,i]**	5.05±1.01
oCyD/LA-12 (1:1)	0.41±0.11	2.87±0.52	7.27±2.42
oCyD/LA-12 (5:1)	0.72±0.25	1.63±0.14[f]	4.53±0.53
β-CyD/LA-12 (5:1)	0.58±0.16	2.79±0.20	5.51±0.57
pCyD	>50	>50	>50

[a] The values represent the mean±SD of 4-10 data. [b] $p<0.001$ vs LA-12; [c] $p<0.01$ vs pCyD + LA-12 (1:1); [d] $p<0.001$ vs LA-12 and pCyD + LA-12 (1:1); [e] $p<0.05$ vs LA-12; [f] $p<0.01$ vs LA-12; [g] $p<0.02$ vs LA-12; [h] $p<0.01$ vs pCyD + LA-12 (1:5); [i] $p<0.001$ vs pCyD + LA-12 (1:5).

3.4.2 CyD polymers as nanocarriers of sorafenib

Sorafenib (Sor, Nexavar, Fig. 41) is an oral multikinase inhibitor approved by the U.S. Food and Drug Administration (FDA) for the treatment of patients with advanced renal cell carcinoma

(RCC) and those with unresectable hepatocellular carcinoma (HCC). This drug displayed antitumor activity across a variety of tumor types, including renal cell, hepatocellular, breast, and colorectal carcinomas. Although originally identified as a Raf kinase inhibitor, sorafenib also inhibits several receptor tyrosine kinases involved in tumor progression and tumor angiogenesis.[225] Despite its efficacy, the hydrophobic nature of this anticancer drug could decrease its bioavailability. At present, 400 mg of Sor is recommended for the liver cancer treatment although severe drug-related toxicity has been reported at this dosage.[226] In the last few years, different nanosystems have been reported to improve its therapeutic efficacy, including lipidic[227], magnetic[228] and polymeric[229] nanoparticles.

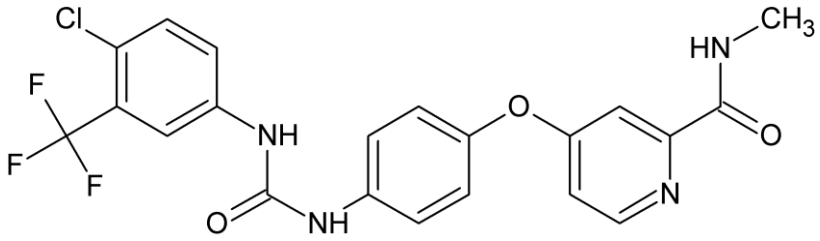

Figure 41: Chemical structure of Sorafenib.

In this thesis, oCyD and pCyD were used as nanocarrier of SOR. The apparent stability constants of the host/guest complexes were also determined. Moreover, preliminary antiproliferative assays of the complexes were performed.

3.4.2.1 SOR solubility study

pCyD or oCyD significanty affect SOR solubility. Figure 42b shows that a clear solution of sorafenib 0.5 mM is obtained only in the presence of pCyD or oCyD (Fig. 42b, vials 3 and 4). When β-CyD was used at the same concentration of cavities of the polymer or oligomer (Fig 42b vial 2) a suspension was obtained, similar to that observed in absence of any solubilizing agents (Fig 42b vial 1). For these experiments SOR was solubilized in DMSO and added to the water solution of CyD systems, the final solutions contained about 0.2% DMSO. Inclusion complexes were characterized with UV/Vis spectroscopy in Tris buffer at pH 7.4, β-CyD was used for comparison, as shown in figure 42a.

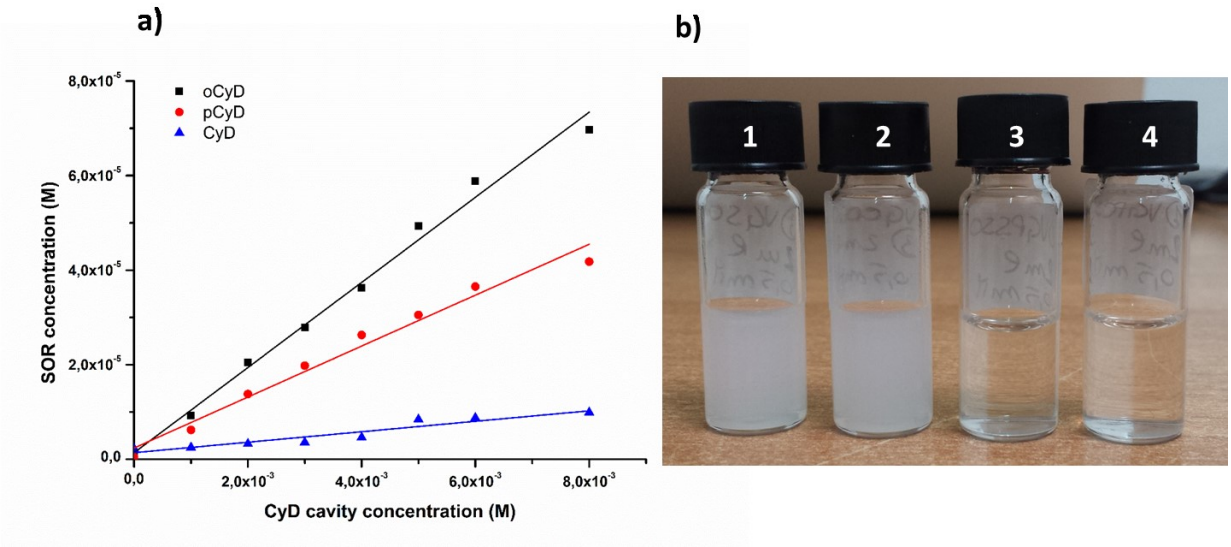

Figure 42:a) Solubility of SOR *vs.* β-CyD cavity concentration of different hosts at pH 7.4: oCyD (black); pCyD (red); β-CyD (blue); B) digital photograph of a solution of 0.5 mM SOR in presence of any (1) or different hosts β-CyD (2), pCyD (3) and oCyD (4).

Apparent stability constants were obtained from solubility measurements with the method of Higuchi and Connors.[230] This method has been widely used for determining stability constant of Drug/CyDs also in the case of polymeric hosts based on CyD.[217,231] Solubility phase diagram obtained by plotting SOR concentration as a function of increasing concentrations of β-CyD, oCyD or pCyD were reported in figure 42a for all the systems CyD-SOR. A A_L-type phase diagram with a linear correlation between SOR and the host concentration and the slope less of unity, was obtained and this suggests the formation of a 1:1 host/guest inclusion complex with the CyD unit. The host concentration has been reported as β-CyD cavity concentration for a more appropriate comparison among the different systems. Interestingly the solubility of the drug increased linearly with the increase of the host concentration. The solubility of SOR in the presence of either pCyD or oCyD increases of 4 and 8 times compared to β-CyD, respectively. The oligomer is the most effective solubilizing agent, more effective than pCyD. This behavior suggests that a longer polymer chain might reduce solubilizing properties of these systems as earlier observed.[232] Moreover, the SOR solubility is slightly affected by β-CyD at the experimental condition used. According to the slope and the intercept of the line obtained the value of inclusion constant Kc are listed in table 5.

Table 5: Stability constant values for the inclusion of SOR in β-CyD, pCyD and oCyD at 25 °C in buffered aqueous solution (pH 7.4)

Hosts	Kc
β-CyD	793±50
pCyD	7464±80
oCyD	21629±400

3.4.2.2 CD spectroscopy

The inclusion ability of oCyD or pCyD for SOR was investigated by CD spectroscopy, β-CyD was also tested as comparative systems. Figure 43 shows the induced CD spectra obtained when Sorafenib was added to an oCyD solution at pH 7.4. The spectra show 2 positive bands at 215 nm and 275 nm and a negative band at 240 nm. The intensity of the bands increased when the guest/host molar ratio increased thus suggesting that Sorafenib can interact with the oligomer. The CD spectra obtained in the presence of either β-CyD, pCyD or oCyD were recorded and shown in figure 44. For an easier comparison among hosts which have a different number of cavities, CD spectra were carried out at the same concentration of CyD cavities in the samples. The highest intensity of the CD bands was observed in the case of oCyD, in keeping with the Kc values. This result highlight the advantage of using polymeric structures as solubilizing systems. Furthermore, in the case of oCyD, a less branched and more flexible systems, the strongest induced CD signals was obtained compared to the other systems at equal concentration of CyD cavities, suggesting a better host/guest interaction in aqueous solution.

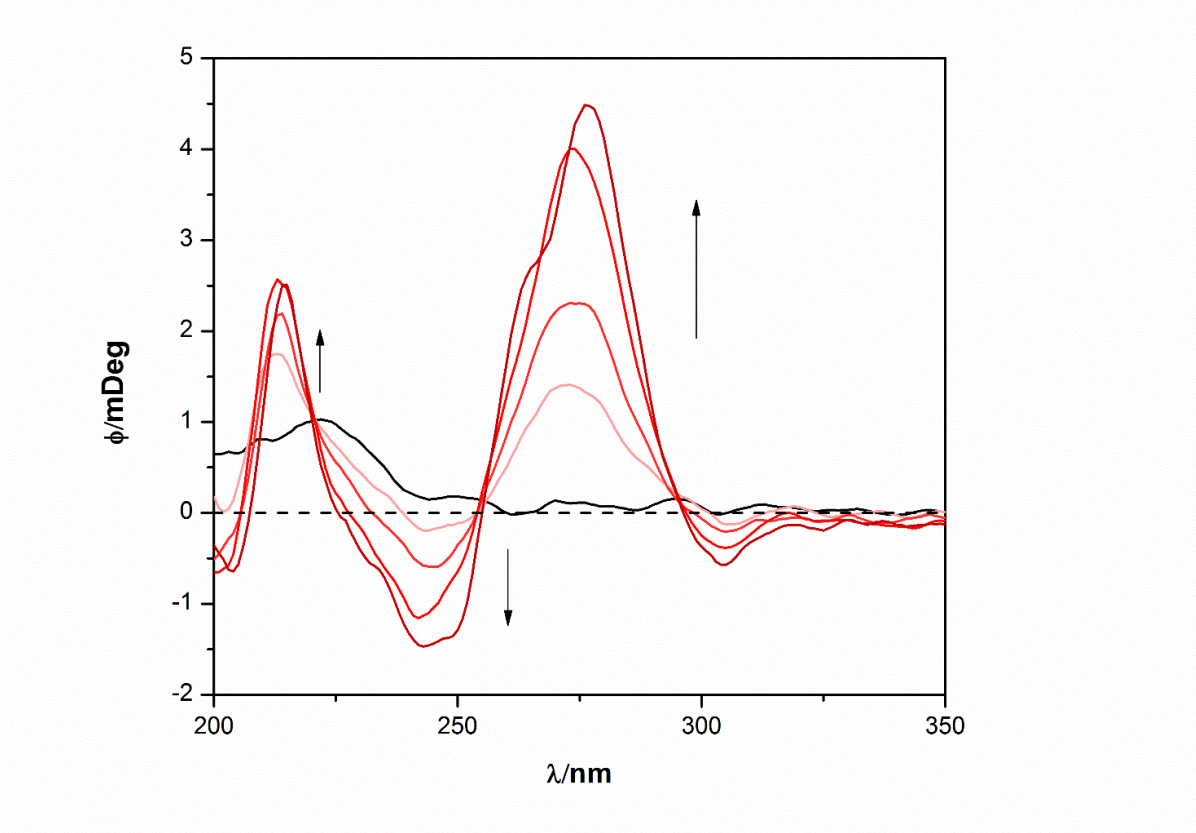

Figure 43: CD spectra of SOR (read from black to light red: 0.5, 1, 2 and 3 × 10^{-5} M) with oCyD (β-CyD cavity concentration: 1.3 × 10^{-3} M) at pH 7.4 (10 mM Tris buffer).

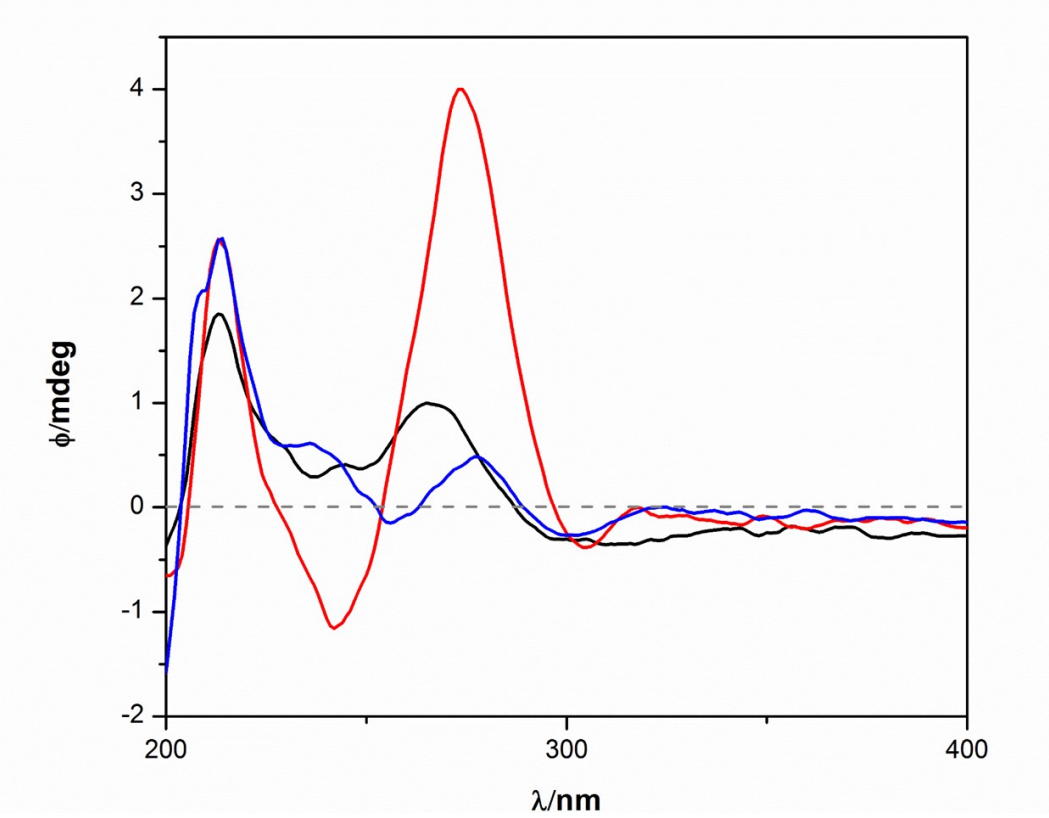

Figure 44: CD spectra of SOR (2 × 10^{-5} M) with different hosts (β-CyD cavity concentration: 1.3 × 10^{-3} M): oCyD (red); pCyD (blue); β-CyD (black).

3.5 Antiproliferative activity (MTT assay)

The SOR-polymer inclusion complexes were evaluated for their cytotoxic effects on different cancer cell lines. For these set of experiments we selected three different cancer cell line: MCF-7 (breast cancers line), GILIN (human neuroblastoma cell line) and HepG2 (liver hepatocellular carcinoma).

pCyD/SOR, oCyD/SOR complexes were tested in all the cell lines and their toxicity were compared to that of SOR, the IC_{50}s values obtained are listed in table 6.

As shown in table 6, the administration of sorafenib as inclusion complex with a polymeric systems did not undergo significant decreases of its antitumor activity in all the cell lines treated. Furthermore, in the case of GILIN cell line, oCyD seems to slightly improve the cytotoxic activity of SOR.

In addition, *in vivo* experiments are still ongoing to investigate the effect of CyD polymers on the pharmacokinetic profile of SOR.

Table 6: Summary of IC50s (μM) of SOR and its inclusion complex with pCyD and oCyD on MCF-7, HepG2 and GILIN cells.

Cellular lines	SOR	pCyD/SOR	oCyD/SOR
MCF-7	8.59±1.17	21.8±3.7	15.9±3.4
HepG2	4.10±0.32	5.99±0.65	7.80±2.34
GILIN	5.12±1.18	4.24±0.77	2.91±0.39

3.6 Mesoporous silica nanodiscs (NDs) as powerful tools for biosensor design

In the field of hard materials, mesoporous silica nanoparticles (MSNs) represent a good candidate for drug delivery systems thanks their ability to store large payloads within their porous structure. Both the particles morphology and the organization of the mesophase are important and tunable features to improve the encapsulation extent as well as the cellular uptake efficiency of the particles. In addition, their external surface can be easily functionalized adding to the MNPs new targeting or functional moieties by simple exploitation of the well-established silicate chemistry.

Among the wide range of particles nowadays available, the best synthetic route to obtain disc-shaped mesoporous material, the nanodiscs (NDs) were selected. This novel material, taking advantage of its extraordinary discoidal shape, could be successfully implemented in a prototype biosensor device (self-assembled monolayer of NDs) for the selective recognition and adhesion of cancer cells. Specifically, a folic acid functionalised self-assembled monolayer (SAMs) of nanodiscs was prepared and employed in cellular adhesion experiments. These systems have so far been widely used as two-dimensional (2D) artificial surfaces in biomedical research.[233] In this case, SAMs of well ordered porous nanodiscs, compared to flat surfaces, allow to take advantage of the pores of the particles for hosting fluorescent dyes or biomolecules that can be used for imaging or *in situ* drug delivery from 2D surfaces.

3.6.1 Synthetic aspects

The mesoporous silica nanodiscs (NDs) were synthesized using tetramethyl orthosilicate (TMOS) as silica source and octadecyltrimethylammonium chloride (C_{18}TMACl) as surfactant. The reaction was conducted in presence of an equimolar amount of surfactant template and silica source under moderate stirring (500 rpm) overnight at r.t. The NDs were recovered by centrifugation (4000 rpm) and washed several times with water and then with ethanol. Finally, to remove the surfactant template from the porous framework, the product was calcinated in air at 550 °C for 8 hours.

The material was first morphologically characterized by scanning and transmission electron microscopy (SEM and TEM; Fig.45). SEM and TEM images display the homogenous discoidal structure of the material, characterized by an average diameter and thickness of 500 ± 40 nm and 80 ± 4 nm, respectively. Moreover, TEM images display a regular and perpendicular distribution of pores. N_2 adsorption studies confirmed the presence of pores, characterized by an average pore size of 3.8 nm (Fig. 46b), and a total pore volume of 0.82 cm^3/g. Small-angle X-ray scattering (SAXS) pattern shows two broad peaks (Fig. 46a) centered at q = 1.71 nm^{-1} and q = 3.2 nm^{-1}, that can be related to the (100) and (110) Bragg peaks of hexagonally ordered pores.[234] Nevertheless, the absence of sharp peaks reveals that the NDs lack of a highly ordered packing. The broadness of the (100) peak and the value of the Bragg spacing d_{100} = 3.7 nm ($d = 2\pi/q$) are in agreement with the pore diameter distribution determined by N_2 absorption. Elemental analysis of the material by X-ray photoelectron spectroscopy (XPS) was also performed. The material resulted composed of Si(2p) and O(1s), which were present in 34,9 ± 0,4 and 65,1 ± 0,4 atomic % respectively in the sample. TGA analysis showed the negligible weight loss of 4% (Fig. 47a)

highlighting that the calcination process removed all organic surfactant. Finally, ζ-potential analysis of NDs resulted -25.9 mV in PBS pH 7.4, indicating an intense negative surface charge for these nanoparticles in physiological conditions.

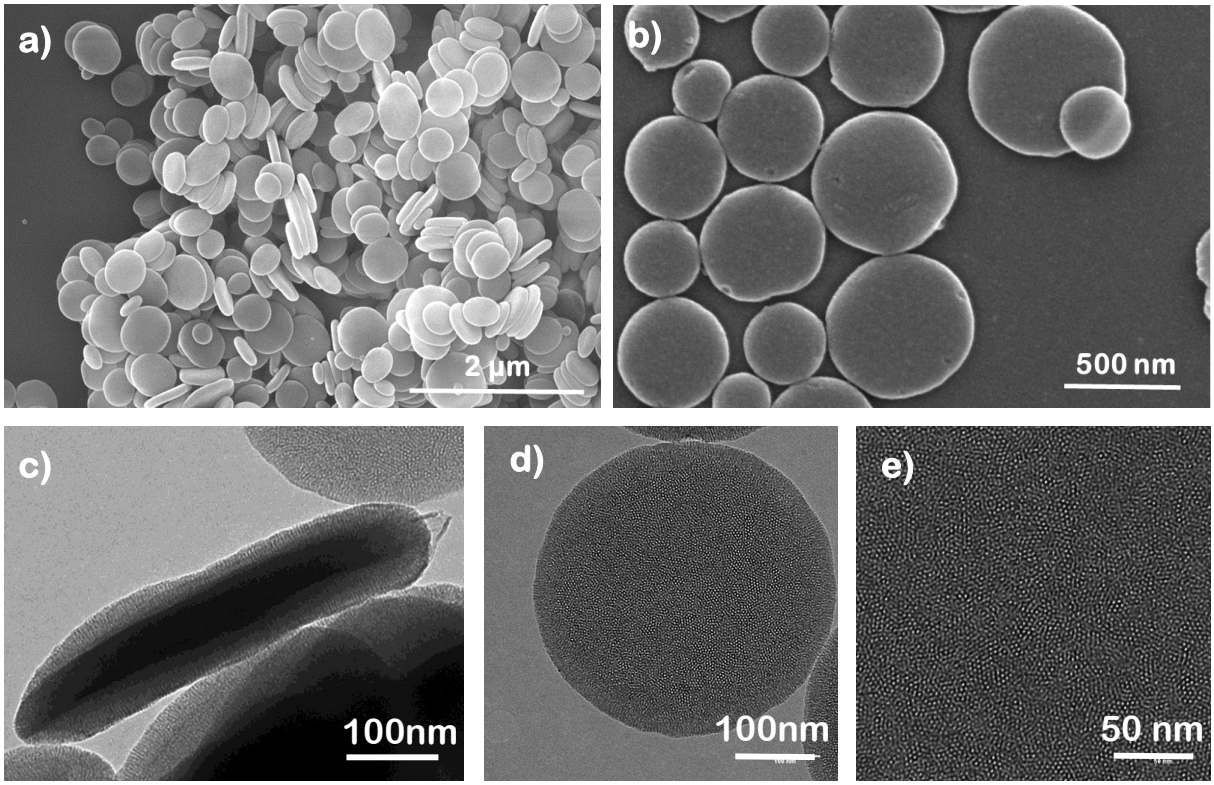

Figure 45: a) and b) SEM images of NDs at different scale bar; c)-d) and e) TEM images of NDs at different scale bar.

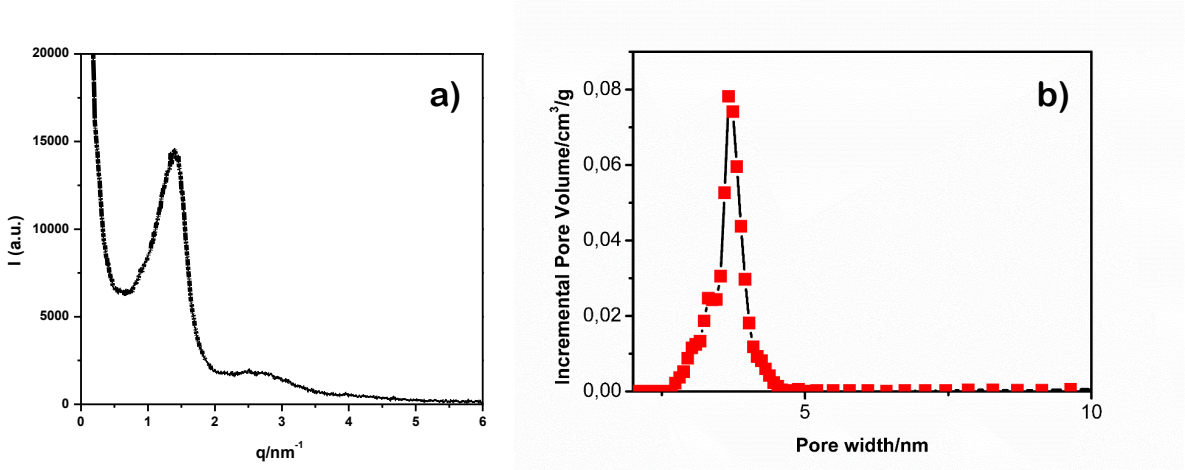

Figure 46: a) SAXS profile of NDs; b) N_2 absorption determined average pore diameter.

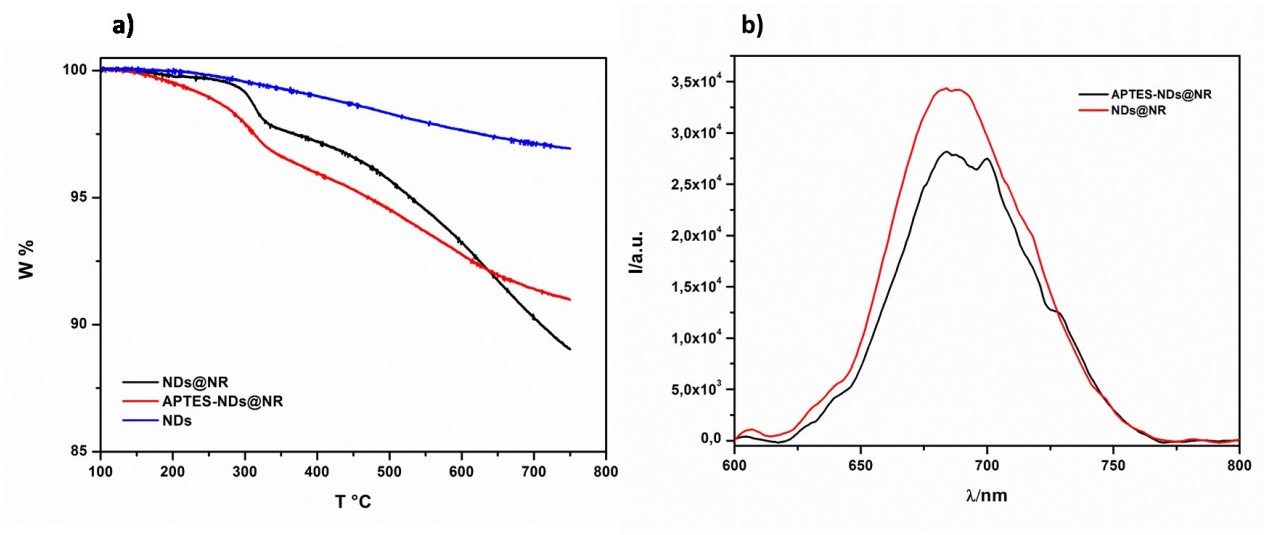

Figure 47: a) Comparative TGA analysis of NDs, NDs@NR and APTES-NDs@NR; b) fluorescence emission spectra of NDs@NR (red) and APTES-NDs@NR (black).

3.6.2 Cellular uptake experiments

In order to perform an initial screening on the cellular uptake of NDs, preliminary incubation experiments in tumor cells were performed. The cellular uptake of NDs in Glioma C6 cancer cells was then investigated by flow cytometry and fluorescence confocal microscopy. Thus, to allow detection of the particles, NDs were covalently labeled with fluorescein isothiocyanate (FITC-NDs). Specifically, Glioma C6 cells (1.5×10^4) were incubated with a 50 µg/mL and a 100 µg/mL dispersion of NDs in culture medium for 3 hours, and subsequently thoroughly washed with PBS to remove the non internalized particles. The confocal images and the orthogonal view of the Z-stack reconstruction depicted in figure 48a clearly highlight an endocytosis of the NDs in the cancer cells. The internalization of NDs was then confirmed also by flow cytometry (Fig. 48b).

Interestingly, this preliminary *in vitro* uptake investigation has detected a high uptake of NDs into the Glioma cells, pointing towards the possibility to deliver high levels of drugs to the tumor site. These findings are in agreement with the findings of Godin at al.[235] who investigated the uptake of 600 nm × 400 nm disc-shaped silicon NPs. Specifically, the uptake of these particles in tumor cells was five-fold higher compared to their spherical counterparts. Such result was achieved without pursuing any active targeting strategy, emphasizing the effect of the geometry of the particles on their *in vitro* cellular uptake behavior.

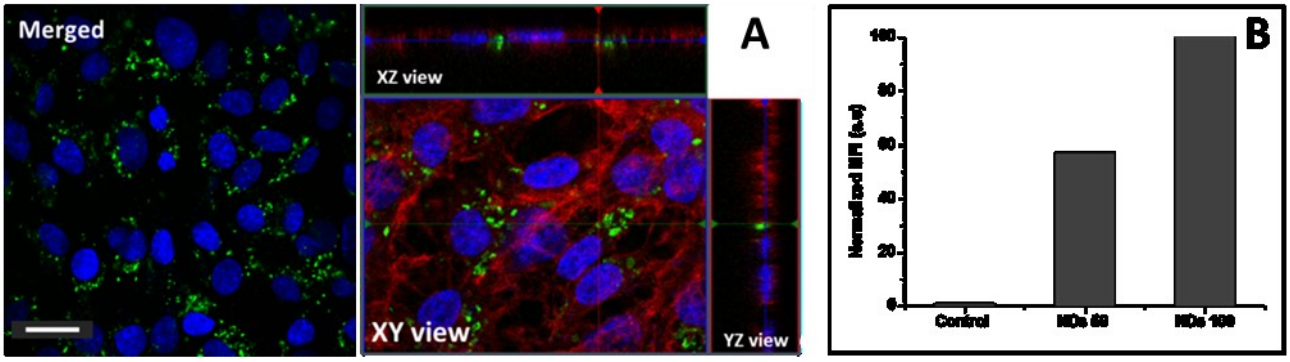

Figure 48: A) Confocal microscopy images of C6 Glioma cells after incubation with NDs (50 µg/mL) for 3 h at 37 °C. The nuclei was stained with DAPI (blue) and the NDs were labelled with FITC; B) Cellular uptake quantitative analysis determined via flow cytometry after 3h of incubation at 37 °C. The FITC fluorescence of 5.000 living single cells was analyzed. The normalized MFI is referred to the Median Fluorescence Intensity (MFI) of the test sample to the MFI of control cells, cultured in the absence of nanoparticles.

3.6.3 Self assembled monolayers of NDs

NDs were hence employed in the preparation of self-assembled monolayers (SAMs), to be used in the selective adsorption of cancer cells and *in situ* delivery of a hydrophobic model compound. The formation of a porous nanoparticle-based SAM was achieved by chemical functionalization[236-240] of the channel entrances of the porous material (the most reactive site on the particle's surface), allowing control of the pores orientation, which can then react with a pre-activated, functionalized surface. The surface of mesoporous silica NDs can be further modified with a wide range of organic biomolecules. In this case, to achieve specific adsorption on tumor cells FA has been used. Moreover, to detect effective release of guest molecules from the porous structure of the NDs, the particles were loaded with nile red (NR), a small hydrophobic dye, prior to preparation of the monolayer.

For the implementation of SAMs, NDs were hence first loaded with nile red (NDs@NR; λ_{exc} = 560 nm; λ_{em} = 633 nm), a hydrophobic dye to be employed in the investigation of the possibility of material transfer from the pores of the NDs in the SAM and the cells, and functionalized with (3-aminopropyl)triethoxysilane (APTES-NDs@NR), that provides the presence of amino groups on the surface of nanoparticles obtaining anchoring points to the substrate and for further grafting of folic acid. The encapsulation process of NR within the pores of NDs was carried by stirring NDs (1 mg/mL) in an ethanolic solution of NR (2 mg/mL) at r.t. overnight. To remove unloaded NR, the material was hence washed several times with ethanol, and finally dried under vacuum. Then, NDs@NR were functionalized with APTES. To try to avoid the leakage of the dye from the NDs pore during their functionalization with APTES, we first attempted the condensation reaction in ethanol, solvent in which NR has a low solubility. Unfortunately, In this case we did

not succeed in obtaining a high grafting of APTES onto the surface of the NDs. Therefore, an alternative procedure involving toluene, solvent in which the NR is more soluble, but also in which NDs are better dispersed, were used. This time, the grafting resulted more effective, yet causing a minor leakage of nile red from the pores.

SEM analysis of the functionalized NDs did not highlight a difference in the morphology of the particles upon loading of the NR, and most importantly condensation of APTES on the NDs surface. TGA analysis of NDs@NR and APTES-NDs@NR (Fig. 47a) displayed an intense loading of the dye in NDs, by detecting a weight loss of 11% for NDs@NR, starting at 350 °C, temperature at which the NDs are still thermally stable. The weight loss of APTES-NDs@NR resulted slightly less pronounced (9 %), most probably due to the introduction of an external silica layer during the grafting process, and the small leakage of NR. Nevertheless, the emission properties of both the hybrids were analyzed at the fluorimeter, and they both resulted to contain the dye (Fig. 47b). NDs@NR and APTES-NDs@NR were finally characterized by ζ potential, and, whilst as expected the loading of NR did not produce any modification of the superficial charge of NDs, upon APTES grafting, the *ζ value* resulted less negative (-13.4 mV).

The SAMs were hence prepared on glass slides, which were pre-functionalized chemically with 3-(triethoxysilyl)propyl isocyanate (IC), following the procedure of Zabala Ruiz et al.[236] More precisely, glass plates were first pre-activated through a treatment with a mixture of H_2SO_4 and H_2O_2, (3:1 v/v), to achieve the hydroxylation of the surface. Then the activated glass plates were dipped into a solution of IC in toluene, to allow condensation of the trisiloxane group of IC onto the glass. Thus, isocyanate glass substrates were obtained. Lastly, the IC functionalized glass plates were reacted with APTES-NDs@NR by sonicating them into a toluene dispersion of the particles (1mg/mL) for 8 minutes, allowing the formation of the urea bond between isocyanate group of IC and NH_2 group of the APTES functionalized NDs. The entire synthetic process is represented in figure 49.

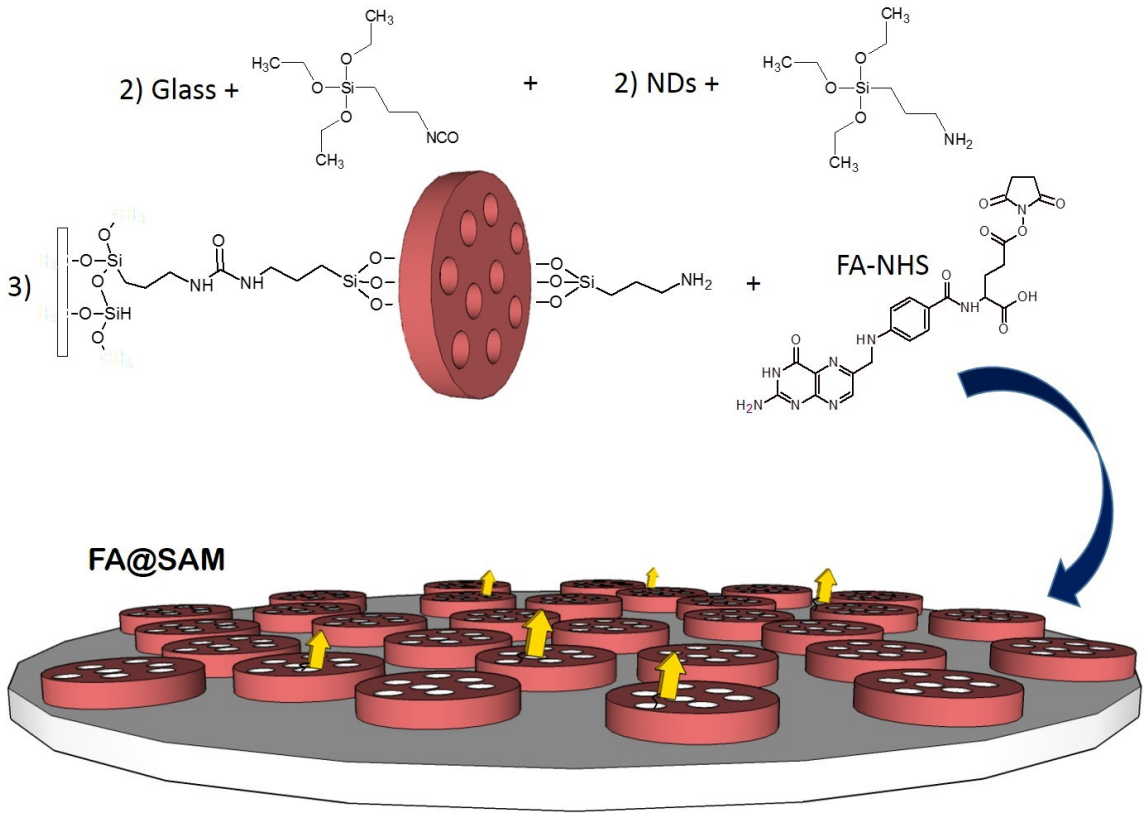

Figure 49: Preparation of FA@SAM as biological sensor.

The NDs monolayers were first investigated through scanning electron microscopy (SEM) and confocal microscopy. As shown by Figure 50, the SEM images of the monolayers highlighted a homogenous particle distribution of the NDs, without significant vertical stacking (Fig. 50a). Confocal images instead demonstrated the persistence of the presence of the NR dye in the porous system (Fig. 50b).

To complete the device by adding the biologically relevant recognition unit, functionalization of the SAMs with folic acid (FA) was finally performed *via* DCC catalyzed peptidic coupling. Specifically, FA was first pre-activated for one hour in DMSO in presence of N,N'-dicyclohexylcarbodiimide (DCC) and N-Hydroxysuccinimide (NHS) obtaining folate N-hydroxysuccinimide (FA-NHS). Then, few drops of the FA-activated DMSO solution were placed onto APTES-NDs@NR monolayers to allow the formation of amidic bond at the interface of the contact surface between NH_2 groups of APTES and FA-NHS. The reaction was left overnight, then the FA-functionalized SAMs were washed by immersion in water and ethanol and finally dried under nitrogen flow.

To demonstrate the effective functionalization of the SAM with FA, high resolution XPS analysis of the N 1s and C 1s signals of the material, was performed, and compared to that of the naked SAMs. The deconvolution of the N 1s band of a naked SAM (Fig. 51a) highlights the

presence of two distinct components. The first one, at 398.5 eV, is associated with the NH_2 groups[241] of the free amino groups present on the surface of the NDs in the SAM. The second component, centered at 400.5 eV, is instead accountable to protonated amino groups. The N 1s band of SAM@FA (Fig. 51b) shows also a component attributable to the nitrogen atoms involved in the amidic bond (401.6 eV) between the anchored aminopropylsilane and the FA. Regarding the C 1s band of the naked SAM (Fig. 51c), it again consists of a predominant peak at 285.0 eV, characteristic of aliphatic carbons, and a minor peak at 287.2 eV, arising from the nitrogen-bonded carbons. The C 1s band of SAM@FA shows an additional component at 289.9 eV due to carboxylic and amidic groups of FA (Fig.51d).

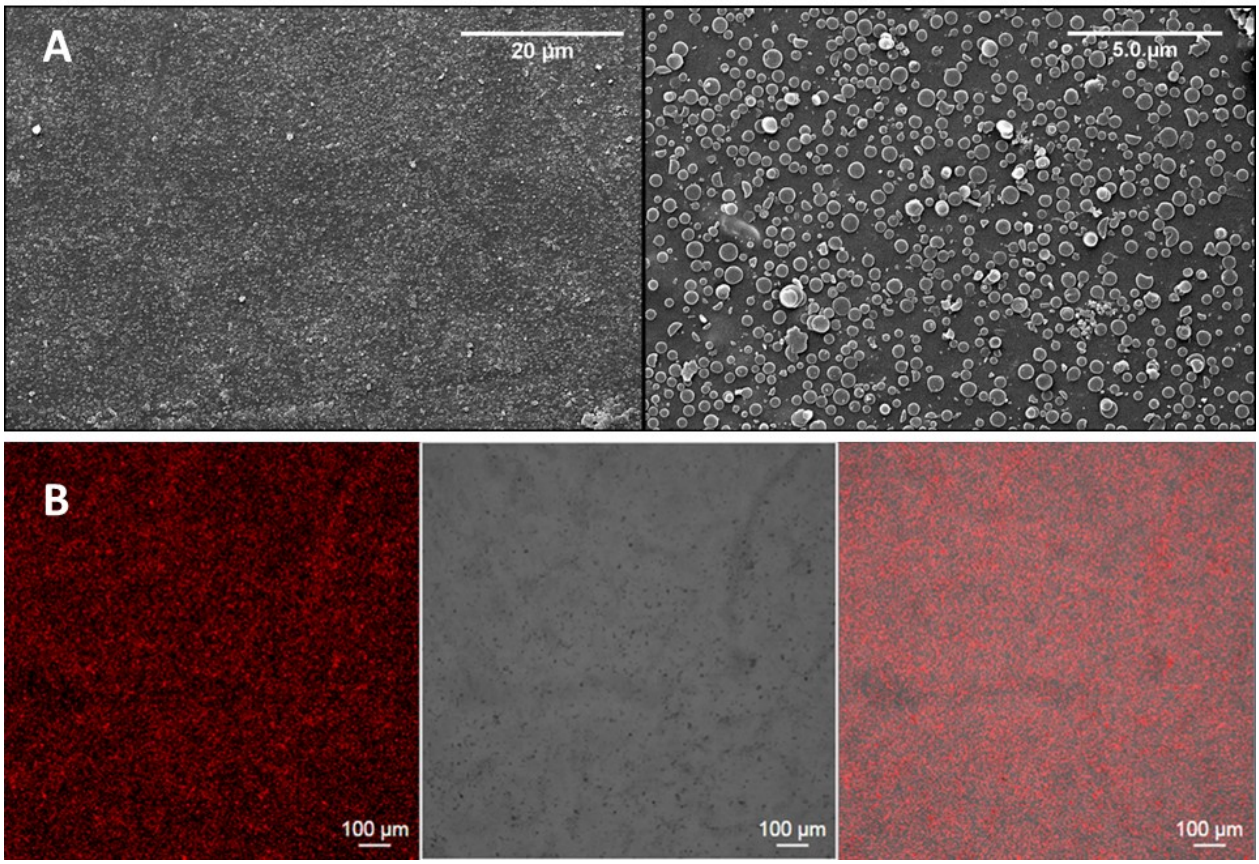

Figure 50: A) SEM images of NDs monolayer; B) Fluorescence microscopy images of NDs monolayer@NR.

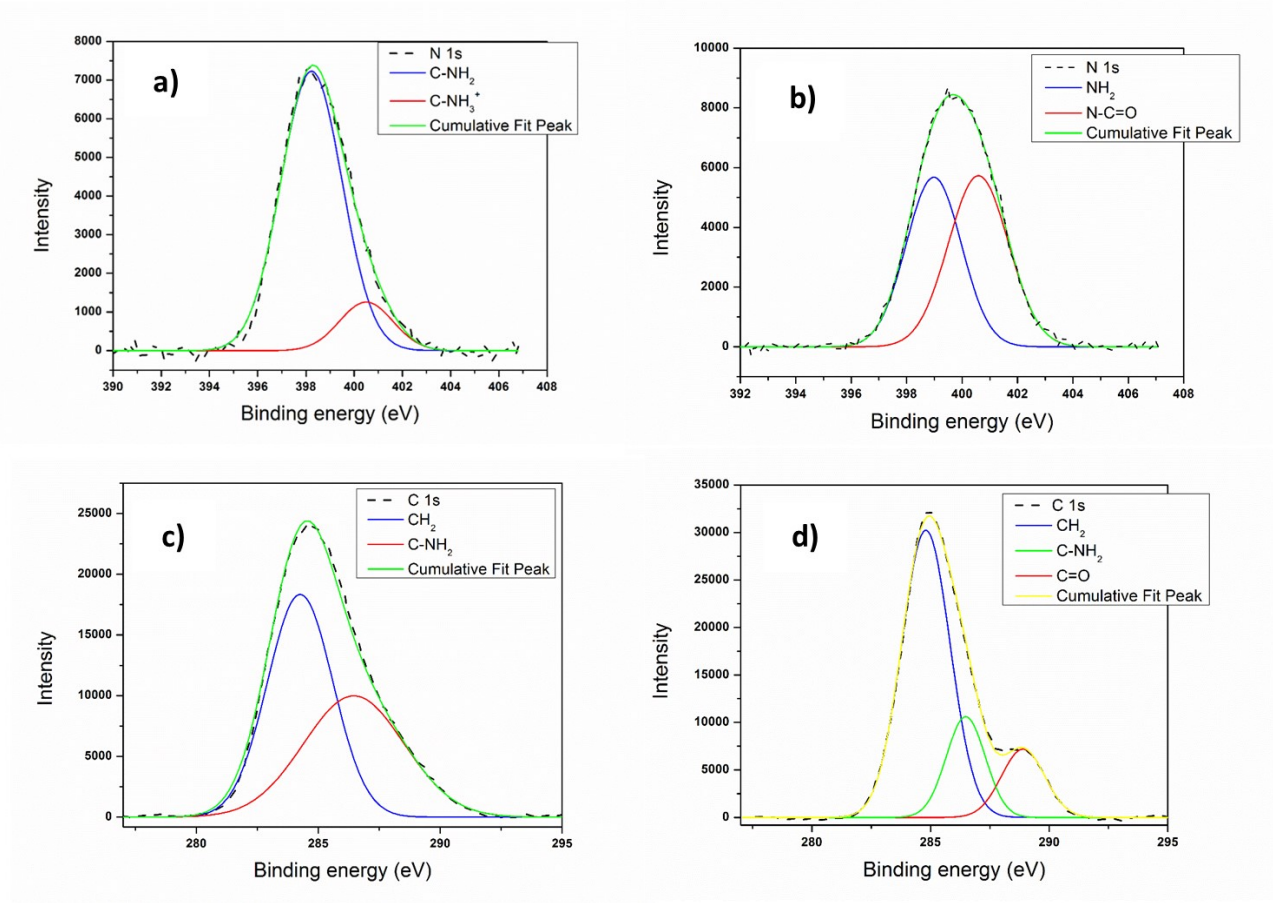

Figure 51: A) High resolution N 1s XPS spectral regions of non functionalized SAM , (B) N 1s XPS spectral regions of SAM@FA, (C) High resolution C 1s XPS spectral regions of non functionalized SAM and (D) C 1s SAM@FA.

3.6.4 Cells adhesion experiments onto SAMs

Once the morphology and the effective surface functionalization of the SAMs were confirmed, adhesion experiments on FA functionalized SAMs were carried out. For this purpose, to check the selectivity of folic acid toward specific cancer cell lines, we used HeLa cells overexpressing folate receptor on their surface.[242] As control experiments, the same cells were seeded on SAMs without folic acid.

Specifically, 1×10^6 cells were stained with DiO, (λ_{exc} = 488 nm; λ_{em} = 501 nm) and seeded on SAMs and SAM@FA, to evaluate any effects of folic acid on the binding activity of the monolayers. After incubation (3 and 24 hours, 37 °C), cells were washed and fixed with PFA. Confocal microscopy showed that the adhesion behavior on the SAMs of the cancerous cells was dramatically different: as shown in figure 52a-b, the population of HeLa cells on SAMs@FA was higher than that non-functionalized monolayer. Accurate counting of the number of cells on the FA functionalized SAMs *versus* the non functionalized SAMs confirmed an increase of 7.6 and 10 time of the population for HeLa cells attached to the SAM@FA after 3 and 24 hours of incubation, respectively (Fig. 52c). Moreover, increasing incubation times

lead to significantly higher cell adhesion. Finally, to test the ability of the SAM@FA to release the content of their porous structure directly into the cells, another adhesion experiment with non-stained HeLa cells was performed, and their *in situ* staining with NR monitored by confocal microscopy. As demonstrated in figure 52d, already upon short incubation time (3 hours) NR could already be detected inside the cells, indicating the possibility of transferring hydrophobic molecules from the support to the cells adsorbed. In conclusion a multifunctional device were developed, able not only to detect specific cancer cells, but also to control the intracellular release of small hydrophobic molecules directly inside of the adsorbed cells.

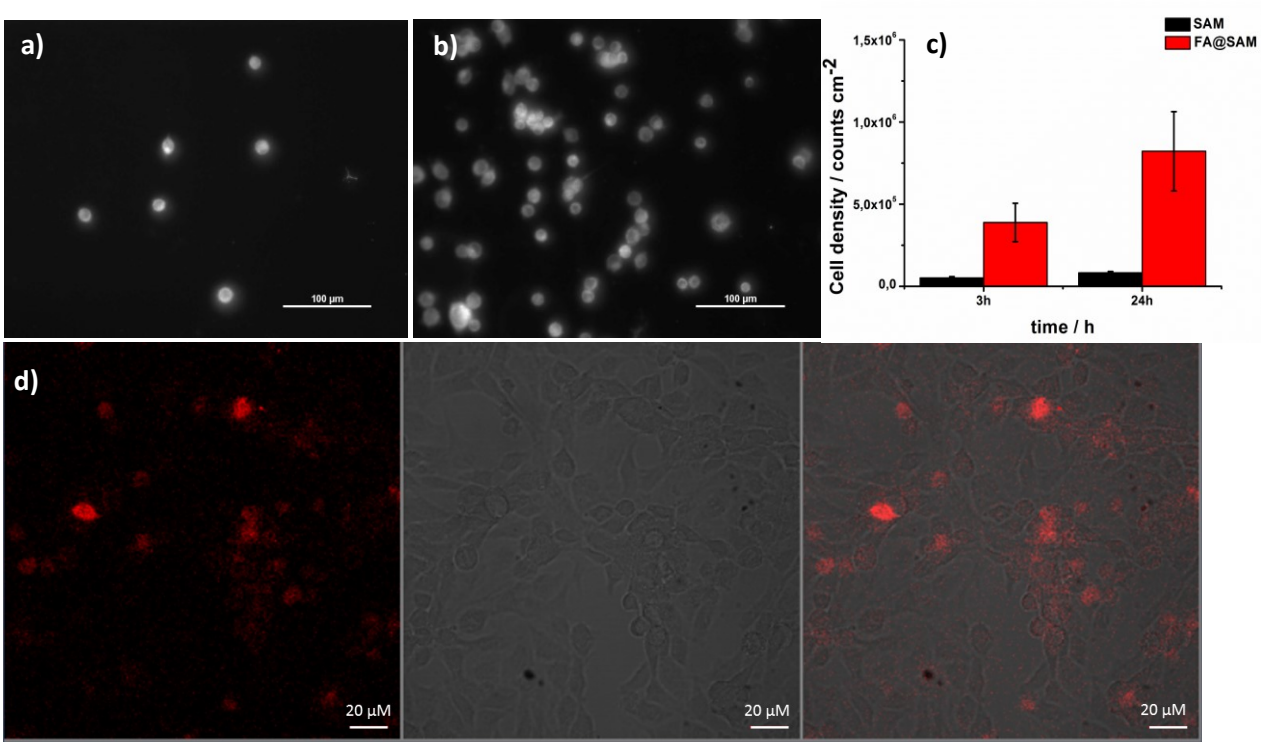

Figure 52: Cell imaging experiment performed with Hela cells overexpessing folate receptors at 3 h of incubation: a) SAM alone; b) SAM@FA, for the experiments the cells were stained with DiO; c) confocal images of non-stained cells of SAM@FA, for detecting NR inside cells.

3.7 Disintegrable Disulfide-doped Silica Nanodiscs (ss-NDs)

Once assessed the efficiency of NDs in entering the cells, we hence decided to further improve this carrier by increasing its biodegradability. To do so, the structure of NDs were doped with disulphide bridges (S-S) in order to introduce a responsiveness to redox stimuli in the particle, which might be able to trigger its structural breakdown. Indeed, this new disc-shape mesoporous material, taking advantage of bio-redox reactions, is expected to undergo a controlled

disintegration process, possibly affording better exocytosis, as well as an improved drug delivery activity.

3.7.1 Synthetic aspects

Disulfide-doped silica nanodiscs (ss-NDs) containing different percentages of disulfide bridges in the framework of the particles (namely 10, 30 and 50% of S-S bonds) were synthesized *via* a base-catalyzed process involving a mixture of two silanes, tetramethyl orthosilicate (TMOS) and bis(triethoxysilyl-propyl)disulfide (BTSPD). This was done in order to better investigate the impact of the biocleavable disulfide bridge in the structural breakdown of the particle, and possibly in its drug delivery efficiency.

The syntheses of ss-NDs were carried out under moderate stirring (500 rpm), at r.t and left overnight using three different molar ratio of TMOS/BTSPD (90/10, 70/30 and 50/50) to obtain different percentages S-S bonds doped nanodiscs. To remove the surfactant without damaged the hybrid organosilica structure of the disulfide-doped NDs, the synthesized ss-NDs were refluxed overnight in acidic ethanol, and then washed with water and ethanol several times.

Morphological characterization of the hybrid material was first performed by scanning and transmission electron microscopy (SEM and TEM). Figure 53 displays the homogenous discoidal morphology of the material evidencing a certain monodispersity of the particles size (average diameter ss-NDs 10% 345.4 ± 50.3 nm, ss-NDs 30% 331.4 ± 45 nm and ss-NDs 50% 249.81 ± 26 nm). In particular, TEM images highlighted the progressive loss of the regularity of the pore distribution along with the increasing of the percentage of S-S linker percentage in the particles. The decrease of the order of the porous structure and the overall porous volume was further investigated by porosimetry and SAXS. Indeed, as shown in Figure 55d, upon increase of the S-S percentage, the SAXS profiles of the particles seem to flatten, progressively loosing the (100) diffraction peak. Moreover, N_2 adsorption investigations unveiled a dramatic decrease of the pore volume of the particles, which dropped from the 0.82 cm^3/g value obtained for NDs (with an average pore size of 3.8 nm) to 0.79 cm^3/g, 0.71 cm^3/g, 0.46 cm^3/g, for NDs 10%, ss-NDs 30% and ss-NDs 50% respectively (Fig. 54). Incorporation of disulfide linker in ss-NDs was further demonstrated by elemental analysis of the material conducted by X-ray photoelectron spectroscopy (XPS; Fig. 55a) This technique detected the atomic percentage of S (2p) in the hybrid nanoparticle samples, which increase from 4.5 ± 4.4 in ss-NDs 10%, to 39.1 ± 2.2 in ss-NDs 50%. These results were hence confirmed by TGA analysis (Fig. 55b), which detected an intense weight loss for ss-NDs in the temperature region where pristine NDs were instead thermally stable, which increased along with the progressive incorporation of S-S

bridge in the particles. Specifically the weight losses were 20%, 27% and 35% for ss-NDs 10%, ss-NDs 30% and ss-NDs 50% respectively. This doping also affected the ζ potential of the hybrid particles, which resulted less negatively charged as compared to NDs (Fig. 55c).

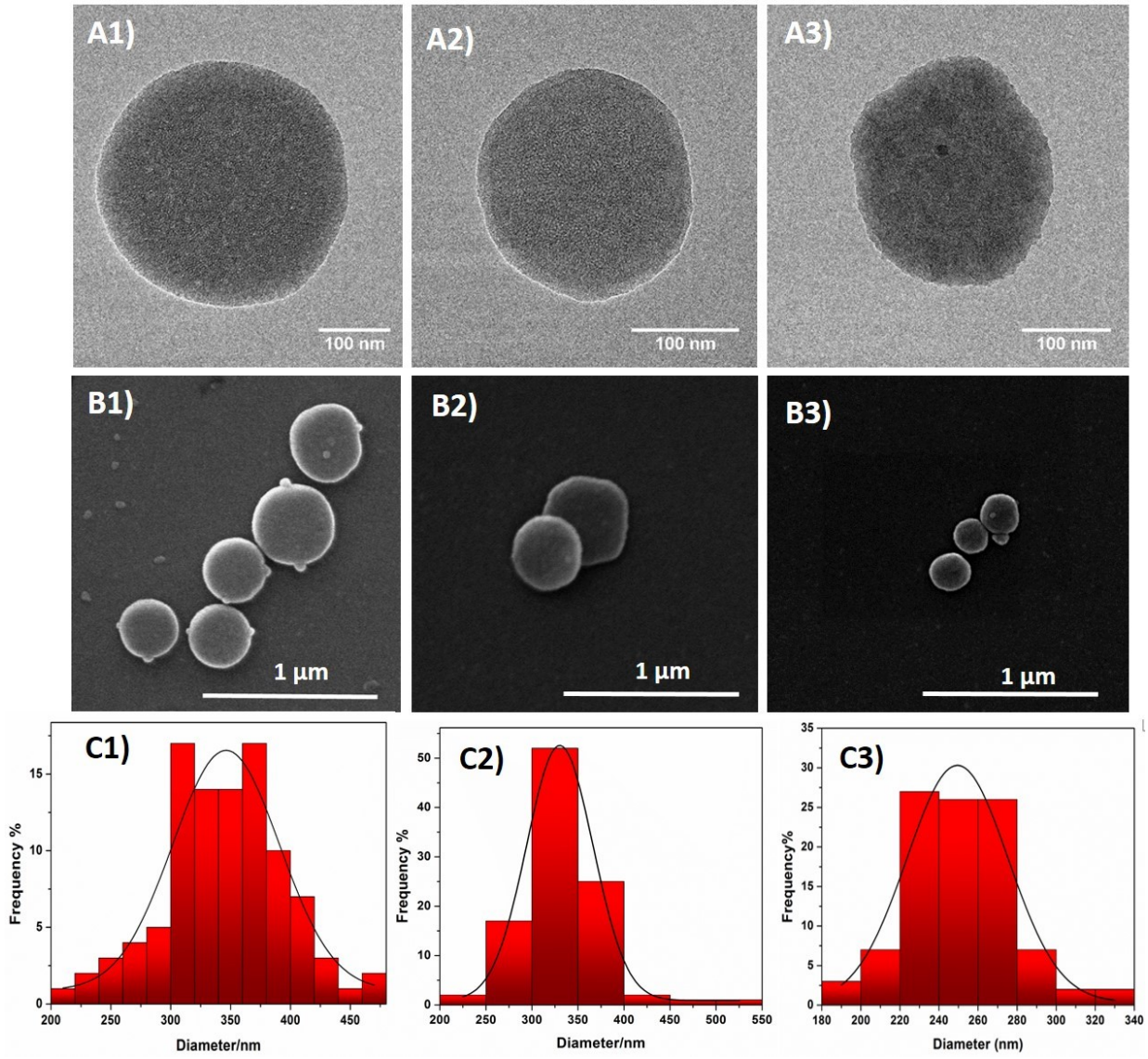

Figure 53: Morphological characterization of the synthesized ss-NDs 10% (1) 30% (2) and 50 (3) by TEM (A) and SEM (B) microscopy, and their respectively size distribution.

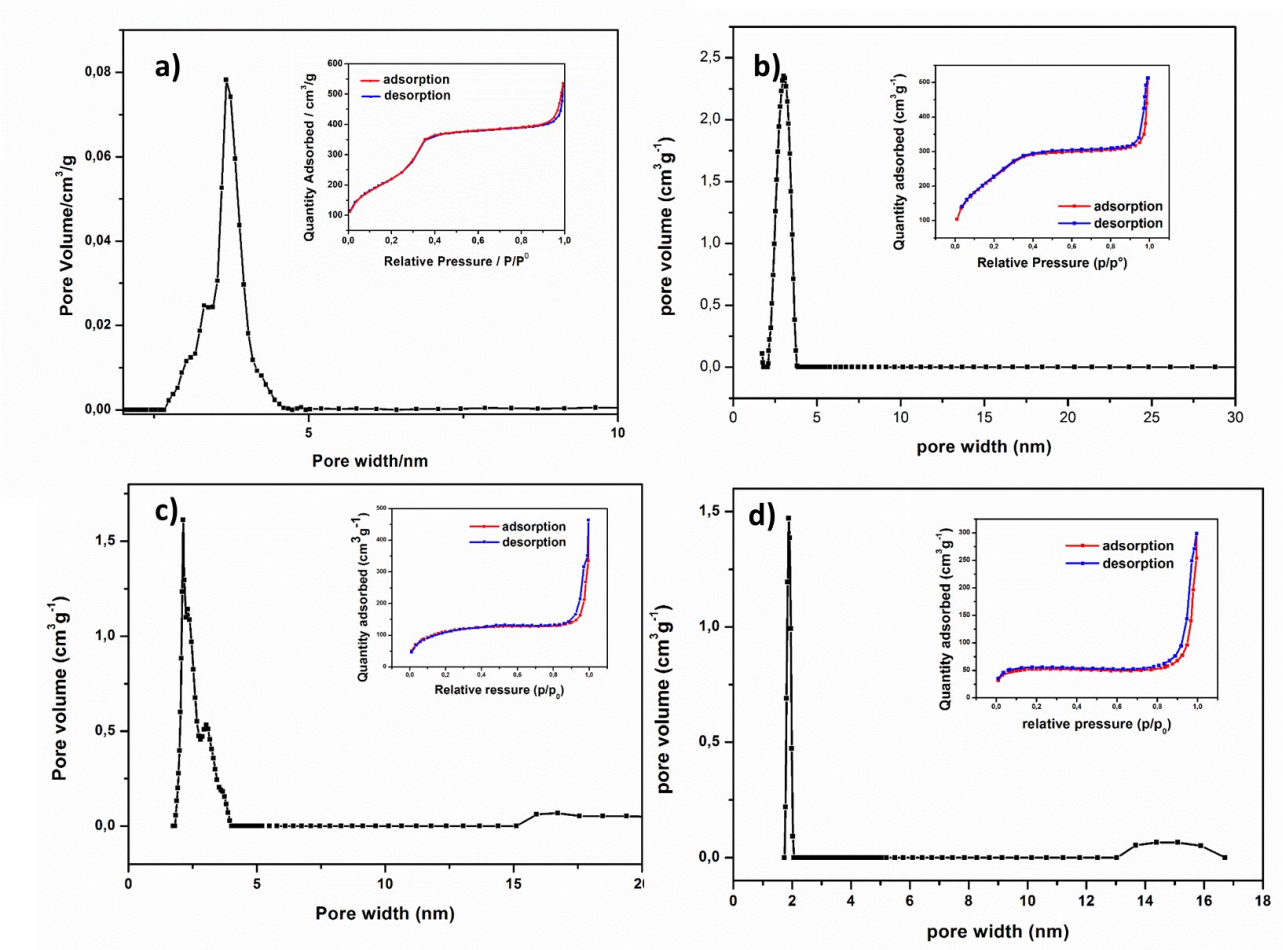

Figure 54: Compared nitrogen absorption analysis of NDs, ss-ND 10%, ss-ND 30% and ss-ND 50%.

a)

	Atomic % Si (2p)	Atomic % S (2p)
NDs	99,7 ± 0,4	0,2 ± 0,4
ss-NDs 10%	95,5 ± 4,4	4,5 ± 4,4
ss-NDs 30%	65,2 ± 1,9	36,1 ± 0,8
ss-NDs 50%	69,9 ± 2,3	39,1 ± 2,3

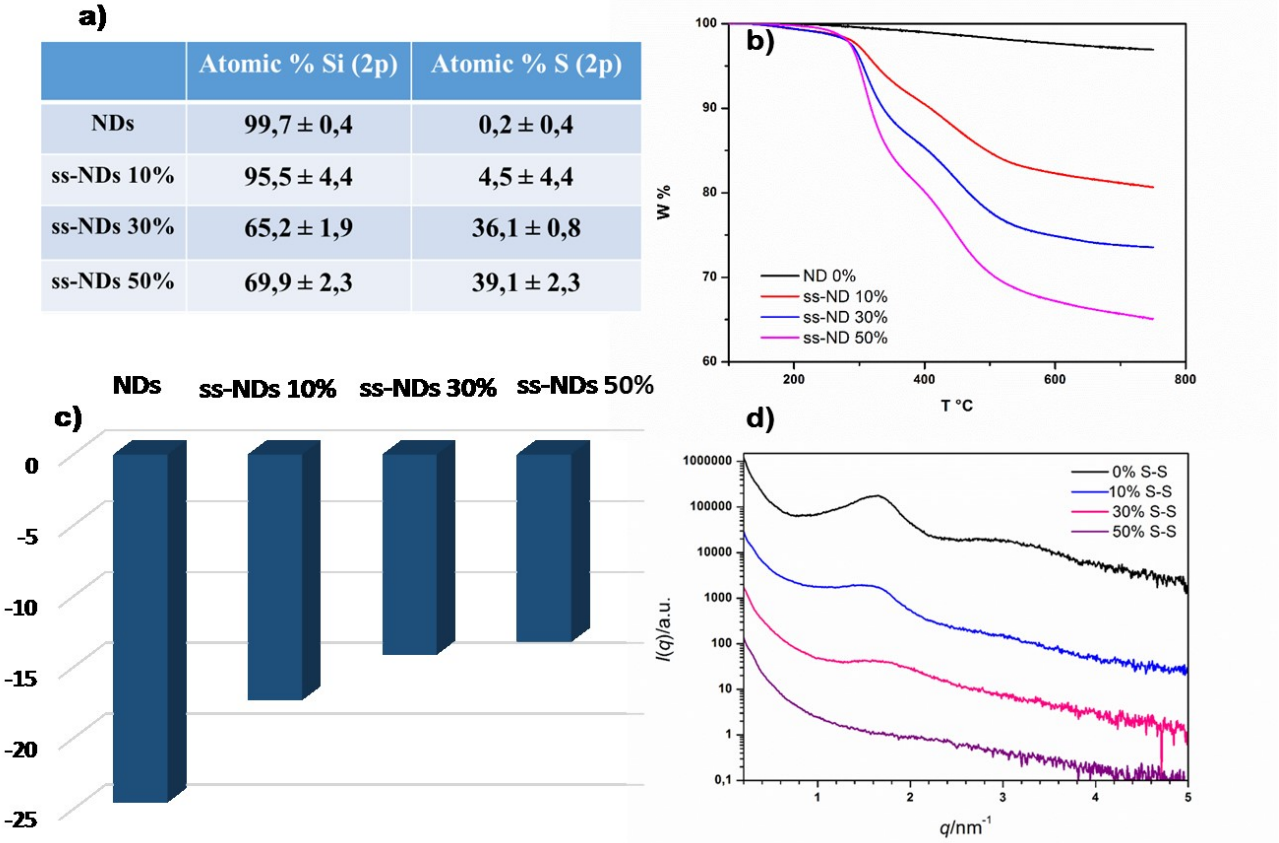

Figure 55: a) XPS analysis of NDs and ss-NDs; b) TGA analysis of NDs and ss-NDs; c) ζ-values of NDs and ss-NDs; d) SAXS profile of NDs and SS-NDs.

3.7.2 Characterization of the breakability of ss-NDs

The responsiveness of the ss-NDs towards reducing agents was investigated in the presence of reduced glutathione (GSH), a thiol-containing tripeptide present in the cytoplasm able to reduce disulfide bonds. It has been demonstrated that the intracellular concentration of GSH (2 - 10 mM) in tumor cells is significantly higher than that in the plasma (1 - 2 μM).[95] Therefore such difference could be exploited for the selective triggering of the self-destruction of the particle within the cancer cells.

In these redox-triggered degradation tests the ss-NDs (0.1 mg/mL) were stirred at 37 °C in PBS in presence of GSH (50 mM), and a drop of the suspension was collected at several time points (exposure time up to 7 days) and analyzed by SEM and TEM (Fig. 56). Images clearly show a structural break-down of ss-NDs in presence of reducing agent, which was not detected for NDs without S-S linker stirred in the same experimental conditions. The breakdown occurs differently, depending on the doping degree of the ss-NDs. Interestingly, in the case of ss-NDs

10% already after 1 day of incubation in GSH the particles seem to undergo cracking of the structure, with big pieces of the particles remaining intact until day 7.

ss-NDs 30% instead seem to undergo a different breakdown mechanism, which involves a dissolution of the structure starting from the particle's core, rather than the neat cracking observed for ss-NDs 10%. This mechanism starts more slowly and continues until complete destruction of the particle, observed at day 7. ss-NDs 50% also undergo the dissolution mechanism observed for ss-NDs 30%, but in a slower fashion. Indeed, broken particles started to be observed only at day 5. These results clearly provide preliminary information concerning the homogeneity of the localization of the S-S linker in the NDs as well as on the difference of the breakdown mechanism, which might affect also the release properties of the particles.

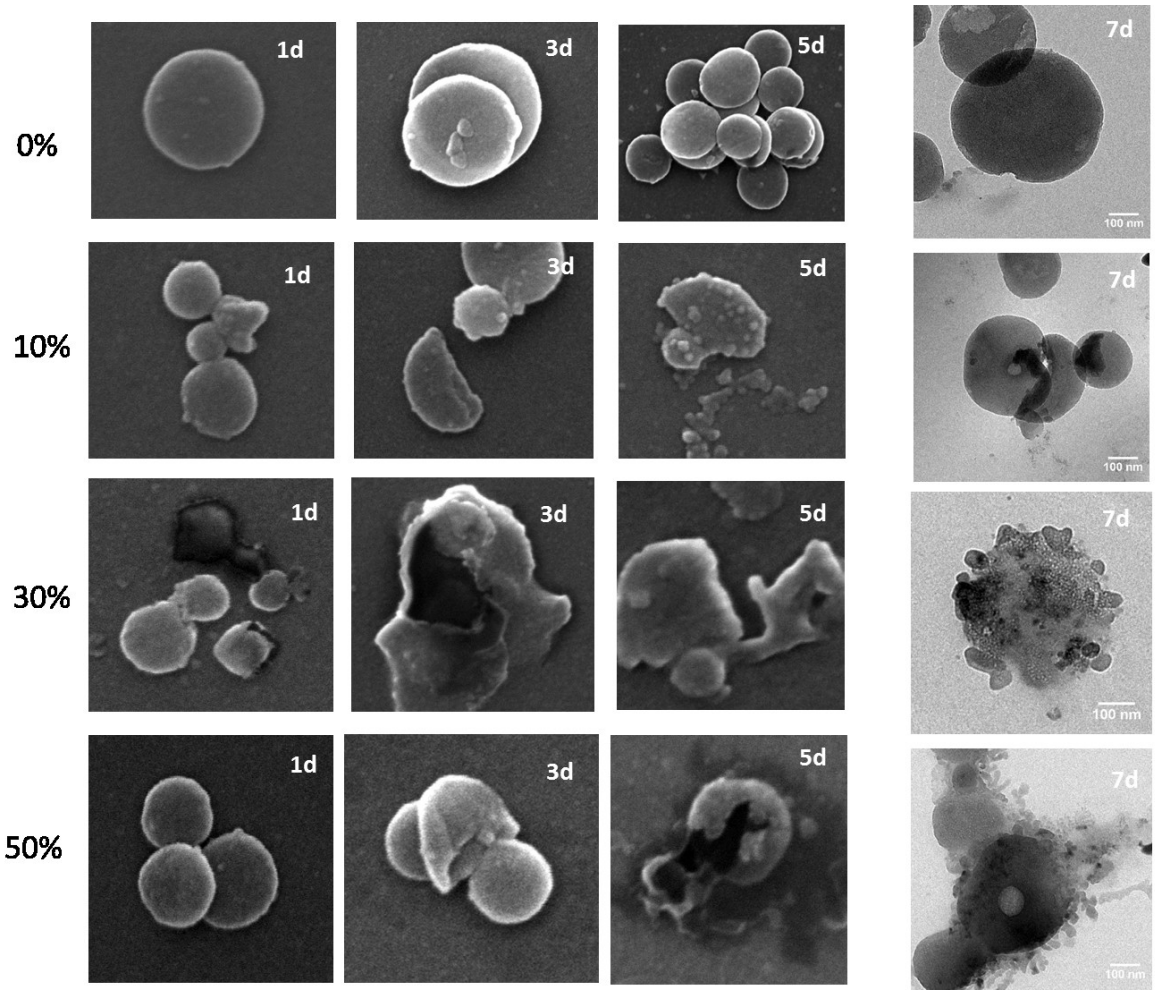

Figure 56: SEM (dx) and TEM (sx) analysis of NDs and ss-NDs 10%, 30% and 50% stirred at 37°C in presence of GSH 50 mM in PBS for 1d, 3d, 5d and 7d.

3.7.3 Drug loading and release study

To demonstrate the beneficial effect of the breakability of ss-NDs on their guest release activities, doxoribicin-loaded ss-NDs were synthesized (DOX@ss-NDs), and their release behavior investigated in the presence of 50 mM GSH. Doxorubicin, commonly used in cancer

therapy, was chosen as model compound for this set of experiments because of its photophysical properties (λ_{exc}= 480 nm, and λ_{em}= 560 nm) which would make the detection easier. Specifically, the ss-NDs (10%, 30% and 50%) and NDs were mixed with DOX in PBS (pH 7.4), for 24 h; afterward, the particles were collected *via* centrifugation and washed several times with water, in order to remove the DOX physisorbed on the surface. The loading of DOX within the particles was determined by measuring the absorption of the washing solutions and ranged from 3.5 to 4% of the ss-NDs and 4.5% of NDs. The different loaded amount of DOX much higher for un-doped NDs is according with the data on the porosimetry obtained from N_2 absorbtion analysis.

DOX@ss-NDs and DOX@NDs (0.1 mg/mL, total volume 15 mL) were then mixed with 50 mM GSH in PBS (pH 7.4) and the trend of the drug release were analyzed through UV/Vis spectroscopy at different time points (Fig.57) over a period of 4 days.

As shown in figure 57 the best release performance was obtained for the non-doped system, NDs. This result is probably accountable to the ordered porous structure possessed by NDs, which might positively influence both the loading and the release of guest molecules in the pores. Similar performance was detected for ss-NDs 10%, the hybrid with the highest degree of order in its porous structure. The release from these two particles is already reaching a plateau value after 3 hours, indicating that the molecule unload is exhaustive in very short time, and consequently in this case the effect of the reduction of the S-S bonds in the ss-NDs 10% is negligible. More complex is the behavior of ss-NDs 30% and ss-NDs 50%. These two hybrids exhibited a much slower release kinetic, which correlates to the destruction kinetic observed in the degradation experiments. In fact, in this case, the release seems strictly associated to the breakdown of the particle, with the DOX release intensifying after 1 day for ss-NDs 30%. Moreover, especially for this particle, a plateau value is not been reached in the 4 days monitored, and most probably exhaustive release will be obtained only upon complete degradation of the particle obtained at day 7.

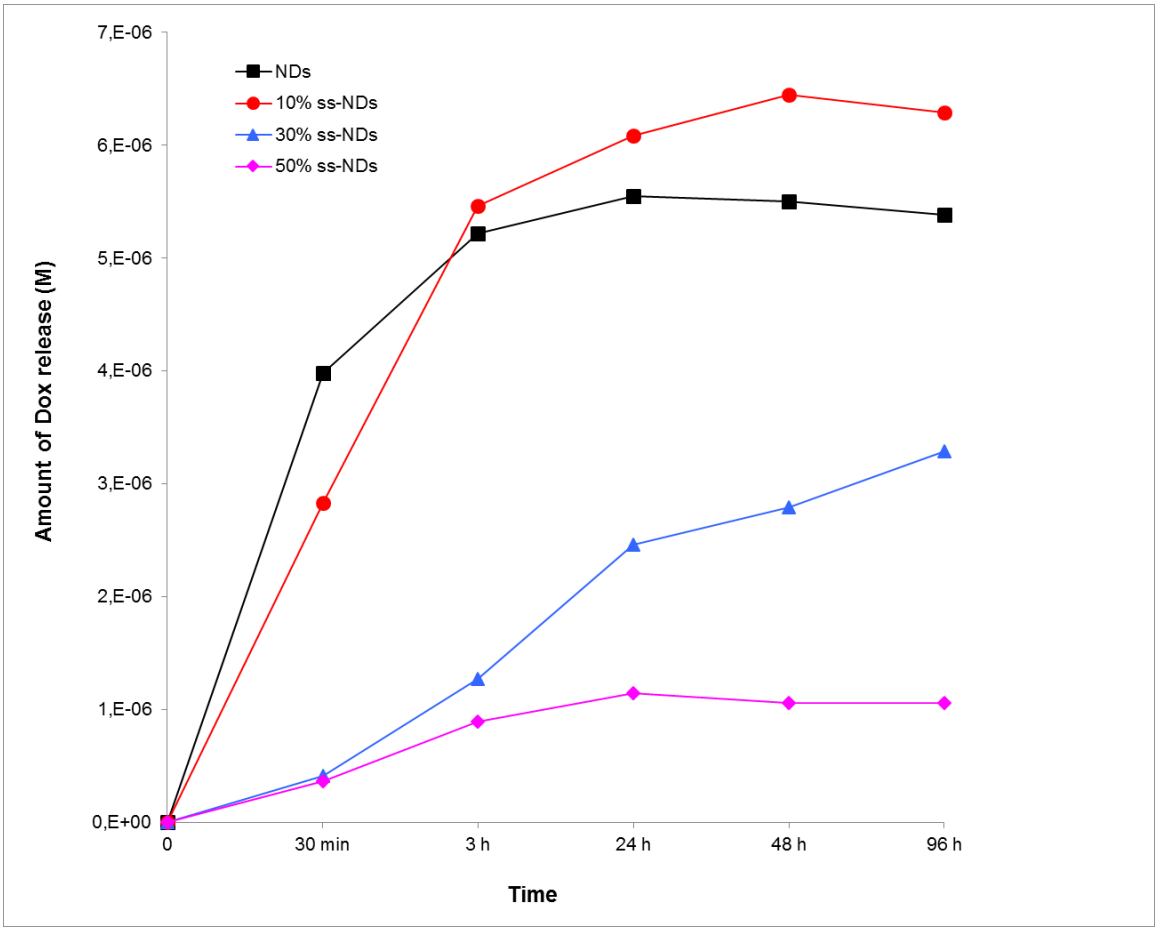

Figure 57: Doxorubicin release study in solution pH 7.4 from ss-NDs 10%, 30% and 50% compared with un-doped NDs.

3.7.4 Cellular uptake and cytoxicity of ss-NDs

To better understand the extent of the internalization of the disulfide doped NDs flow cytometry studies were performed. To perform these experiments, ss-NDs were labeled with fluorescein (FITC-ss-NDs). Specifically, fluorescein isocyanate (FITC) was covalently linked to APTES via urethane bond and then this derivative was grafted onto the surface of ss-NDs. The reaction was performed in toluene at r.t. and left overnight. The emission properties of FITC-ss-NDs were analyzed at the fluorimeter and the obtained spectra are reported in figure 59. Glioma C6 cells were incubated with a dispersion of 40 µg/mL and 80 µg/mL of NDs and ss-NDs (10%, 30% and 50%) in culture medium and subsequently washed with PBS to remove the non internalized particles. From the mean fluorescent intensity (MFI) data reported in figure 58, the internalization of NDs increases along with the increase of the doping until ss-NDs 30%, to then decrease again for ss-NDs 50%. The uptake then resulted also concentration and time dependent, still preserving the same trend. This higher tendency of the ss-NDs to be internalized by the cancer cells can be attributed to a combination of their lower surface charge and the higher hydrophobicity of the

hybrid, due to the presence of the disulfide linker in the framework of the particles. Indeed, it has been described that cellular uptake of nanoparticles results favorably influenced by an increase of the surface hydrophobicity of a particle to which a less important protein corona formation is associated.[243]

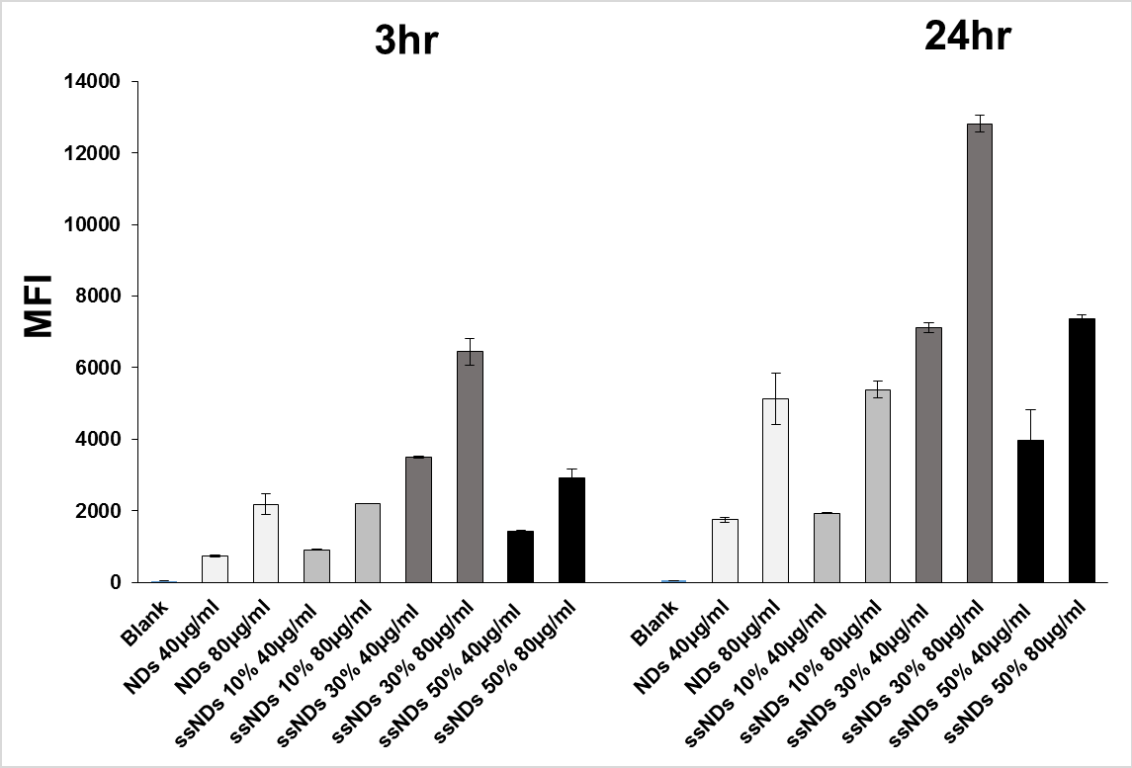

Figure 58: Cellular uptake quantitative analysis determined via flow cytometry after 24 and 48h of incubation at 37 °C of ss-NDs at concentration of 40 µg/mL and 80 µg/mL.

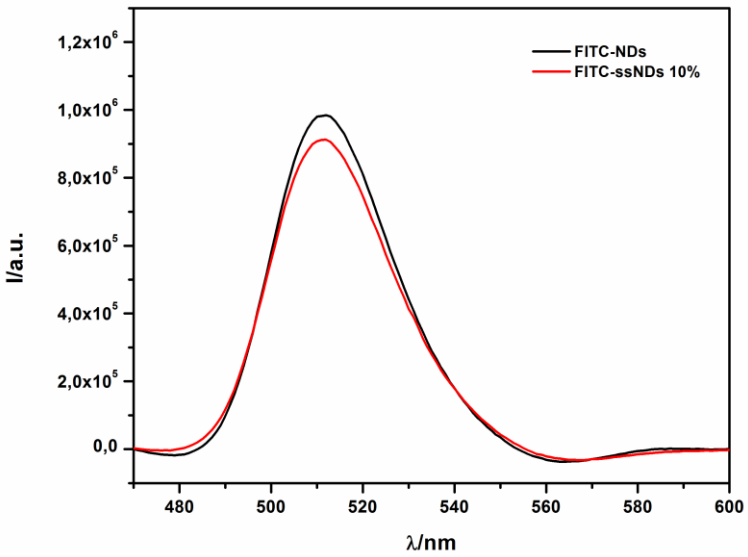

Figure 59: Emission fluorescence spectra of FITC-NDs and FITC-ssNDs 10%.

The cytotoxicity of ssNDs were also investigated in Glioma C6 cells. The cancer cells were cultured onto glass coverslips in Dulbecco's modified Eagle's medium (DMEM) containing 10% fetal bovine serum (FBS) and pen/strep (penicillin/streptomycin) at 37° C in 5% CO_2 and 95% air. After 24 h of cell growing, cells were treated with ss-NDs and NDs at different concentrations (20, 40, 80 and 100 µg/mL; Fig. 60), and the viability was measured after 72 h. Negligible cell death was detected across the concentration range tested, indicating very low cytotoxicity of the nanodiscs.

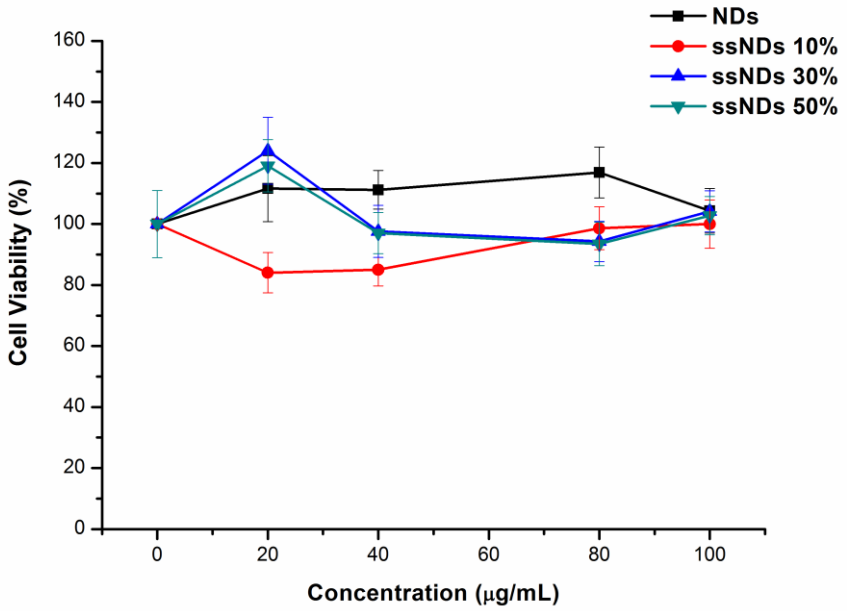

Figure 60: Cell viability of Glioma C6 cells measured after incubation for 72 h with NDs and ss-NDs 10, 30 and 50% at a concentration of 20, 40, 80 and µg/mL.

In vitro drug delivery experiments to test the beneficial effect of the breakability of ss-NDs are still ongoing. Nevertheless, here is shown the cellular uptake of DOX@NDs and DOX@ssNDs investigated by mean of confocal microscopy (Fig 61). For this set of experiments, Glioma C6 cells were seeded onto glass bottom dishes at a density of 1.5×10^4 cells per well and allowed to grow for 24 h. After the media was removed and the cells treated with 40 µg/mL of DOX@NDs and DOX@ssNDs. Free DOX (1.6 µg/mL) were also incubated with the cells for comparative purpose. After 3 or 24 hours of incubation the cells were washed with PBS and analyzed using confocal microscopy. The confocal images taken after 3h of incubation demonstrate an abundant endocytosis in particular for ss-NDs 30 and 50%, with a tendency to localize mainly in the perinuclear region (Fig. 61 A4-5). On the other hand, the images taken after 24 h of incubation shows high presence of DOX inside the nucleus only for NDs and ss-NDs 10% (Fig. 61 B2-3), highlighting the release of the drug from mesoporous structure of the

particles. Whilst, for ss-NDs 30% in spite of their much higher tendency to be internalized into cancer cells thanks their higher hydrophobicity due to the presence of disulfide linker in the framework of the particles, showed a less pronounced release of DOX (Fig. 61 B4).More complex is the behavior of ss-NDs 50%, indeed they are able to penetrate the cell membrane even after 3 hour of incubation, but it seems they formed large aggregate in the perinuclear region without release of the drug even after 24 h of incubation (Fig. 61 B5). This result is according with the data of the release profile, in which a much slower release kinetic of the drug were found for ss-ND 30 and 50% compared to un-doped NDs or ss-NDs 10%, the hybrid with the highest degree of order in its porous structure.

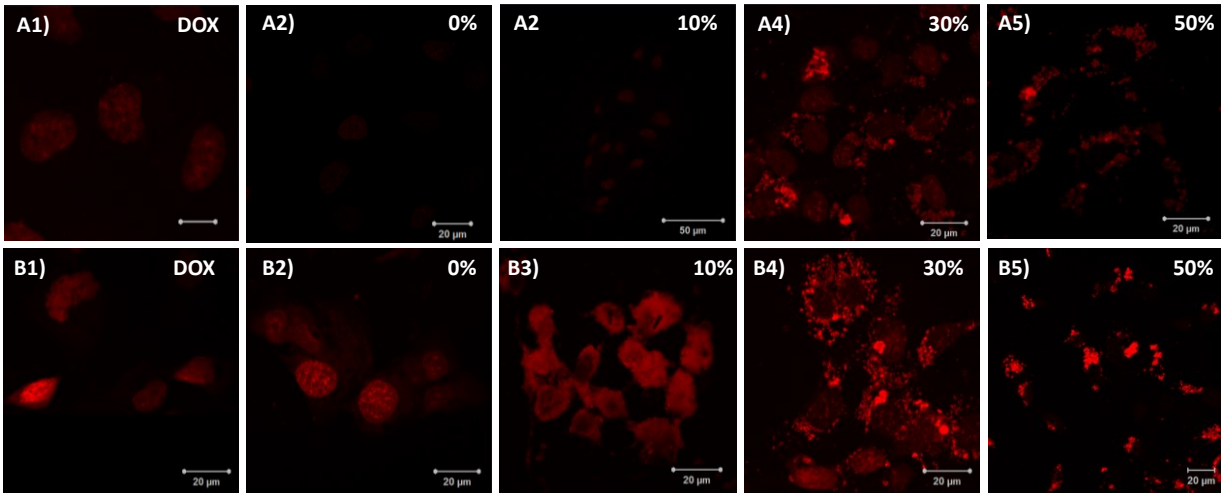

Figure 61: Confocal images of Glioma C6 cells after incubation 3 h (A1-5) and 24 h (B1-5) with DOX 1.6 µg/mL, DOX@NDs and DOX@ssNDs at 40 µg/mL.

4 CONCLUSIONS

In this doctoral work promising drug carriers were designed starting from different scaffold materials.

A family of systems using CyDs were synthesized and in particular mono-functionalized cyclodextrins or polymers based on CyD of different molecular weight in order to exploit the unique properties as solubilizer and stabilizer agents of CyDs were synergistically combined with the targeting ability of FA. CyD based nanoparticles were investigated to improve the water solubility of hydrophobic drugs, such as SOR and LA-12. In particular, the CyD polymers and oligomers (oCyD and pCyD) were found more effective than the parent CyD as solubilizer agents. The use of cross-linked CyDs increased remarkably the water solubility of the drug without any reduction of its *in vitro* cytotoxicity in all the cellular lines treated as found for SOR/CyD polymers complexes. (Fig. 62).

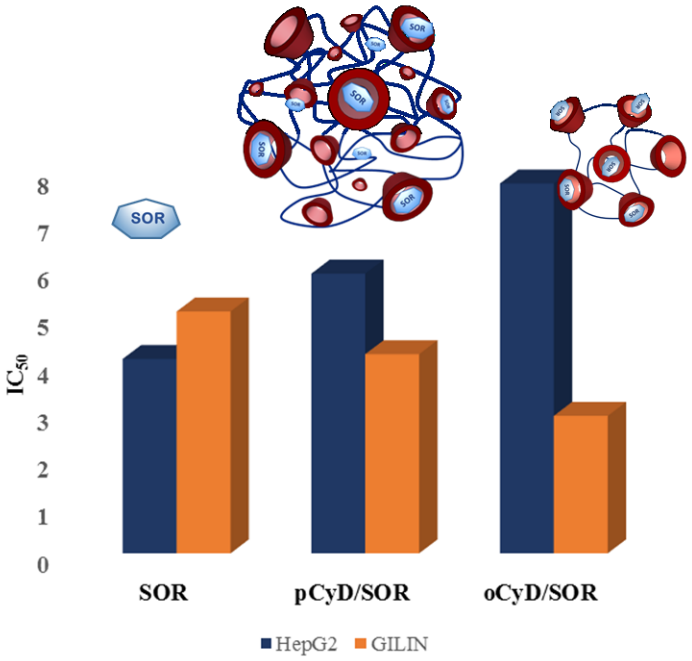

Figure 62: **IC_{50} values of SOR and its inclusion complex with pCyD and oCyD on HepG2 and GILIN cells.**

The incorporation of amino functional moiety in the backbone of the CyD polymers was also carried out gaining a useful tool for the inclusion of negatively charged drugs, such as DCF (Fig. 63). The results showed that the presence of the macromolecular arrangement, not only, does not weaken the stability of the inclusion complex with DCF, but also the presence of amino groups of $oCyDNH_2$ plays a relevant role in the recognition process.

Moreover, in all the inclusion complexes explored the results suggest that the length and size of the chain seems not to improve some of the polymer features when compared with those of

the oligomer. This finding highlights the potential of short polymeric chains as new drug carriers with a more favorable pharmacokinetic profiles.

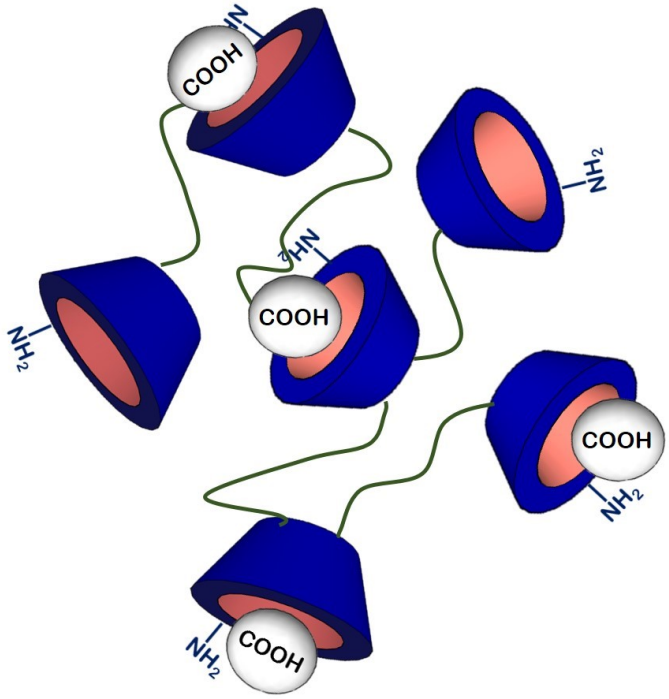

Figure 63: Schematic representation of inclusion complex between oCyDNH$_2$ and DCF.

In order to obtain targeted systems the functionalization of CyD cavity with FA was also carried out for both CyD and CyD-based polymers. Concerning the CyD conjugates, this was the first case of characterization of pure α- and γ- regioisomers of CyD-FAs. Furthermore, to widely explore the different behavior of the 3- and 6- derivatives, the first FA-conjugated CyD at its secondary side (CyD3-FA) was synthesized. For these latter derivatives, the functionalization with FA circumvents the self-inclusion of the FA side chain and makes the cavity fully available for the inclusion of the LA-12. Antiproliferative activity towards the anticancer drug LA-12 highlighted the effectiveness of these derivatives in selective cancer therapy, increasing the cytotoxic effect of the drug as a function of the different expression degree of FRs on the cell surface (Fig. 64).

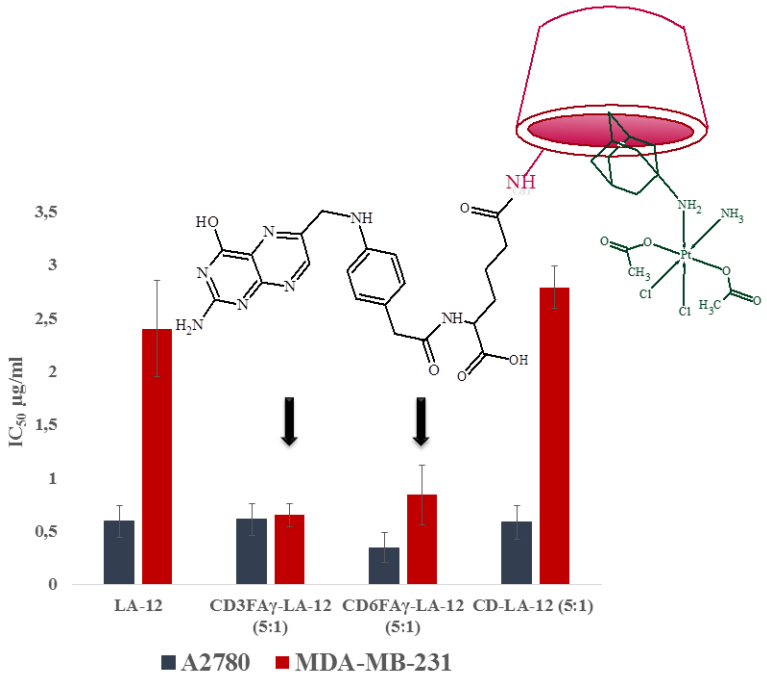

Figure 64: IC_{50} values of LA-12 and its inclusion complex with CyD-FAγ in FR (+) cancer cells.

However, when oCyDFA and pCyDFA were used for the selective vehiculation of LA-12 in FR (+) cancer cells, the beneficial effect of FA as targeting moiety resulted scant, probably because of the low accessibility of FA by the receptor due to the low extent of modification with FA (12-15% of the cavities) or to the self-inclusion of the FA units inside the CyD cavities. Interestingly, the size of the polymers seems to play a crucial role in the cytotoxic effect of the drug depending on the cellular line taking into account as shown in figure 65.

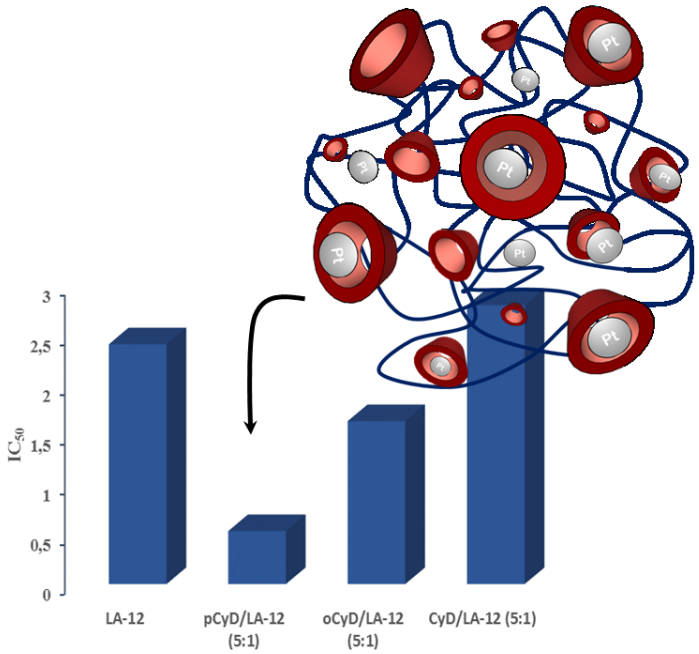

Figure 65: IC_{50} values of LA-12 and its inclusion complex with pCyD, oCyD and CyD in MDA-MB-231 cancer cells.

In the field of hard materials, a new disc-shaped mesoporous silica-based nanomaterial the nanodiscs (NDs) were synthesized. Preliminary results on the cellular uptake of NDs in cancer cells highlighted a high endocytosis for these particles, probably taking advances of their peculiar morphology. Moreover, NDs resulted able also to store large payloads within their well-ordered porous structure. This new disc-shaped material was used for the implementation into a NDs self-assembled monolayer (SAM)-based device to be employed for selective cancer cell adhesion and *in situ* release of therapeutic or diagnostic agents. For this purpose the NDs were first successfully loaded with the hydrophobic dye NR and functionalized with FA. The results showed a strong and selective adhesion of cancer cells overexpressing FRs, as well as the effective transfer of the hydrophobic dye NR from the porous structure of the NDs to the cells adsorbed onto the monolayer. This finding opens new perspectives in the usage of biocompatible tool as a mean to introduce therapeutic agents or differentiation molecules in selected cell types. The recognition process is represented in figure 66.

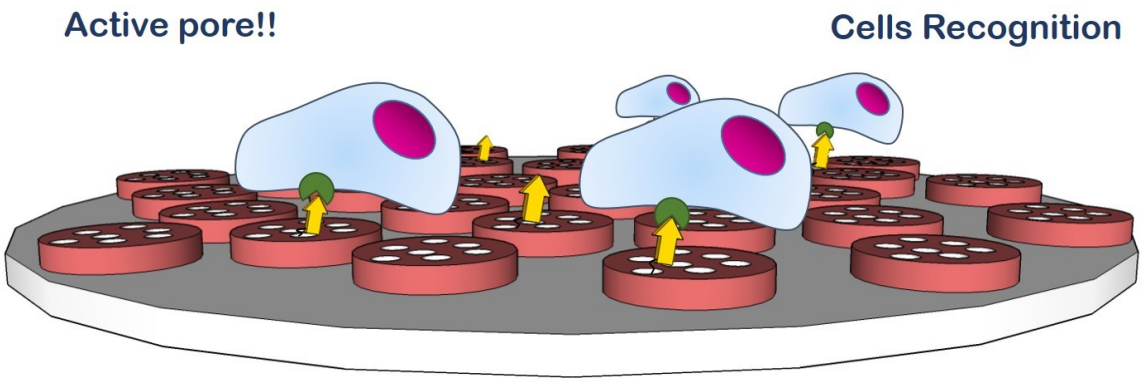

Figure 66: Schematic representation of SAM@FA of NDs for the selective recognition of FR (+) cancer cells.

Finally, in order to further increase the biodegradability of NDs within the cancerous cells, a series of redox-responsive mesoporous silica nanodiscs (ss-NDs), containing different amounts of disulfide (S-S) linkers in their framework (10%, 30% and 50%) were also developed. These hybrids resulted able to respond to reducing stimuli with a unique self-destructive behavior and an enhanced drug releasing performance (Fig. 67). The ss-NDs were found to be biocompatible towards Glioma C6 cells, and degradable in simulated physiological reductive conditions. Studies on their drug delivery and exocytosis are currently ongoing, which will be followed by external functionalization for active targeting purpose.

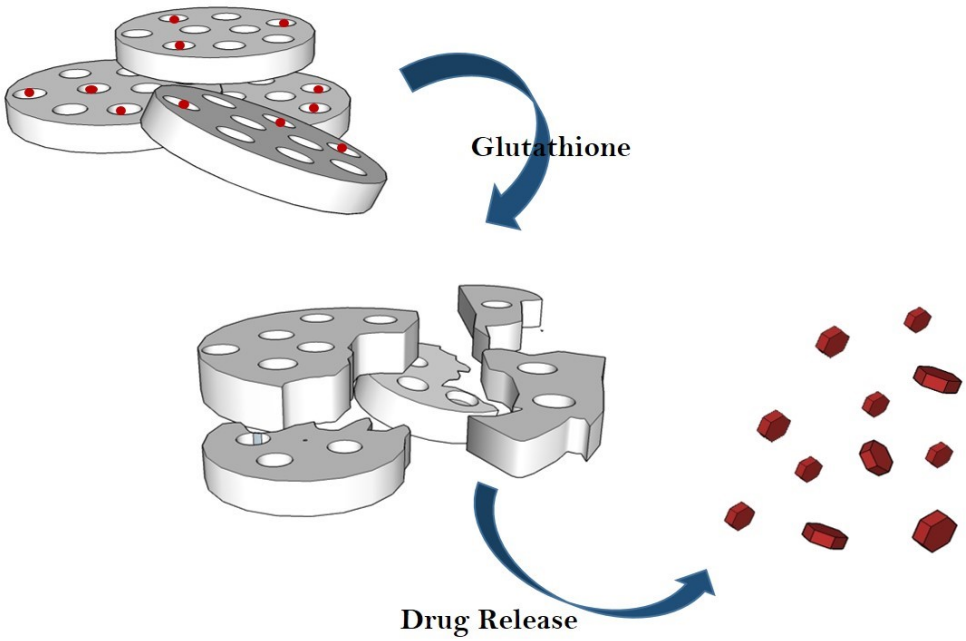

Figure 67: Schematic representation of the breakdown of ss-NDs in presence of reducing agents for enhanced drug release performance.

5 EXPERIMENTAL SECTION

5.1 Materials

All chemicals obtained from commercial sources were used without further purification: β-cyclodextrin (β-CyD, Fluka), folic acid (FA, Aldrich), anhydrous N,N-dimethylformamide (DMF, Aldrich), tetramethyl orthosilicate (TMOS, Aldrich), bis-3-triethoxysilyl-propyl disulphide (BTSPD) 3-aminopropyl triethoxysilane (APTES, Aldrich), Trimethylsilyl isothiocyanate (IC), octadecyltrimethylammonium chloride (C_{18}TACl), N,N'-Dicyclohexylcarbodiimide (DCC), n-hydroxysuccinimide (NHS), nile red (NR, Aldrich). 6A-Amino-6A-deoxy-βCyD and 3A-amino-3A-deoxy- 2A(S),3A(R)-βCyD were synthesized from the corresponding tosylates as previously described.[194,244] LA-12 was synthesized as reported elsewhere. [201] The water soluble polymer pCyD (92 kDa, 70% of CyDs) was purchased from CyClolab. DEAE and CM Sephadex 25 (Sigma–Aldrich) were used for column chromatography. Thin-layer chromatography (TLC) was performed on silica gel plates (60-F254, Merck, Darmstadt, Germany). Products were detected on TLC by UV spectroscopy or by an anisaldehyde test. Stock solutions of LA-12 and SOR were prepared in DMSO.

5.2 NMR spectroscopy

^{1}H and ^{13}C NMR spectra were recorded at 25 °C with a Varian UNITY PLUS-500 spectrometer at 499.9 and 125.7 MHz, respectively. The NMR spectra were obtained by using standard pulse programs from the Varian library. The 2D experiments (COSY, TOCSY, HSQC and ROESY) were acquired using 1 K data points, 256 increments and a relaxation delay of 1.2 s. The spectra were referred to the solvent signal. For clarity, the sugar units in CyD derivatives are labelled A–G counter-clockwise starting from the modified ring (denoted as A) and viewing from the primary hydroxyl groups.

5.3 UV/Vis and Circular dichroism spectroscopy

Spectroscopic measurement on CyDs and CyD polymers were recorded using an Agilent 8452A diode array spectrophotometer for UV/Vis spectra and a JASCO J-1500 spectropolarimeter concerning the CD measurements. The spectra represent the average of 10 scans and were recorded at 25 °C on freshly prepared aqueous solutions.

While absorbtion spectra on mesoporous materials were measured on a Shimazu UV-3600 spectrophotometer double-beam UV-Vis-NIR spectrometer and baseline corrected. Steady-state emission spectra were recorded on a Horiba Jobin-Yvon IBH FL-322 Fluorolog 3 spectrometer equipped with a 450 W xenon arc lamp, double grating excitation, and emission monochromators (2.1 nm mm^{-1} of dispersion; 1200 grooves mm^{-1}) and TBX-04 single photon-counting detector. Emission spectra were corrected for source intensity (lamp and grating) and emission spectral response (detector and grating) by standard correction curves.

5.4 Mass spectrometry

ESI-MS measurements were performed by using a Finnigan LCQ DECA XP PLUS ion-trap spectrometer operating in the negative-ion mode and equipped with an orthogonal ESI source (Thermo Electron Corporation, USA). Xcalibur software was used for the elaboration of mass spectra.

5.5 Light scattering measurements

Dynamic light scattering (DLS) measurements were carried out using a Zetasizer Nano ZS (Malvern Instruments, UK) equipped for backscattering at 173° with a 633 nm He–Ne laser. Weight average molecular weight (Mw) determination was performed through static light scattering measurements. Samples were studied at different concentrations and at 25 °C applying the Rayleigh equation, which reports the intensity of the light scattered from the oligomer/polymer solution:

$$\frac{Kc}{R\theta} = \left(\frac{1}{Mw} + 2A_2c\right) P_\theta$$

wherein R_θ is the ratio of scattered light to incident light of the sample; Mw is the weight-averaged molecular weight; A_2 is the second virial coefficient; c is the sample concentration; P_θ is the angular dependence of the sample scattering intensity; K is the optical constant defined as:

$$K = \frac{4p^2}{\lambda_0^4 N_A}\left(n_0 \frac{dn}{dc}\right)^2$$

wherein N_A, Avogadro's constant; λ_0, laser wavelength; n_0, solvent refractive index; dn/dc, differential refractive index increment. A dn/dc value of 0.137 g mL^{-1} was used as reported in

the literature for similar systems.[149] Toluene was used as the reference. $K_C/R_\theta P$ can be plotted as a function of *c*. The slope ($2A_2$) gives the second virial coefficient and the intercept (1/Mw) gives the molecular weight. Aqueous buffered solutions of oligomer (10 mM Tris buffer, pH 7.4) were filtered with nylon membrane filter (0.22 mm). The size distribution of the sample were measured during the determination of molecular weight. Triplicate measurements were carried out. Every measurement was the average of at least 12 runs.

5.6 Phase solubility studies

Phase solubility studies were performed in aqueous solutions. Excess amounts of the drugs (7 mg) were added to a 2 mL aqueous solutions containing different concentrations of β-CyD, oCyDNH_2 or pCyD in acetate buffer (10 mM, pH 5.5) when the drug was DCF or of β-CyD, oCyD or pCyD in Tris buffer (10 mM, pH 7.4) when the drug was SOR.
After an incubation time of 12 hours the solution were centrifuged to remove the unloaded drug and the supernatant were analyzed by mean of UV/Vis spectrophotometer monitoring the absorbance at 276 nm (for DCF) and at 268 nm (for SOR). Phase solubility diagrams were plotted, and the apparent stability constants (Kc) were calculated according to the following formula:

$$Kc = \alpha / S_0(1 - \alpha)$$

where S_0 represents the solubility of SOR and α represents the slope of the straight line. Sample preparation and analyses were performed at room temperature. The molar absorptivity of SOR was calculated in a water solution of pCyD or oCyD obtaining a value of 45300 and of 47000 respectively.

5.7 ITC titrations

ITC titrations were carried out at 25 °C in water (40 mM phosphate buffer, pH 6.9) by using a nano-isothermal titration calorimeter Nano-ITC^{2G} (TA Instruments, USA) having an active cell volume of 0.988 mL and a 250 or 100 μL stirring syringe. Measurements were run in the overfilled mode; the reaction mixture in the sample cell was continuously stirred at 250 rpm during the titration. Intervals between injections were 350–500 s to allow complete equilibration. The power curve (heat flow as a function of the time) was integrated through NanoAnalyze (TA Instruments, USA) to obtain the gross heat evolved/absorbed in the reaction. The instrument was chemically calibrated by titrating an HCl solution (1 mM) into buffered

Tris (30 mM containing 10 mM HCl). The equipment was also checked by running an electrical calibration. ITC measurements were carried out by titrating aqueous solution of β-CyD (14.80–16.53 mM) into a DCF solution (0.605–1.07 mM) and aqueous solutions of DCF (4.40–5.47 mM) into either pCyD (0.0108–0.0526 mM as total polymer concentration) or oCyDNH$_2$ (0.0685–0.0878 mM as total polymer concentration). Based on the average Mw and β-CyD% content of the polymers, the above total polymer concentrations correspond to "β-CyD cavity" concentrations of 0.616–2.99 mM and 0.480–0.615 mM for oCyD and oCyDNH$_2$, respectively. Solutions of both DCF and CyD derivatives were prepared by dissolving weighed amounts in 40 mM phosphate buffer (pH 6.9). Prior to the titration experiments, all solutions were degassed with gentle stirring under vacuum for about 15 min. 4-5 independent experiments were typically run for each host-guest system. The heats of dilution were determined in separate blank experiments by titrating solutions of either β-CyD or DCF (in 40 mM phosphate buffer) into a solution containing 40 mM phosphate buffer only. The net heats of reaction, obtained by subtracting the heat evolved/absorbed in the blank experiments, were analyzed by HypDH. This software determines the equilibrium constants and/or formation enthalpies of complex species in solution by a non-linear least-squares analysis of the function $U=\sum(Q_{obs} - Q_{calc})^2$, where Q_{obs} and Q_{calc} are the observed heats, corrected for the dilution (blank) effects, and the calculated heats, respectively. HypDH also allows for the simultaneous refinement of data from multiple titrations.

5.8 Scanning Electron Microscopy (SEM)

SEM images were recorded with a FEI Quanta FEG 250 instrument (FEI corporate, Hillsboro, Oregon, USA) with an acceleration voltage of 20 kV. The samples were prepared by drop-casting a dispersion of particles in EtOH (0.1 mg/mL) onto a glass cover slip, subsequently sputter coated with Au (Emitech K575X peltier cooled) for 60 s at 60 mA prior to fixation on an Al support.

5.9 Trasmission Electron Microscopy (TEM)

TEM samples were analyzed on a Hitachi 7500 instrument at an acceleration voltage of 80 kV. Ethanolic suspensions of the materials (0.1 mg/mL) were drop-casted onto Formvar coated Cu grids (400 mesh) and allowed to dry overnight prior to visualization.

5.10 X-ray Photoelectron Spectroscopy (XPS)

XPS analysis was performed using a K-Alphatm+ X-ray Photoelectron Spectrometer (XPS) System (Thermo Scientific). Monochromatic Al K alpha X-rays were used (15 keV, 72 W, 200 μm spot diameter). Spectra were measured using a pass energy of 200 V for survey spectra end 50 eV for core level spectra. The analyzed samples were prepared by drop-casting an ethanolic dispersion (0.1 mg/mL) of the particles onto a glass coverslip pre-coated with Au (Emitech K575X peltier cooled) for 3 min at 60 mA.

5.11 Thermogravimetric Analysis (TGA)

TGA analyses were conducted on a Perkin Elmer TGA4000 instrument machine under nitrogen atmosphere. The samples (0.1-2 mg) were kept at 100°C for 30 minutes for stabilization, then heated from 100 to 750 °C at a speed of 10 °C/min, before being held at this temperature for further 30 minutes, and finally cooled. The analyses were performed under a gas flow of N_2 at 60 mL/min.

5.12 Nitrogen Adsorbtion Analisys

Porosimetry analyses of the samples were performed using a Micromeritisc porosimeter (model ASAP-2020). The samples were degassed at 150 °C for 3h and N_2 adsorbtion/desorbtion measurement was done at -196 °C. The surface areas and pore volume were calculated by BET methods and the pore size distribution was calculated by DFT methods.

5.13 Small Angle X-ray Scattering (SAXS)

The small-angle X-ray scattering set-up comprised the SAXSess small-angle X-ray scattering instrument from Anton Paar GmbH, containing a slit collimation system, and the PW3830 laboratory X-ray generator (40 kV, 50mA) with a long-fine focus sealed X-ray tube (CuKα wavelength of λ = 0.1542 nm) from PANalytical. Detection was performed with the 2D imaging-plate reader Cyclone® by Perkin Elmer. Measurements were performed on powder sample for 2 min and the data collected up to a scattering vector q value of 7 nm^{-1}, where $q = (4\pi/\lambda)\sin(\theta/2)$ and 2θ the scattering angle. Powder samples were held in tape, and the tape background was subtracted before the scattered intensity was corrected for the slit geometry

smearing by using the Lake method. The 2D data were converted to 1D data by using SAXSQuant software (Anton Paar GmbH, Austria).

5.14 Reduction of ss-NDs with GSH

ss-NDs were suspended in a PBS solution of glutathione (GSH 50 mM) with a concentration of 0.1 mg/mL (total volume of 15 mL). The solution was initially sonicated for 10 minutes and then kept at 37 °C while stirring. Aliquots of 1.5 mL were taken at different time points (from 0 to 7 days) for SEM and TEM analysis. Control experiments using NDs in presence of 50 mM of GSH were also performed under the same conditions.

5.15 DOX loading of the NDs and ss-NDs

A mixture of NDs (5 mg), DOX (2 mg), and 1 mL of PBS (10 mM, pH 7.4) was prepared in an eppendorf tube, sonicated 5 min in a bath at 37°C, and finally stirred overnight at room temperature. The DOX loaded NDs were hence collected by centrifugation (15 min at 10 krpm). The samples were washed several times with water, and dried for few hours under vacuum. The loading and washing solution supernatants were kept to determine the DOX loading.

5.16 Evaluation of the effects of the reduction of ss-NDs on guest release

Doxorubicin (DOX) loaded ss-NDs were suspended (0.1 mg/mL) in a PBS solution of GSH (50 mM). The solution (total volume of 15 mL) was initially sonicated for 10 minutes and then kept at 37 °C while stirring. Aliquots of 1.5 mL were taken at different time points (from 0 to 4 days) for UV/Vis measurement. The aliquots were centrifuged for 10 min and the supernatants analysed by UV/Vis spectroscopy.

5.17 Confocal Microscope

Confocal imaging was performed with a Zeiss LSM 710 confocal microscope system equipped with a 63x magnification, numerical aperture 1.3 of Zeiss LCI Plan- NEOFLUAR water immersion objective lens (Zeiss GmbH, Germany).

5.18 Cell culture

Ovarian carcinoma A2780 and ductal breast epithelial carcinoma T47-D cells were grown as monolayers in RPMI medium (Euroclone, Pero, Italy) supplemented with 10% fetal bovine serum (FBS, Euroclone). The medium of T47-D was supplemented with insulin (5 UmL^{-1}). Breast carcinoma MDA-MB-231 and MCF-7 cells were grown in Dulbecco's modified Eagle's medium (DMEM, Euroclone) supplemented with 10% FBS and 1% penicillin–streptomycin (Euroclone).

Hela and Glioma C6 cells were cultured in a media composed as follows: 88% Dulbecco's Modified Eagle Medium (DMEM), 10% Fetal Bovine Serum, 1% Penicillin-Streptomycin and 1% L-Glutamine 200 mM. The cell culture was performed under 5% CO_2, and at 37 °C. Detachment of the cells from the culture flask was performed by trypsination.

5.19 Cell counting

The cell viability was determined using a CASY® Cell Counter and Analyser machine (system model TT, Roche).

5.20 Flow Cytometry (FACS analysis)

Samples were acquired on a LSRII cytometer (Becton Dickinson Biosciences, San diego, CA, USA). Quality control was performed regularly using cytometer setup & tracking beads (BD Biosciences) to ensure consistency of fluorescence intensity measurements throughout all experiments. Cell debris and dead cells were excluded using Forward scatter area and side scatter area and cell aggregates were excluded using Side Scatter Width and Side Scatter Area. Fluorescein fluorescence of 5000 living single cells was analyzed after monoparametric acquisition using the FL 2 Area parameter (excitation with a 488 nm Blue Laser, 575/26 nm emission filter). FACSDivaTM software version 6.1.2. (BD Biosciences) was used for data analysis and graphical output. Data are expressed as the ratio of Median Fluorescence Intensity (MFI) of the test sample to the MFI of the control cells, cultured in the absence of nanoparticles, in parallel with test samples.

5.21 Cell staining

HeLa cells (1×10^6 /mL) were suspended in a serum-free culture medium, and the DiO dye (5 µL/mL, λ_{exc} = 488 nm, λ_{em} = 501 nm) was added. The suspension was then gently mixed and incubated for 10-20 minutes at 37 °C, before being centrifuged at 1500 rpm for 5 min. The supernatant was finally removed, and the cells gently resuspended in fresh medium at 37 °C. The washings were repeated twice.

5.22 Cell adhesion onto SAMs and counting

The monolayers were washed with PBS solution to remove all the impurities. The SAMs, either naked or functionalized with folic acid, were placed in a 24 well plate (diameter 4 cm) and seeded with cells (1×10^5 HeLa,). Each plate was covered with the culture medium (2 mL) and incubated for 30 min. Then the culture medium was removed, the plates washed twice with PBS (5 mL) and fixed with PFA (3 mL). After 10 minutes, PFA was removed, and the plates were washed twice with bi-distilled water (5 mL) and mounted on microscopy glass for confocal microscope analysis. The cells counting is an average of three values each referred to a surface of 0.0015 cm^2. This averaged value is then normalized to the total area of the monolayer, 1 cm^2.

5.23 FACS sample preparation for NDs and ss-NDs

Glioma C6 cells were seeded in a 24-well cell culture plate at a density of 5×10^3 cells per well and allow to grow for 24 h. After this time, the cells were treated with 40 and 80 µg/mL of NDs and ss-NDs (10%, 30% and 50%) and incubated for 3, 14 and 48 hours. Control cells were treated with equivalent volumes of culture media. After incubation with the particles cells were trypsinated, centrifuged for 3 min at 1 krpm and the resultant pellet was re-suspended in 500 µL of PBS. Cells were centrifuged one more time and finally the pellet was re-suspended in 500 µL with PBS (4% PFA) for FACS measurements.

5.24 Confocal images of C6 Glioma cells treated with FITC-NDs

For this experiment Glioma C6 cells were seeded onto glass cover slips in a 24-well cell culture plate at a density of 1.5×10^4 cells per well and allowed to grow for 24 h. Afterwards, the media

was removed and fresh media containing FITC-NDs at a concentration of 50 and 100 μg/mL was added to the cells and incubated for 3 h at 37 °C in a humidified atmosphere with 5% CO_2. Afterwards cells were then washed 5 times with PBS and fixed with 4% PFA. In order to visualize the nuclear region, the nucleus was stained with DAPI and washed three times with PBS. The glass cover slips were mounted onto glass slides for confocal microscopy measurements. The excitation wavelength for DAPI was 405 nm, and for FITC was 490 nm.

5.25 Cellular staining for Z-stacking of FITC-NDs

Glioma C6 cells were prepared as previously explained for the cellular uptake experiment and incubated with FITC-NDs under the same conditions. After 24 h of incubation cells were washed 5 times with PBS and fixed with 4% PFA. Cells were then washed with PBS and kept in 0.1% Triton X-100 in PBS for 10 minutes and afterwards in 1% bovine serum albumin (BSA) in PBS for 20 min. The cell layer on glass cover slip was stained with Phalloidin Alexa Fluor® 647, for F-actin/membrane staining, for 20 min, in the dark at room temperature, and washed twice with PBS. The nuclear region was stained with DAPI. The cover slips were mounted onto glass slides for confocal microscopy measurements. The excitation wavelength for DAPI and Phalloidin Alexa Fluor® 647 were 405 and 650 nm respectively.

5.26 Confocal images of C6 Glioma cells treated with DOX loaded NDs and ss-NDs

Glioma C6 cells were seeded onto glass bottom dishes at a density of 1.5×10^4 cells per well and allowed to grow for 24 h. Next, the media was removed and fresh media containing DOX loaded NDs and ss-NDs (10%, 30%, 50%) at a concentrations of 40μg/mL was added to the cells and incubated for 3, 24 and 48h at 37 °C in a humidified atmosphere with 5% CO_2. Free DOX in PBS were also incubated with the cells under the same conditions for comparison purposes. After the incubation times cells were then washed 5 times with PBS and fixed with 4 % PFA. The glass cover slips were mounted onto glass slides for confocal microscopy measurements. The excitation wavelength for DOX was 470 nm.

5.27 Cytotoxicity of NDs and ss-NDs

Glioma C6 cells were seeded in a 24-well cell culture plate at a density of 3×10^4 cells per well and allowed to grow for 24 h. After this time, the cells were treated with 20, 40, 80 and 100 µg/mL of nanodiscs, and control cells were treated with equivalent volumes of culture media. Cells were incubated for 72 h, after which they were trypsinated, centrifuged for 3 min at l krpm and the resultant pellet was re-suspended in l mL of culture media. Cell viability was measured using CASY® Cell Counter and Analyzer.

5.28 Determination of antiproliferative activity by MTT assay

Cell lines were plated (180 µL of a suspension of appropriate concentration) into flat-bottomed 96-well microtiter plates. After 6–8 h of incubation, cells were treated with the selected complexes (five solutions (20 µL) in a dilution ratio of 1:5 (starting from 10 µM concentration) and processed by the MTT assay (3-(4,5-dimethylthiazol- 2-yl)-2,5-diphenyltetrazolium bromide). The stock solutions of LA-12 and SOR were freshly prepared in DMSO (2%). The final concentration of DMSO in the cell culture medium did not exceed 0.2%. CyDs, CyD polymers and their FA derivatives were used starting from 50 µM concentration. IC_{50} values were calculated on the basis of the analysis of single concentration–response curves. The Cricket Graph III software was used to analyse the concentration–response curves.

The Mann-Whitney test for non-parametric data was used for statistical analysis. The number of data points for each experimental group ranged from 4 to 7.

5.29 Synthesis of Folate N-hydroxysuccinimide (FA-NHS)

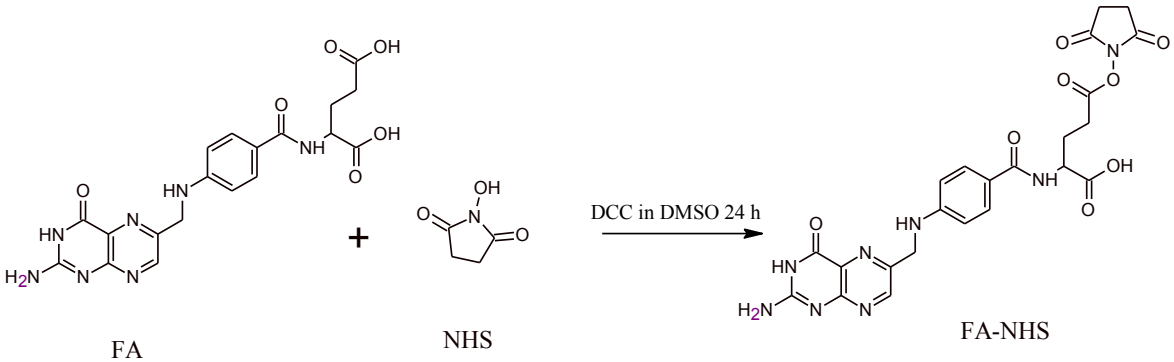

FA NHS FA-NHS

Folate N-hydroxysuccinimide (FA-NHS) was synthesized according to the method of Lee and Low.[245] Folic acid (500 mg, 1.13 mmol) was dissolved in DMSO (10 mL) in the presence of

trimethylamine (TEA, 20 µL) and reacted with N-hydroxysuccinimide (NHS, 30 mg, 1.13 mmol) and dicyclohexylcarbodiimide (DCC, 233 mg, 1.13 mmol) for 12 h at room temperature in the dark. The reaction mixture was filtered to remove the precipitated side product dicyclohexylurea, and the filtrate treated with diethyl ether to allow precipitation of FA-NHS. The yellow-orange precipitate was collected by filtration of the mother liquor and stored at -20 °C.

5.30 Synthesis of 3A-deoxy-3A-(pteroyl-glutamylamine)-2A(S),3A(R)-βCyD (CyD3-FA)

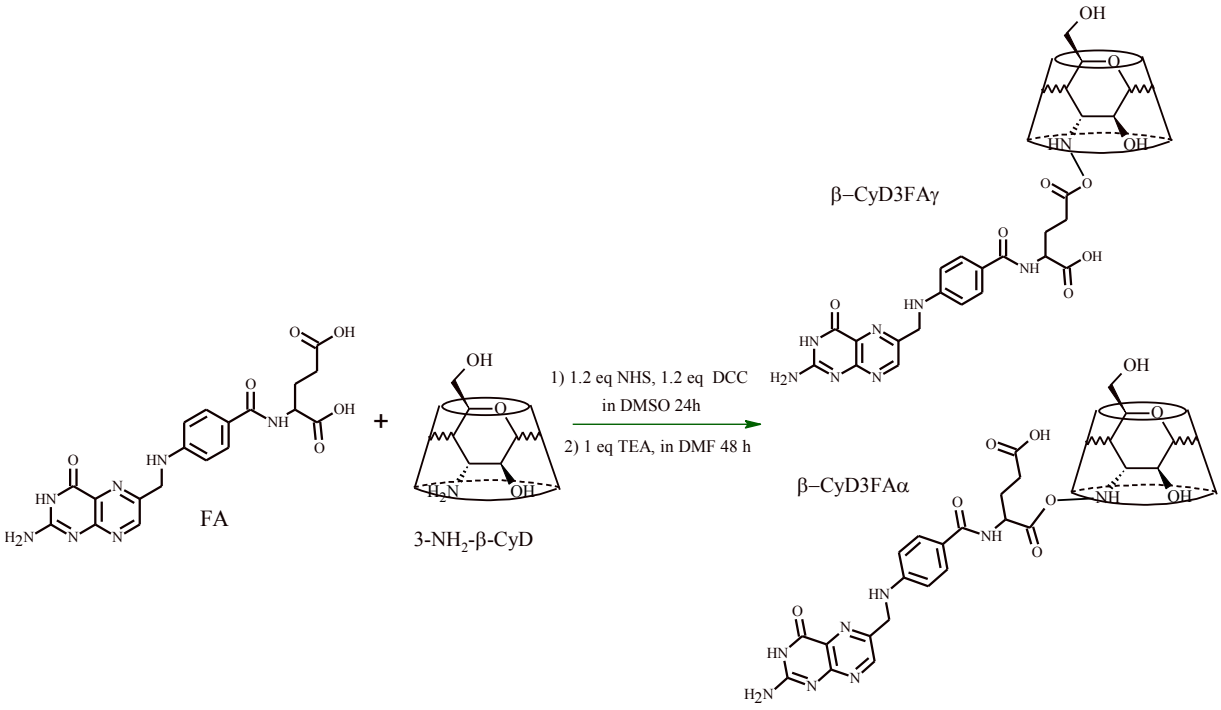

FA-NHS (237 mg, 0.4 mmol) and 3A-amine-3A-deoxy-2A(S),3A(R)-βCyD (50 mg, 44.6 mmol) were dissolved in dry DMF (10 mL), TEA (10 µL) was added and the reaction mixture was stirred at room temperature for 48 h. The solvent was evaporated to dryness *in vacuo*. The product was suspended in Milli-Q water (3.0 mL) and purified by anion-exchange liquid chromatography (DEAE Sephadex A-25, HCO_3^- form) using a linear gradient of NH_4HCO_3 (0 →0.3M). Two products, corresponding to α and γ regioisomers of the conjugate CyD3-FA, were obtained.

CyD3-FAγ:

Yield: 45%.

TLC: Rf 0.68 (PrOH/AcOEt/H_2O/NH_3 4:2:4:1).

ESI-MS *m/z*: 777.2 $[M-2H]^{2-}$, 1555.5 $[M-H]^-$.

CD (H_2O), λ/nm (Δε): 220 (1.1), 290 nm (1.2).

^{1}H NMR (500 MHz, D_2O) δ (ppm): 8.67 (s, 1H; H-7 of FA), 7.50 (m, 2H; H-13 and H-15 of FA), 6.56 (m, 2H; H-12 and H-16 of FA), 5.04-4.74 (m, 7H; Hs-1 of CyD), 4.56 (s, 2H; H-9 of FA), 4.58 (m, 1H; H-3 of CyD), 4.34 (m, 1H; H-19 of FA), 3.98-3.10 (m, 41H; Hs-6, Hs-5, Hs-4, Hs-3, Hs-2 of CyD), 2.42 (m, 1H; H-22 of FA), 2.22 ppm (m, 3H; Hs-21 and H-22' of FA).

CyD3-FAα:

Yield: 20%.

TLC: Rf 0.69 (PrOH/AcOEt/H_2O/NH_3 4:2:4:1).

ESI-MS *m/z*: 777.4 $[M-2H]^{2-}$, 1555.4 $[M-H]^-$.

CD (H_2O), λ/nm (Δε): 220 (-2.9), 235 (2.3), 270 (3.3), 300 nm (3.5).

^{1}H NMR (500 MHz, D_2O) δ (ppm): 8.48 (s, 1H; H- 7 of FA); 7.52 (d, *J*=8.4 Hz, 2H; H-13 and H-15 of FA); 6.52 (d, *J*= 8.2 Hz, 2H; H-12 and H-16 of FA); 5.04 (d, *J*=2.8 Hz, 1H; H-1 of CyD); 4.95 (d, *J*=2.9 Hz, 1H; H-1 of CyD); 4.93 (d, *J*=3.4 Hz, 1H; H- 1 of CyD); 4.91 (m, 2H; H-1 of CyD); 4.87 (d, *J*=3.3 Hz, 1H; H-1 of CyD); 4.76 (bs, 1H; H-1A of CyD), 4.54 (m, 2H; H-9 of FA) ; 4.41 (bs, 1H; H-3A of CyD), 4.33‑4.13 (m, 2H; H-3G, H-3X of CyD and H-19 of FA); 4.06‑3.30 (m, 36H; H-6, H-5A, H-5, H-4, H-3, H-2 of CyD); 3.11 (d, *J*=11.1 Hz, 1H; H-6Y of CyD); 3.04‑2.90 (m, 2H; H-5A and H-6aY of CyD), 2.49 (m, 2H; Hs-22 of FA); 2.25 ppm (m, 2H; Hs-21 of FA).

5.31 Synthesis of 6A-deoxy-6A-(pteroyl- glutamylamine)-βCyD (CyD6-FA)

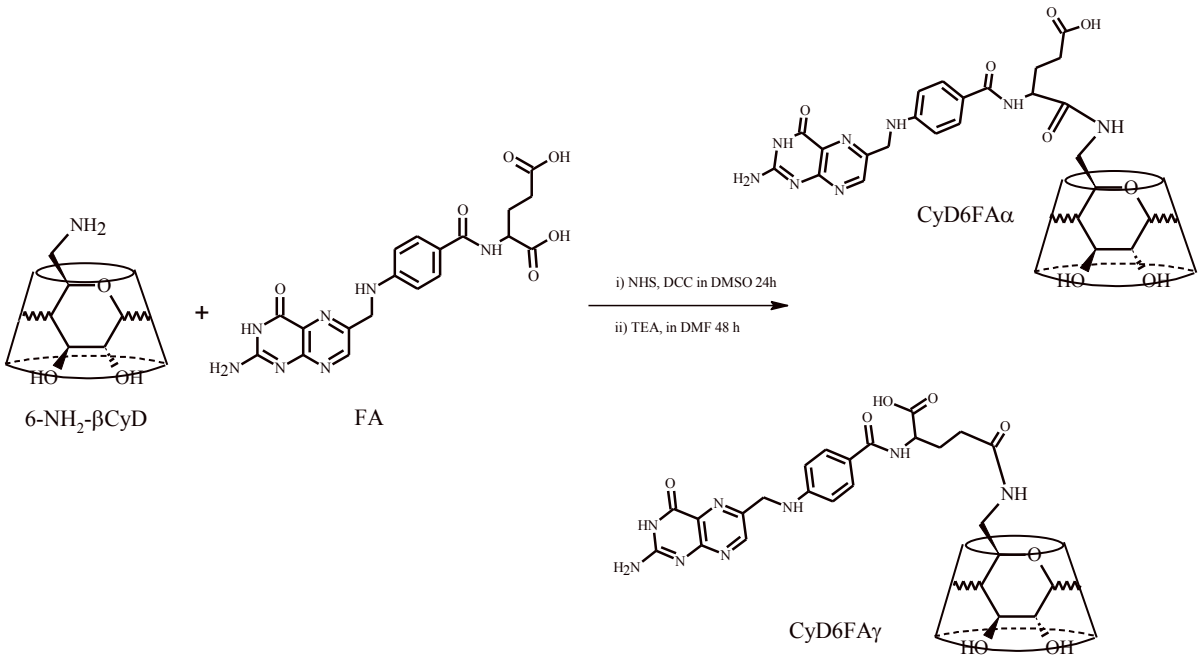

FA-NHS (220 mg, 0.3 mmol) and 6A-amino-6A-deoxy-βCyD (110 mg, 97 mmol) were dissolved in dry DMF (4 mL), TEA (20 µL) was added and the reaction mixture was stirred at room temperature for 48 h. The solvent was evaporated to dryness *in vacuo* and the solid residue was dissolved in Milli-Q water (3 mL) and purified by ion-exchange liquid chromatography (DEAE Sephadex, HCO_3^- form) using a linear gradient of NH_4HCO_3 (0 → 0.3 M). Two products, corresponding to the α and γ regioisomers of the conjugate βCyD6-FA, were obtained.

CyD6-FAγ:

Yield: 40%.

TLC: Rf 0.56 (PrOH/AcOEt/H_2O/ NH_3 4:2:4:1).

ESI-MS *m/z*: 777.2 $[M-2H]^{2-}$, 1555.2 $[M-H]^-$.

CD (H_2O), λ/nm (Δε): 204 (38.1), 230 (-2.3), 250 (-3.1), 275 (9.2), 306 nm (4.4).

^{1}H NMR (500 MHz, D_2O) δ (ppm): 8.42 (s, 1H; H-7 of FA), 7.29 (d, *J*=8.4 Hz, 2H; H-13 and H-15 of FA), 6.55 (d, *J*= 8.3 Hz, 2H; H-12 and H-16 of FA), 4.99 (m, 2H; H-1 of CyD), 4.97 (m, 2H; H-1A and H-1 of CyD), 4.91 (d, 1H; H-1 of CyD), 4.89 (d, *J*= 3.6 Hz, 1H; H-1 of CyD), 4.84 (d, *J*=3.1 Hz, 1H; H-1 of CyD), 4.69 (m, 2H; H-9 of FA), 4.26 (t, *J*=3.2 Hz, 1H; H-19 of FA), 4.13 (d, *J*= 11.2 Hz, 1H; H-6X of CyD), 4.04 (d, *J*=14.4 Hz, 1H; H-6b A of CyD), 3.96 (m, 1H; H-3Y of CyD), 3.89‑3.28 (m, 34H; H-6, H-5A, H-5, H-4, H-3, H-2 of CyD), 3.20

(t, *J*=9.2 Hz, 1H; H-4A of CyD), 3.14 (m, 1H; H-3G of CyD), 3.09 (d, *J*=9.8 Hz, 1H; H-3G of CyD), 3.03 (m, 2H; H- 3X of CyD), 2.60 (dd, *J*=14.4, 10.9 Hz, 1H; H-6a A of CyD), 2.49 (m, 1H; H-21b of FA), 2.25 (dd, *J*=16.2, 7.4 Hz, 1H; H-22b of FA), 2.10 (dd, *J*=16.2, 12.5 Hz, 1H; H-22a of FA), 1.93 ppm (dd, *J*=13.6, 7.4 Hz, 1H; H-21a of FA).

^{13}C NMR (125 MHz, D_2O) δ (ppm): 147.40 (C-7 of FA), 128.3 (C-13 and C-15 of FA), 113.7 (C-12 and C-16), 104‑101 (C-1 of CyD), 87.0 (C-4A), 82.9‑81.2 (Cs-4), 80.8‑76.2 (C-5, C-3), 63.6‑60.7 (Cs-6), 62.2 (C-6X of CyD), 58.6 (C-19 of FA), 48.9 (C-9 of FA), 41.8 (C-6A), 73.6 (C-3Y of CyD), 72.3 (C-3G of CyD), 73.4 (C-3X of CyD), 32.5 (C-22 of FA), 28.7 ppm (C-21 of FA).

CyD6-FAα:

Yield: 12%.

TLC: Rf: 0.50 (PrOH/AcOEt/H_2O/NH_3 4:2:4:1).

ESI-MS *m/z*: 777.3 $[M-2H]^{2-}$, 1555.5 $[M-H]^-$.

CD (H_2O) λ/nm (Δε): 205 (23.1), 225 (-4.4), 275 (3.1), 305 nm (2.5).

^{1}H NMR (500 MHz, D_2O) δ (ppm): 8.40 (s, 1H; H- 7 of FA), 7.43 (d, *J*=8.7 Hz, 2H; H-13 and H-15 of FA), 6.57 (d, *J*= 8.6 Hz, 2H; H-12 and H-16 of FA), 5.02 (d, *J*=3.6 Hz, 1H; H-1 of CyD), 5.00 (d, *J*=3.6 Hz, 1H; H-1G of CyD), 4.98 (d, *J*=3.8 Hz, 1H; H-1 of CyD), 4.96 (d, *J*=3.0 Hz, 1H; H-1 of CyD), 4.86 (d, *J*=3.5 Hz, 2H; H-1A and H-1B of CyD), 4.82 (m, 1H; H-1X of CyD), 4.69 (m, 2H; H-9 of FA), 4.30 (d, *J*=14.8 Hz, 1H; H-5A of CyD), 4.13 (d, *J*= 10.9 Hz, 1H; H-6bG of CyD), 4.02 (m, 2H; H-6aG of CyD and H-19 of FA), 3.99-3.30 (m, 34H; H-6, H-5, H-4, H-3, H-2 of CyD), 3.20 (m, 1H; H-4A of CyD), 3.15 (m, 1H; H-6bA of CyD), 3.02 (m, 1H; H-3B of CyD), 2.88 (m, 1H; H-3X of CyD), 2.71‑2.66 (m, 1H; H-6A of CyD), 2.61 (m,1H; H-22b of FA), 2.23 (m, 1H; H-22 of FA) 2.16 (m, 1H; H- 21b of FA), 1.98 ppm (m, 1H; H-21 of FA).

^{13}C NMR (125 MHz, D_2O) δ (ppm): 145.91 (C-7 of FA), 134.3 (C-13 and C-15 of FA), 112.2 (C-12 and C-16), 104‑101 (C-1 of CyD), 82.9‑81.2 (Cs-4), 80.8‑76.2 (C-5, C-3, C-2), 68.5 (C-2A), 63.6-60.7 (Cs-6), 58.9 (C-19 of FA), 47.5 (C-9 of FA), 35.0 (C-22 of FA), 27.5 ppm (C-21 of FA).

5.32 Synthesis of 3A-tert-Butoxycarbonyl-amino-3A-deoxy-2A(S),3A(R)-βcyclodextrin (CyD3NHBoc)

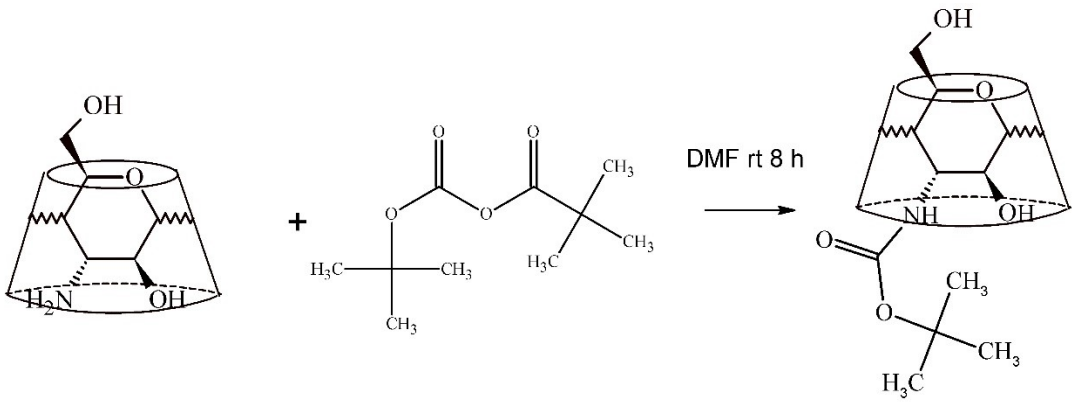

$CyD3NH_2$ (Boc)2O CyD3NHBoc

3A-Amino-3A-deoxy-2A(S),3A(R)-β-CyD (100 mg, 88.1 mmol) and di-tert-butyldicarbonate (19.24 mg, 88.1 mmol) were dissolved in dry DMF and the reaction mixture was stirred at room temperaturefor 8 h. The solvent was evaporated to dryness *in vacuo*. The crude product was suspended in water and purified by dialysis (Float-A-LyZer G2, MWCO 1000). The product (CyD3NHBoc) was freeze dried to give a white powder.

Yield: 91%

TLC: Rf = 0.56 (PrOH/AcOEt/H_2O/NH_3 5 : 2 : 2 : 4).

ESI-MS *m/z*: 1234.4 $[M+H]^+$.

5.33 Synthesis of amino-oligomer oCyDNH$_2$

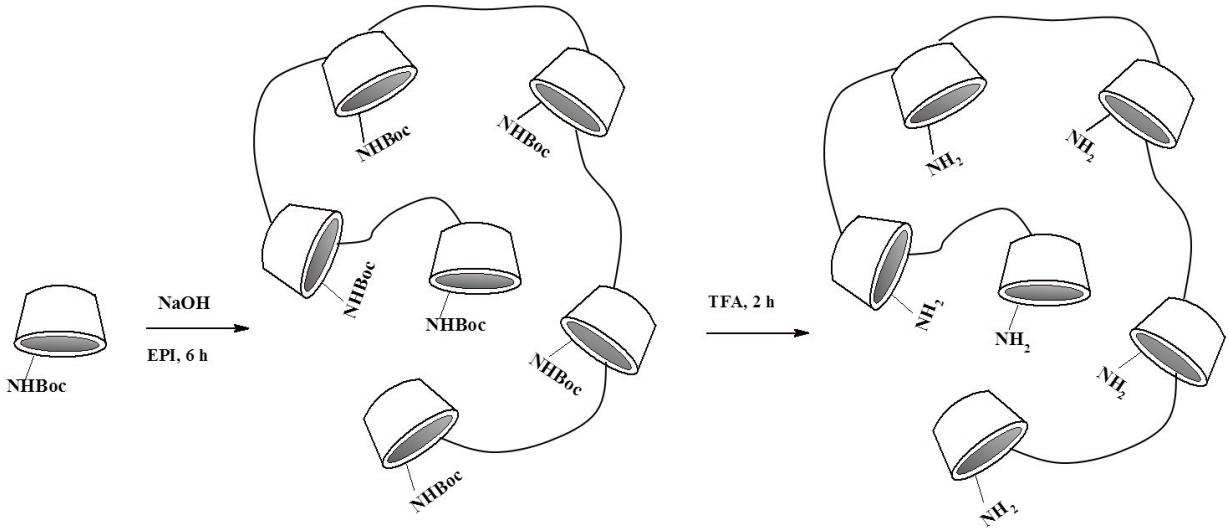

500 mg of CyD3NHBoc (0.4 mmol) in 3 mL of a 7 M NaOH solution was stirred overnight at room temperature. EPI (0.160 mL, 2 mmol) was slowly added and the mixture was heated to 40 °C. After 6 h, acetone was added and a gel was obtained, after decantation acetone was removed and the suspension was maintained at 50 °C for 12 h. Then HCl 6 N was added until neutral pH and the mixture was ultra-filtrated (molecular weight cut-off 5000). The final product was precipitated by ethanol and dried under vacuum to obtain Boc protected oCyDNH$_2$. oCyDNHBoc was deprotected by reaction with TFA for 2 h and purified through ultra-filtration. Finally, the product was freeze dried to give a white powder.

Yield: 68%.

oCyDNHBoc:

^{1}H NMR (500 MHz, D_2O) δ (ppm): 5.18–4.82 (7H, m, H-1), 4.25–3.20 (60H, m, H-5, -6, -3, -2, -4, EPI protons), 1.45 (9H, bs, Boc).

^{13}C NMR (125.7 MHz, D_2O) δ (ppm): 156.5 (CO), 102–100 (C-1), 80 (C-4), 75–67 (C-5, C-3, C-2, CH-EPI), 63 (CH_2OH of chains), 62 (C-6), 60 (CH_2 of chains), 28.0 (Boc CH_3).

oCyDNH$_2$.

^{1}H NMR (500 MHz, D_2O) δ (ppm): 5.20–4.82 (7H, m, H-1), 4.27–3.22 (60H, m, H-5, -6, -3, -2, -4).

^{13}C NMR (125.7 MHz, D_2O) δ (ppm): 102–100 (C-1), 80 (C-4), 75–69 (C-5, C-3, C-2, CH-EPI, CH_2 EPI), 63 (CH_2OH of chain), 62 (C-6), 60 (CH_2).

DLS (size): 3.2 ± 0.8 nm.

ζ potential: 5.1 ±1 mV at pH = 7.4; 19.5 ± 2 mV at pH = 4.

5.34 Synthesis of amino-oligomer oCyDNH$_2$30

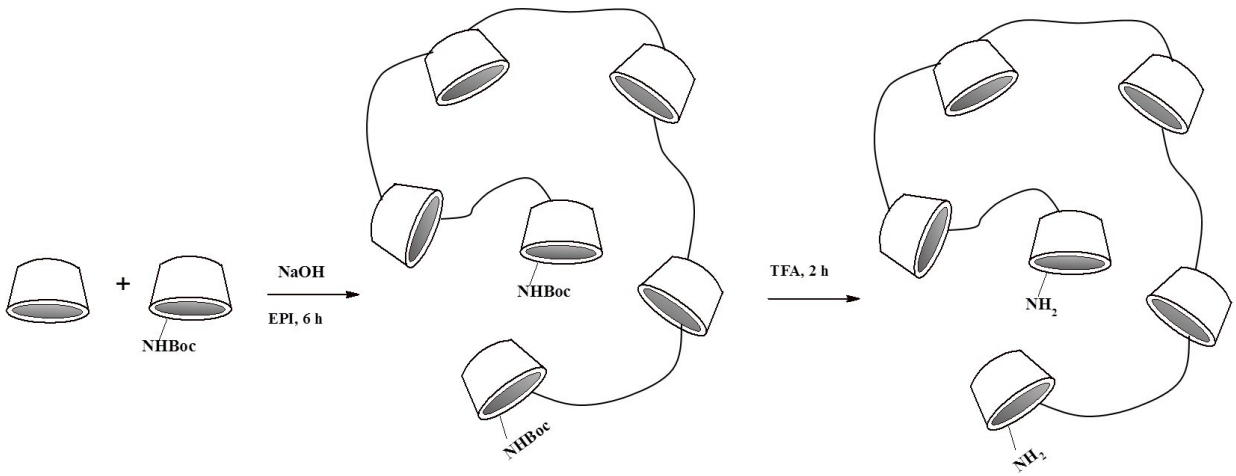

A mixture of 200 mg of β-CD (0.17 mmol.) and 100 mg of CyD3NHBoc (0.081 mmol) in 2 mL of 7 M NaOH solution was stirred overnight at room temperature. EPI (101 µl) was slowly added and the mixture was heated to 40°C. After 6 h, acetone was added and a gel was obtained. The reaction was stopped after 6 h by addition of acetone. After decantation, acetone was removed. The suspension was maintained at 50°C overnight. Then HCl 6 N was added until neutral pH at r.t. and the mixture ultra-filtrated (molecular weight cut-off 5000). The final product was precipitated with ethanol and dried under vacuum obtaining oCyDNH$_2$30 protected with BOC. The polymer was deprotected by treatment with TFA for 2 h and purified by ultrafiltration. Finally, the product was freeze dried to give a white powder.

Yield: 75%.

oCyDNHBoc30:

^{1}H NMR (500 MHz, D_2O) δ (ppm): 5.18-4.82 (7H, m, H-1), 4.25-3.20 (42 H, m, H-5,-6,-3,-2,-4), 1.45 (2.4H, bs, Boc).

^{13}C NMR (125.7 MHz, D_2O) δ (ppm): 102-100 (C-1), 80 (C-4), 75–67 (C-5, C-3, C-2, CH-EPI), 63 (CH_2OH of chains), 62 (C-6), 60 (CH_2 of chains), 28.0 (Boc CH_3).

oCyDNH$_2$30:

^{1}H NMR (500 MHz, D_2O) δ (ppm): 5.20–4.82 (7H, m, H-1), 4.27–3.22 (60H, m, H-5, -6, -3, -2, -4).

^{13}C NMR (125.7 MHz, D_2O) δ (ppm): 102–100 (C-1), 80 (C-4), 75–69 (C-5, C-3, C-2, CH-EPI, CH_2 EPI), 63 (CH_2OH of chain), 62 (C-6), 60 (CH_2).

DLS (size): 3,2 ± 0.8 nm.

ζ potential: -7 ± 1 mV (pH = 7.4), at = 13 ±1 mV (pH 4).

5.35 Synthesis of β-Cyclodextrin oligomer (oCyD)

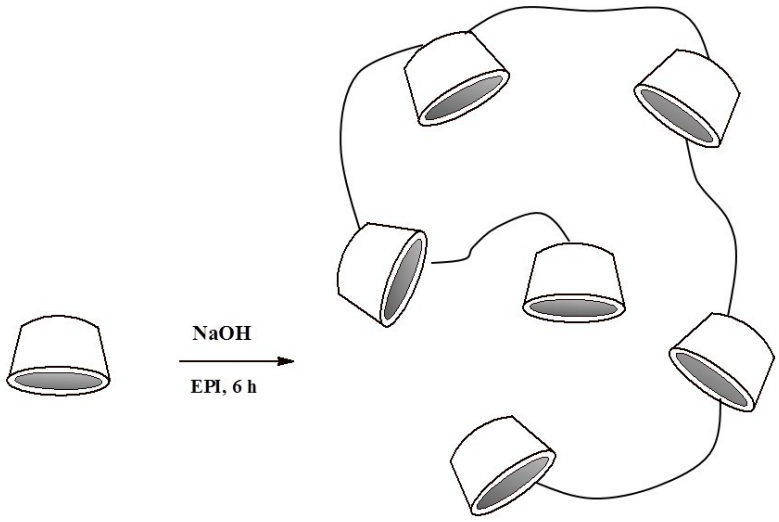

A mixture of 5 g β-CyD (4.4 mmol.) and 10 mL of 7 M NaOH solution was stirred overnight at room temperature. EPI (1.72 mL, 22 mmol) was slowly added under stirred. The reaction was stopped after 6 h by addition of acetone. After decantation, acetone was removed. The suspension was maintained at 50°C overnight. Then HCl 6 N was added until neutral pH at 25°C and the mixture was ultra-filtrated (molecular weight cut-off 5000). Ethanol was added to precipitate the final product. It was filtered and freeze dried to give a white powder.

Yield: 50 %.

^{1}H NMR (500 MHz, D_2O) δ (ppm): 5.20-4.82 (7H, m, H-1), 4.27-3.22 (69 H, m, H-5,-6,-3,-2,-4, H of linker).

^{13}C NMR (125.7 MHz, D_2O) δ (ppm): 102–100 (C-1), 80 (C-4), 75–69 (C-5, C-3, C-2, CH-EPI, CH_2 EPI), 63 (CH_2OH of chain), 62 (C-6), 60 (CH_2).

DLS (size): 3.8 ± 0.7 nm.

ζ potential: 2.1 ± 1 mV.

5.36 Synthesis of pCyD3FA

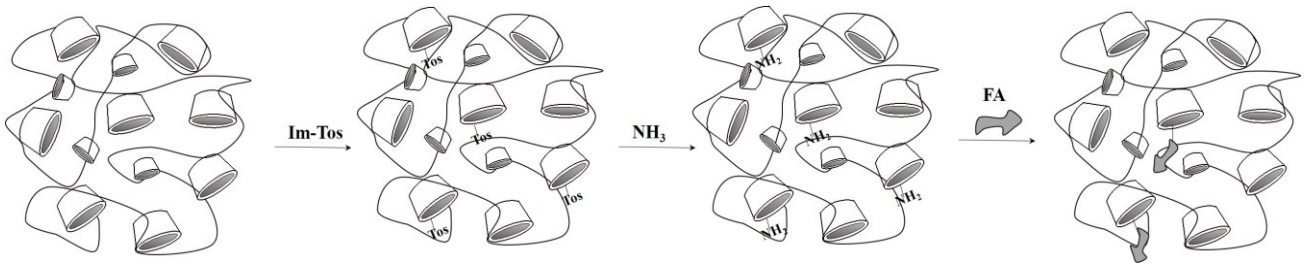

To a solution of commercial polymer (100 mg) and p-toluenesulfonyl imidazole (Is-Im, 22 mg) in 6.0 mL of DMF freshly activated powder molecular sieves 4A (0.50 g) was added, and the mixture was stirred for 48 h. Then, molecular sieves were removed and the mixture was concentrated under reduced pressure. The tosylate, without any purification step, was resuspended in 4 ml of milliQ water in presence of 400 mg of $NaHCO_3$ for 4 h, then 1 ml of 28% NH_3 was added and the reaction was kept under N_2 atmosphere over night. The product obtained was purified by dialysis and the solvent was evaporated to dryness *in vacuo*.

The amino polymers obtained and FA-NHS (50 mg,) were dissolved in dry DMF (2 ml), TEA (10 µl, δ=0.72) was added and the reaction mixture was stirred at room temperature for 48 h. The solvent was then evaporated to dryness *in vacuo*. The product was resuspended in milli-Q water (3 ml) and purified by dialysis.

Yield: 30%.

^{1}H NMR (500 MHz, D_2O) δ (ppm): 8.60 (bs, H-7 of FA), 7.56 (bs, H-13 and H-15 of FA), 6.62 (bs, H-12 and H-16 of FA), 5.20-4.82 (7H, m, H-1), 4.27-3.22 (69 H, m, H-5,-6,-3,-2,-4, EPI and H-FA).

5.37 Synthesis of oCyD3FA

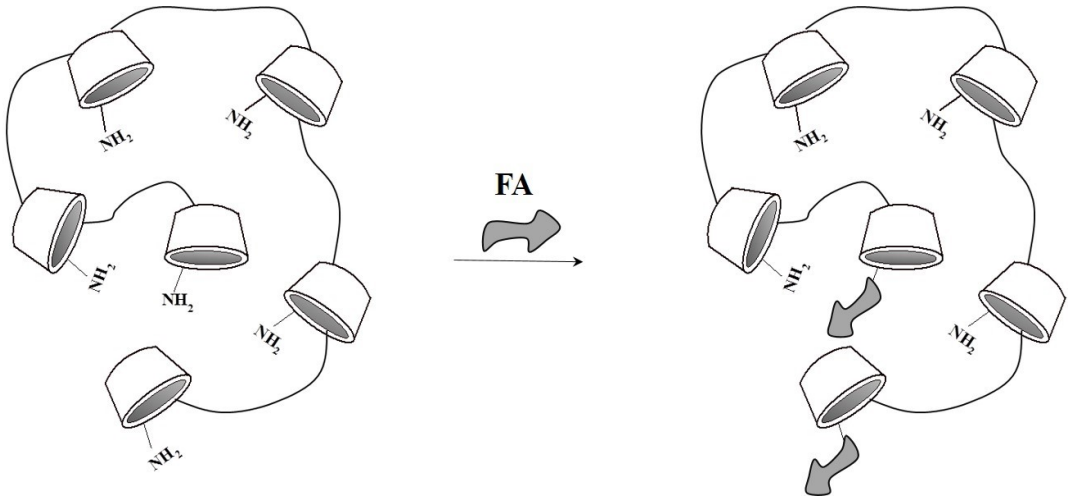

oCyDNH$_2$ previously synthesized (100 mg) and FA-NHS (50 mg) were dissolved in dry DMF (2 ml) , TEA (10 µl, δ=0.72) was added and the reaction mixture was stirred at room temperature for 48 h. The solvent was evaporated to dryness *in vacuo*. The product was resuspended in milli-Q water (3 ml) and purified by dialysis.

Yield: 40%.

^{1}H NMR (500 MHz, D_2O) δ (ppm): 8.60 (bs, H-7 of FA), 7.56 (bs, H-13 and H-15 of FA), 6.62 (bs, H-12 and H-16 of FA), 5.20-4.82 (7H, m, H-1), 4.27-3.22 (69 H, m, H-5,-6,-3,-2,-4, EPI and H-FA).

5.38 Synthesis of Nanodiscs (NDs).

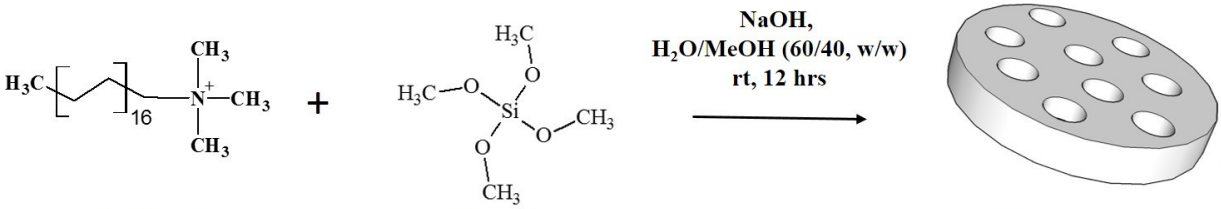

C_{18}TACl **TMOS** **NDs**

Octadecyltrimethylammonium chloride (C_{18}TMACl, 0.42 g) and 1 M NaOH solution (0.3 mL) were dissolved in a water/methanol (60/40; w/w) solution (100 g). tetramethyl orthosilicate (TMOS, 170 µl) was then added to the solution under vigorous stirring (500 rpm) at r.t. and the mixture was further stirred overnight. The white powder was recovered by centrifugation at 4500 rpm and washed with distilled water and ethanol several times, and finally dried. The powder was then calcinated in air at 550 °C for 8 h to remove the remaining organic surfactant. The material was finally thoroughly characterized by means of ζ-potential, XPS, TGA, SAXS, N2 adsorption, SEM and TEM analysis techniques.

5.39 Synthesis of disulfide doped nanodiscs (ss-NDs 10, 30 and 50%)

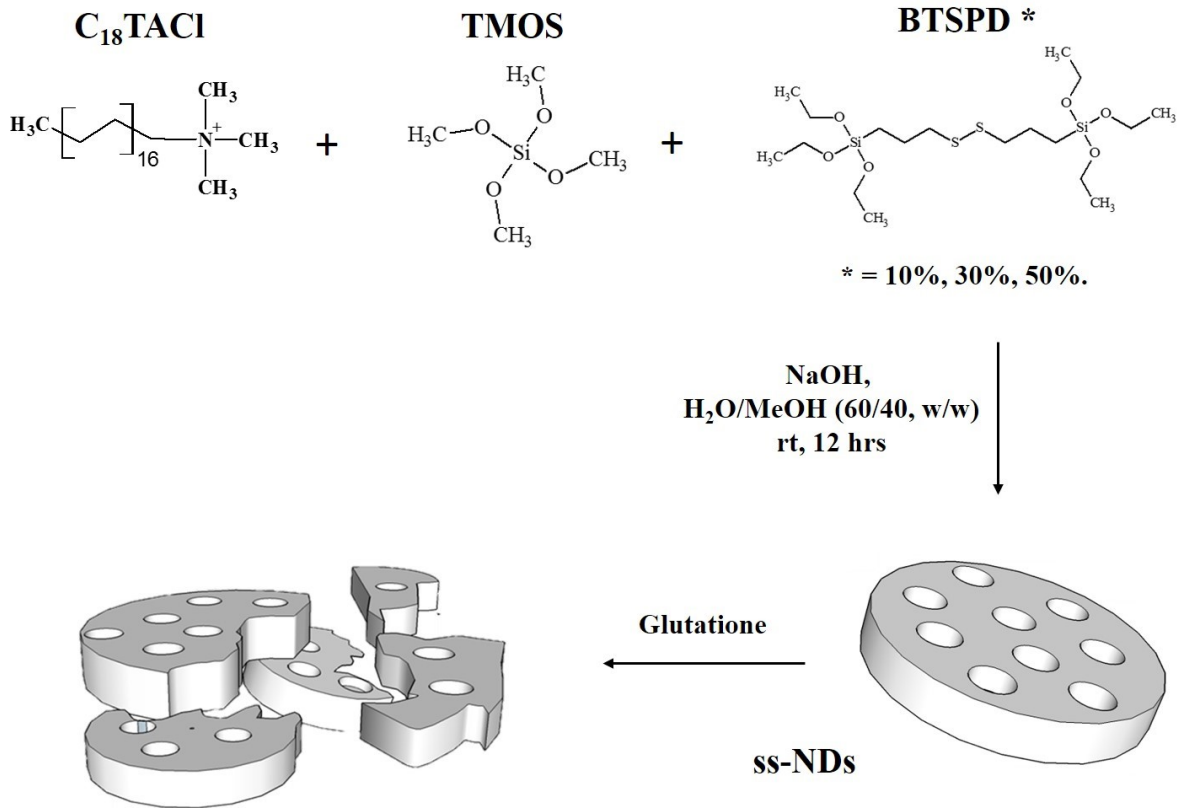

C_{18}TMACl (0.42 g) and 1 M NaOH solution (0.3 mL) were dissolved in a water/methanol (60/40; w/w) solution (100 g) and stirred slowly. A solution of 1 mL methanol containing different molar ratio between TMOS and BTSPD to obtain 10, 30 and 50% disulfide doped NDs (table 7) was then added drop by drop under vigorous stirring, and the mixture left stirred overnight at 500 rpm. After that, the particles were recovered by centrifugation (20 min at 4500 rpm), and purified through a sequence of sonication/centrifugation cycles in EtOH. To remove the surfactants from the pores, the particles were dissolved in acidic EtOH (100 mL, 30 μL of HCl) and refluxed overnight. The particles were hence purified by a sequence of sonication/centrifugation cycles in EtOH and finally dried under vacuum. The material was finally thoroughly characterized by means of ζ-potential, XPS, TGA, SAXS, N_2 adsorption, SEM and TEM analysis techniques.

Table 7: Amount of silica reactant TMOS and BTSPD to synthesize ss-NDs with different percentages of disulfide bridges.

% s-s bridges	TMOS	BTSPD
ssNDs 10%	155 µL	30 µL
ssNDs 30%	120 µL	80 µL
ssNDs 50%	85 µL	135 µL

5.40 Nile Red loading of the NDs (NDs@NR, encapsulation process)

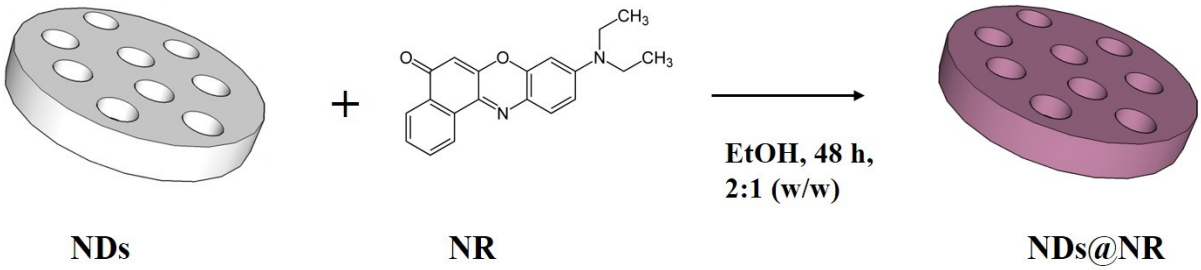

A mixture of NDs (10 mg), Nile Red (20 mg), and ethanol (10 mL) was prepared in a tube, sonicated 10 min, and stirred overnight at r.t. Then, the product was collected by centrifugation (800 rpm for 20 min) and washed several times with ethanol, and then dried under vacuum. The material was characterized by fluorescence spectroscopy and TGA.

5.41 Functionalization of NDs and ss-NDs with fluorescein (FITC-NDs, grafting process)

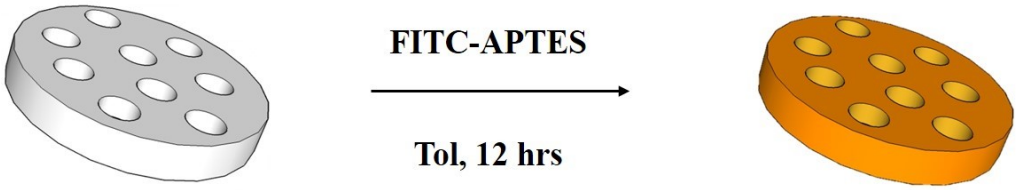

FITC-APTES =

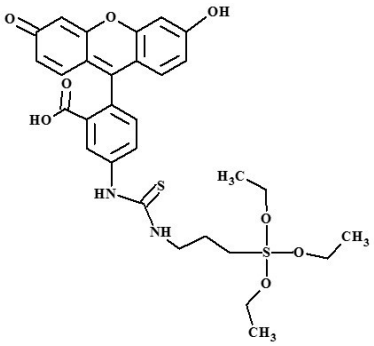

Fluorescein isothiocyanate (3 mg) and 5 µl of APTES were mixed in 1 ml of DMSO and left stirring for 30 min. Subsequently, 200 µl of this solution were added to a suspension of 1 mg of NDs or ss-NDs (10%, 30%, 50%) in 800 µl of toluene beforehand sonicated for 10 min. The mixture was stirred overnight at r.t.. The product was precipitated in diethyl ether and then washed several times with ethanol (using centrifuge at 8000 rpm for 20 min at each washing step).

5.42 Functionalization of NDs and NDs@NR with APTES:

NDs or NDs@NR (4 mg) were suspended in the mixed solvent DMSO/toluene (1:4, total volume 1 mL) by sonication for 15 min. Then APTES (4 µL) was added, and the mixture was stirred overnight at r.t.. The nanoparticles were then collected by centrifugation for 20 min at 14500 rpm. The precipitated solid was then re-dispersed by sonication in toluene and centrifuged three times to remove unreacted silane. The material was characterized by mean of ζ-potential and TGA.

5.43 Preparation of APTES-NDs and APTES-NDs@NR SAMs

Glass plates were introduced into a 100 mL flask and activated with 3:1 H_2SO_4/H_2O_2 (10 mL) at 100 °C for 1 h. The solution was removed and the plates were washed with bi-distilled water (3 × 30 mL) followed by ethanol (3 × 20 mL) and finally dried under nitrogen flow. The plates were then placed into a 100 mL round bottom flask containing toluene (30 mL), 3-Isocyanopropyltriethoxysilane (IC, 0.8 mL) was added and the flask was heated at 115 °C overnight. Subsequently, the plates were removed from the solution and washed with toluene (5 mL) and ethanol (5 mL) and dried with nitrogen flow. The plates were then placed into a suspension of APTES functionalized NDs in toluene (1 mg/mL, 2 mL), and sonicated for 8 minutes, before recovering the plates, rinsing them with toluene (5 mL) and air-drying them before use. The SAM was characterized by mean of SEM and in the case of SAMs@NR with SEM and fluorescent microscopy.

5.44 Functionalization of SAMs with folic acid (FA)

Folic acid (FA, 1 mg, 2.26 μmol) was dissolved in DMSO (1,5 ml) in presence of triethylamine (TEA δ=0.75, 5 μL) and reacted with N-hydroxysuccinimide (NHS, 0.26 mg, 2.26 μmol) and dicyclohexylcarbodiimide (DCC, 0.46 mg, 2.26 μmol) for 1 h at room temperature in the dark. Then APTES functionalized monolayers were placed in this solution and left reacted overnight. Subsequently, the functionalized SAMs were removed from the solution and washed with DMSO, water, ethanol and dried with nitrogen flow.

6 APPENDIX 1: PUBLICATIONS

1. Giglio V., Viale M., Vecchio G., Submitted.
2. Giglio V., Maggini L., De Cola L., Submitted.
3. Giglio V., Viale M., Monticone M., Natile G., Intini F., Vecchio G. Cyclodextrin polymers as carries for the platinum-based anticancer agent LA-12, Submitted.
4. Giglio V., Sgarlata C., Vecchio G. Novel amino-cyclodextrin cross-linked oligomer as efficient carrier for anionic drugs: A spectroscopic and nanocalorimetric investigation, *RSC Advances*, **2015**, 5, 16664-16671.
5. Giglio V., Oliveri V., Viale M., Natile G., Intini F., Vecchio G. Folate-Cyclodextrin conjugates as new carriers of the platinum (IV) complex LA-12, *ChemPlusChem*, **2015**, 80, 536-543.
6. Oliveri V., D'Agata R., Giglio V., Spoto G., Vecchio G. Cyclodextrin-functionalized gold nanoparticles via streptavidin: a supramolecular approach. *Supramolecular Chemistry*, **2013**, 25, 465-473.

7 APPENDIX 2: PROCEEDINGS

1. Giglio V. , Oliveri V., Vecchio G. *"Metal-Chelating Polymer Based on Cyclodextrin and 8-hydroxyquinoline"* 6th Eur. Conference Chemistry in the Life Sciences, Lisbon 10-12/06/2015.
2. Giglio V., Maggini L., Cabrera I., De Cola L. "*Disintegrable Disulfide-doped Silica Nanodiscs: Novel Drug Delivery Materials for Enhanced Performance",* 15th Eur.-Winter School on Physical Organic Chemistry (E-WiSPOC), Bressanone, 1-6/05/2015.
3. Giglio V., Natile G., Intini F., Viale M., Aiello C, Vecchio G "*β-Cyclodextrin polymers functionalized with folic acid as new delivery systems*", 17th Int. Cyclodextrin Symposium, Saarbrucken, 29-31/05/2014.
4. Giglio V., Oliveri V., Natile N., Intini F., Viale M., Aiello C., Vecchio G., "*Coniugati di β-ciclodestrine funzionalizzate con acido folico per l'indirizzamento selettivo di farmaci*", Congresso congiunto delle sezioni SCI Calabria e Sicilia, Catania, 2-3/12/2013.
5. Giglio V., Oliveri V., Natile G., Intini F., Viale M., Aiello C., Vecchio G., "*Folic acid-β-cyclodextin conjugates for drug targeting"*, Biomet 13, XIII Workshop on PharmacoBiometallics, Catania, 25-26/10/2013.
6. Giglio V., Oliveri V., Natile G., Intini F., Viale M., Aiello C., Vecchio G., "*Folate-β-cyclodextrin conjugates as drug targeting systems*", 3rd Eur. Conference on Cyclodextrin, Antalya, 2-4/10/2013.
7. Oliveri V., D'Agata R., Giglio V., Spoto G., Vecchio G. "*β-cyclodextrin-functionalized gold nanoparticles via streptavidin",* Convegno 2012 della Divisione di Chimica dei Sistemi Biologici, 24-25/09/2012, Napoli.

8 ACKNOWLEDGEMENTS

I would like to express my sincere gratitude to my supervisor Prof. Graziella Vecchio for believing in me since the beginning of this stimulating journey into the scientific research and for giving me the opportunity to work with her as PhD student.

I would like to thank also Prof. Luisa De Cola for giving me the opportunity of spending an amazing experience abroad working in her lab, which markedly improved my scientific background.

A special thanks goes to Dr. Laura Maggini for her guidance, support and also for her friendship during my work in Strasbourg, making that period unforgettable.

I would like to thank also Dr. Maurizio Viale of the Department of Integrated Oncological Therapies, IRCCS AOU S. Martino-IST for the biological evaluations of my compounds.

Thank also to Dr. Carmelo Sgarlata for the nano-ITC measurements for the determination of stability constants.

And last, but not least, I want to give thanks to my husband who has encouraged and supported me in all the choices I made; without you I would not have ever become the woman I am now.

9 REFERENCES

1 A. W Jackson Jacksonicki, D. Witzigmann, V. Balasubramanian, J. Huwyler, *J. Control. Release* **2014**, *200*, 138–157.
2 R. Núñez-Lozano, M. Cano, B. Pimentel, G. de la Cueva-Méndez, *Curr. Opin. Biotechnol.* **2015**, *35*, 135–40.
3 R. Duncan, R. Gaspar, *Mol. Pharm.* **2011**, *8*, 2101–2141.
4 M. B. Sporn, *Ann. N. Y. Acad. Sci.* **1997**, *833*, 137–146.
5 E. C. Dreaden, A. M. Alkilany, X. Huang, C. J. Murphy, M. A. El-Sayed, *Chem. Soc. Rev.* **2012**, *41*, 2740–2779.
6 R. Langer, *Science* **2001**, *293*, 58–59.
7 P. R. Lockman, R. J. Mumper, M. A. Khan, D. D. Allen, *Drug Dev. Ind. Pharm.* **2002**, *28*, 1–13.
8 T. Tanaka, P. Decuzzi, M. Cristofanilli, J. H. Sakamoto, E. Tasciotti, F. M. Robertson, M. Ferrari, *Biomed. Microdevices* **2009**, *11*, 49–63.
9 N. P. Truong, M. R. Whittaker, C. W. Mak, T. P. Davis, *Expert Opin. Drug Deliv.* **2015**, *12*, 129–142.
10 J. R. Heath, M. E. Davis, *Annu. Rev. Med.* **2008**, *59*, 251–265.
11 J. Cheng, B. A. Teply, I. Sherifi, J. Sung, G. Luther, F. X. Gu, E. Levy-Nissenbaum, A. F. Radovic-Moreno, R. Langer, O. C. Farokhzad, *Biomaterials* **2007**, *28*, 869–876.
12 V. Reebye, P. Sætrom, P. J. Mintz, K.-W. Huang, P. Swiderski, L. Peng, C. Liu, X. Liu, S. Lindkaer-Jensen, D. Zacharoulis, et al., *Hepatology* **2014**, *59*, 216–227.
13 H.-C. Huang, S. Barua, G. Sharma, S. K. Dey, K. Rege, *J. Control. Release* **2011**, *155*, 344–357.
14 R. W. Ross, A. L. Zietman, W. Xie, J. J. Coen, D. M. Dahl, W. U. Shipley, D. S. Kaufman, T. Islam, A. R. Guimaraes, R. Weissleder, et al., *Clin. Imaging* **2009**, *33*, 301–305.
15 P. Rivera Gil, D. Hühn, L. L. del Mercato, D. Sasse, W. J. Parak, *Pharmacol. Res.* **2010**, *62*, 115–125.
16 N. Desai, V. Trieu, Z. Yao, L. Louie, S. Ci, A. Yang, C. Tao, T. De, B. Beals, D. Dykes, et al., *Clin. Cancer Res.* **2006**, *12*, 1317–1324.
17 F. M. Muggia, J. D. Hainsworth, S. Jeffers, P. Miller, S. Groshen, M. Tan, L. Roman, B. Uziely, L. Muderspach, A. Garcia, et al., *J. Clin. Oncol.* **1997**, *15*, 987–993.
18 G. Batist, G. Ramakrishnan, C. S. Rao, A. Chandrasekharan, J. Gutheil, T. Guthrie, P. Shah, A. Khojasteh, M. K. Nair, K. Hoelzer, et al., *J. Clin. Oncol.* **2001**, *19*, 1444–1454.
19 J. Homsi, G. R. Simon, C. R. Garrett, G. Springett, R. De Conti, A. A. Chiappori, P. N. Munster, M. K. Burton, S. Stromatt, C. Allievi, et al., *Clin. Cancer Res.* **2007**, *13*, 5855–5861.
20 A. Awada, A. A. Garcia, S. Chan, G. H. M. Jerusalem, R. E. Coleman, M. T. Huizing, A. Mehdi, S. M. O'Reilly, J. T. Hamm, P. J. Barrett-Lee, et al., *Lancet. Oncol.* **2013**, *14*, 1216–1225.
21 G. P. Stathopoulos, D. Antoniou, J. Dimitroulis, J. Stathopoulos, K. Marosis, P. Michalopoulou, *Cancer Chemother. Pharmacol.* **2011**, *68*, 945–950.
22 R. T. Poon, N. Borys, *Future Oncol.* **2011**, *7*, 937–945.
23 M. E. Davis, J. E. Zuckerman, C. H. J. Choi, D. Seligson, A. Tolcher, C. A. Alabi, Y. Yen, J. D. Heidel, A. Ribas, *Nature* **2010**, *464*, 1067–1070.
24 S. Gaur, Y. Wang, L. Kretzner, L. Chen, T. Yen, X. Wu, Y.-C. Yuan, M. Davis, Y. Yen, *Nanomedicine* **2014**, *10*, 1477–1486.
25 H. D. Williams, N. L. Trevaskis, S. A. Charman, R. M. Shanker, W. N. Charman, C. W. Pouton, C. J. H. Porter, *Pharmacol. Rev.* **2013**, *65*, 315–499.
26 S. Karve, M. E. Werner, R. Sukumar, N. D. Cummings, J. A. Copp, E. C. Wang, C. Li, M. Sethi, R. C. Chen, M. E. Pacold, et al., *Proc. Natl. Acad. Sci. U. S. A.* **2012**, *109*, 8230–8235.
27 V. Bonnet, C. Gervaise, F. Djedaïni-Pilard, A. Furlan, C. Sarazin, *Drug Discov. Today* **2015**, *20*, 1120–6.
28 H. Arima, Y. Hayashi, T. Higashi, K. Motoyama, *Expert Opin. Drug Deliv.* **2015**, *12*, 1425–1441.
29 R. Gref, M. Lück, P. Quellec, M. Marchand, E. Dellacherie, S. Harnisch, T. Blunk, R. Müller, *Colloids Surf. B. Biointerfaces* **2000**, *18*, 301–313.
30 H. Otsuka, Y. Nagasaki, K. Kataoka, *Adv. Drug Deliv. Rev.* **2003**, *55*, 403–419.
31 A. Wicki, D. Witzigmann, V. Balasubramanian, J. Huwyler, *J. Control. Release* **2014**, *200*, 138–157.
32 A. I. Minchinton, I. F. Tannock, *Nat. Rev. Cancer* **2006**, *6*, 583–592.
33 X.-Q. Zhang, X. Xu, N. Bertrand, E. Pridgen, A. Swami, O. C. Farokhzad, *Adv. Drug Deliv. Rev.* **2012**, *64*, 1363–1384.
34 T. Lammers, F. Kiessling, W. E. Hennink, G. Storm, *J. Control. Release* **2012**, *161*, 175–187.
35 M. N. Holme, I. A. Fedotenko, D. Abegg, J. Althaus, L. Babel, F. Favarger, R. Reiter, R. Tanasescu, P.-L. Zaffalon, A. Ziegler, et al., *Nat. Nanotechnol.* **2012**, *7*, 536–543.
36 A. Jhaveri, P. Deshpande, V. Torchilin, *J. Control. Release* **2014**, *190*, 352–370.
37 I. F. Tannock, D. Rotin, *Cancer Res.* **1989**, *49*, 4373–4384.

38 Y. Obata, S. Tajima, S. Takeoka, *J. Control. Release* **2010**, *142*, 267–276.
39 S. M. Moghimi, A. C. Hunter, J. C. Murray, *Pharmacol. Rev.* **2001**, *53*, 283–318.
40 F. Yuan, M. Dellian, D. Fukumura, M. Leunig, D. A. Berk, V. P. Torchilin, R. K. Jain, *Cancer Res.* **1995**, *55*, 3752–3756.
41 S. M. Moghimi, J. Szebeni, *Prog. Lipid Res.* **2003**, *42*, 463–478.
42 Y. Matsumura, H. Maeda, *Cancer Res.* **1986**, *46*, 6387–6392.
43 H. F. Dvorak, J. A. Nagy, J. T. Dvorak, A. M. Dvorak, *Am. J. Pathol.* **1988**, *133*, 95–109.
44 H. Maeda, *Adv. Drug Deliv. Rev.* **2015**, *91*, 3–6.
45 S. A. Skinner, P. J. Tutton, P. E. O'Brien, *Cancer Res.* **1990**, *50*, 2411–2417.
46 V. Torchilin, *Adv. Drug Deliv. Rev.* **2011**, *63*, 131–135.
47 H. Hashizume, P. Baluk, S. Morikawa, J. W. McLean, G. Thurston, S. Roberge, R. K. Jain, D. M. McDonald, *Am. J. Pathol.* **2000**, *156*, 1363–1380.
48 B. Haley, E. Frenkel, *Urol. Oncol. 26*, 57–64.
49 L. E. Gerweck, K. Seetharaman, *Cancer Res.* **1996**, *56*, 1194–1198.
50 Y. Wang, A. Santos, A. Evdokiou, D. Losic, *J. Mater. Chem. B* **2015**, *3*, 7153–7172.
51 Y. Yan, G. K. Such, A. P. R. Johnston, J. P. Best, F. Caruso, *ACS Nano* **2012**, *6*, 3663–3669.
52 R. K. Jain, T. Stylianopoulos, *Nat. Rev. Clin. Oncol.* **2010**, *7*, 653–664.
53 K. Strebhardt, A. Ullrich, *Nat. Rev. Cancer* **2008**, *8*, 473–480.
54 R. Misra, S. Acharya, S. K. Sahoo, *Drug Discov. Today* **2010**, *15*, 842–850.
55 W. Liang, J. K. W. Lam, *Molecular Regulation of Endocytosis*, InTech, **2012**.
56 A. P. Chapman, P. Antoniw, M. Spitali, S. West, S. Stephens, D. J. King, *Nat. Biotechnol.* **1999**, *17*, 780–783.
57 W. P. Faulk, C. G. Taylor, C. J. Yeh, J. A. McIntyre, *Mol. Biother.* **1990**, *2*, 57–60.
58 J. F. Head, F. Wang, R. L. Elliott, *Adv. Enzyme Regul.* **1997**, *37*, 147–169.
59 N. G. Rainov, A. Söling, *Curr. Opin. Mol. Ther.* **2005**, *7*, 483–492.
60 T. Minko, *Adv. Drug Deliv. Rev.* **2004**, *56*, 491–509.
61 G. Lurje, H.-J. Lenz, *Oncology* **2009**, *77*, 400–410.
62 V. Grünwald, M. Hidalgo, *J. Natl. Cancer Inst.* **2003**, *95*, 851–867.
63 J. Mendelsohn, *J. Clin. Oncol.* **2003**, *21*, 2787–2799.
64 R. J. Lee, P. S. Low, *Biochim. Biophys. Acta - Biomembr.* **1995**, *1233*, 134–144.
65 X. Q. Pan, X. Zheng, G. Shi, H. Wang, M. Ratnam, R. J. Lee, *Blood* **2002**, *100*, 594–602.
66 J. Sudimack, R. J. Lee, *Adv. Drug Deliv. Rev.* **2000**, *41*, 147–162.
67 X. Zhao, *Adv. Drug Deliv. Rev.* **2004**, *56*, 1193–1204.
68 P. S. Low, W. A. Henne, D. D. Doorneweerd, *Acc. Chem. Res.* **2008**, *41*, 120–129.
69 X. Zhao, H. Li, R. J. Lee, *Expert Opin. Drug Deliv.* **2008**, *5*, 309–319.
70 S. D. Weitman, R. H. Lark, L. R. Coney, D. W. Fort, V. Frasca, V. R. Zurawski, B. A. Kamen, *Cancer Res.* **1992**, *52*, 3396–3401.
71 J. F. Ross, H. Wang, F. G. Behm, P. Mathew, M. Wu, R. Booth, M. Ratnam, *Cancer* **1999**, *85*, 348–357.
72 N. Nakashima-Matsushita, T. Homma, S. Yu, T. Matsuda, N. Sunahara, T. Nakamura, M. Tsukano, M. Ratnam, T. Matsuyama, *Arthritis Rheum.* **1999**, *42*, 1609–1616.
73 F. Shen, J. F. Ross, X. Wang, M. Ratnam, *Biochemistry* **1994**, *33*, 1209–1215.
74 C. Paulos, *Adv. Drug Deliv. Rev.* **2004**, *56*, 1205–1217.
75 S. Wang, R. J. Lee, C. J. Mathias, M. A. Green, P. S. Low, *Bioconjug. Chem.* **1996**, *7*, 56–62.
76 O. Aronov, A. T. Horowitz, A. Gabizon, D. Gibson, *Bioconjug. Chem.* **2003**, *14*, 563–574.
77 I. J. Majoros, A. Myc, T. Thomas, C. B. Mehta, J. R. Baker, *Biomacromolecules* **2006**, *7*, 572–579.
78 C. A. Ladino, R. V Chari, L. A. Bourret, N. L. Kedersha, V. S. Goldmacher, *Int. J. Cancer* **1997**, *73*, 859–864.
79 K. Motoyama, R. Onodera, A. Okamatsu, T. Higashi, R. Kariya, S. Okada, H. Arima, *J. Drug Target.* **2013**, *22*, 211–219
80 J.-J. Yin, S. Sharma, S. P. Shumyak, Z.-X. Wang, Z.-W. Zhou, Y. Zhang, P. Guo, C.-Z. Li, J. R. Kanwar, T. Yang, et al., *PLoS One* **2013**, *8*, e62289.
81 R. R. Hood, C. Shao, D. M. Omiatek, W. N. Vreeland, D. L. DeVoe, *Pharm. Res.* **2013**, *30*, 1597–1607.
82 J. Kim, D. R. Wilson, C. G. Zamboni, J. J. Green, *J. Drug Target.* **2015**, *23*, 627–641.
83 X. Ma, A. Gong, B. Chen, J. Zheng, T. Chen, Z. Shen, A. Wu, *Colloids Surf. B. Biointerfaces* **2015**, *126*, 44–49.
84 B. Bahrami, M. Mohammadnia-Afrouzi, P. Bakhshaei, Y. Yazdani, G. Ghalamfarsa, M. Yousefi, S. Sadreddini, F. Jadidi-Niaragh, M. Hojjat-Farsangi, *Tumour Biol.* **2015**, 5727–5742.
85 J. Fan, G. Fang, X. Wang, F. Zeng, Y. Xiang, S. Wu, *Nanotechnology* **2011**, *22*, 455102–455113.
86 S. Mohapatra, S. R. Rout, R. Narayan, T. K. Maiti, *Dalton Trans.* **2014**, *43*, 15841–15850.

87 Z. Luo, X. Ding, Y. Hu, S. Wu, Y. Xiang, Y. Zeng, B. Zhang, H. Yan, H. Zhang, L. Zhu, et al., *ACS Nano* **2013**, *7*, 10271–10284.
88 M. Liong, J. Lu, M. Kovochich, T. Xia, S. G. Ruehm, A. E. Nel, F. Tamanoi, J. I. Zink, *ACS Nano* **2008**, *2*, 889–896.
89 H. Shmeeda, *Mol. Cancer Ther.* **2006**, *5*, 818–824.
90 J. Wu, Q. Liu, R. J. Lee, *Int. J. Pharm.* **2006**, *316*, 148–153.
91 V. Torchilin, *Eur. J. Pharm. Biopharm.* **2009**, *71*, 431–444.
92 M. Xu, J. Qian, X. Liu, T. Liu, H. Wang, *Mater. Sci. Eng. C. Mater. Biol. Appl.* **2015**, *50*, 341–347.
93 E. Fleige, M. A. Quadir, R. Haag, *Adv. Drug Deliv. Rev.* **2012**, *64*, 866–884.
94 Y.-C. Wang, F. Wang, T.-M. Sun, J. Wang, *Bioconjug. Chem.* **2011**, *22*, 1939–1945.
95 W. Chen, Y. Shi, H. Feng, M. Du, J. Z. Zhang, J. Hu, D. Yang *J. Phys. Chem. B* **2012**, *116*, 9231–9237.
96 A. W. Jackson, D. A. Fulton *Macromolecules*, **2012**, *45*, 2699–2708.
97 L.-Y. Tang, Y.-C. Wang, Y. Li, J.-Z. Du, J. Wang *Bioconjugate Chem.* **2009**, *20*, 1095–1099.
98 H.-Y. Wen, H.-Q. Dong, W.-J. Xie, Y.-Y. Li, K. Wang, G. M. Pauletti, D.-L. Shi *Chem. Commun*. **2011**, *47*, 3550-3552.
99 S. Quignard, S. Masse, G. Laurent, T. Coradin *Chem. Commun.* **2013**, *49*, 3410-3412.
100 Z. Xu, K. Zhang, X. Liu, H. Zhang *RSC Adv.* **2013**, *3*, 17700-17702.
101 J. Croissant, X. Cattoen, M. W. C. Man, A. Gallud, L. Raehm, P. Trens, M. Maynadier, J.-O. Durand *Adv. Mater.* **2014**, *26*, 6174–6180.
102 Y. Chen, Q. Meng, M. Wu, S. Wang, P. Xu, H. Chen, Y. Li, L. Zhang, L. Wang, J. Shi *J. Am. Chem. Soc.* **2014**, *136*, 16326–16334.
103 M. W. Dewhirst, Z. Vujaskovic, E. Jones, D. Thrall, *Int. J. Hyperthermia* **2005**, *21*, 779–790.
104 V. P. Torchilin, *Nat. Rev. Drug Discov.* **2014**, *13*, 813–27.
105 D. Needham, G. Anyarambhatla, G. Kong, M. W. Dewhirst, *Cancer Res.* **2000**, *60*, 1197–1201.
106 B. M. Dicheva, G. A. Koning, *Expert Opin. Drug Deliv.* **2014**, *11*, 83–100.
107 S. V Kurkov, T. Loftsson, *Int. J. Pharm.* **2013**, *453*, 167–180.
108 L. Escuder-Gilabert, Y. Martín-Biosca, M. J. Medina-Hernández, S. Sagrado, *J. Chromatogr. A* **2014**, *1357*, 2–23.
109 I. Tabushi, Y. Kuroda, T. Mizutani, *Tetrahedron* **1984**, *40*, 545–552.
110 R. Breslow, *Adv. Enzymol. Relat. Areas. Mol. Biol.* **1986**, *58*, 1–60.
111 W. Tagaki, H. Yamamoto, *Tetrahedron Lett.* **1991,** *32*, 1207–1207.
112 I. Tabushi, Y. Kuroda, T. Mizutani, *J. Am. Chem. Soc.* **1986**, *108*, 4514 –4557.
113 G. Galaverna, R. Corradini, A. Dossena, R. Marchelli, G. Vecchio, *Electrophoresis* **1997**, *18*, 905–911.
114 K. Kano, *J. Phys. Org. Chem.* **1997**, *10*, 286–291.
115 A. M. Amorini, F. Bellia, V. Di Pietro, B. Giardina, D. La Mendola, G. Lazzarino, S. Sortino, B. Tavazzi, E. Rizzarelli, G. Vecchio, *Eur. J. Med. Chem.* **2007**, *42*, 910–920.
116 Y. Liu, B. Li, B.-H. Han, Y.-M. Li, R.-T. Chen, *J. Chem. Soc. Perkin Trans. 2* **1997**, 1275–1278.
117 Y. Liu, Y.-M. Zhang, A.-D. Qi, R.-T. Chen, K. Yamamoto, T. Wada, Y. Inoue, *J. Org. Chem.* **1997**, *62*, 1826–1830.
118 R. Breslow, L. E. Overman, *J. Am. Chem. Soc.* **1970**, *92*, 1075–1077.
119 M. Rezac, R. Breslow, *Tetrahedron Lett.* **1997**, *38*, 5763–5766.
120 R. P. Bonomo, V. Cucinotta, F. D'Alessandro, G. Impellizzeri, G. Maccarrone, G. Vecchio, E. Rizzarelli, *Inorg. Chem.* **1991**, *30*, 2708–2713.
121 R. K. Jones, J. E. Caldwell, S. J. Brull, R. G. Soto, *Anesthesiology* **2008**, *109*, 816–824.
122 A. I. Rosenbaum, G. Zhang, J. D. Warren, F. R. Maxfield, *Proc. Natl. Acad. Sci.* **2010**, *107*, 5477–5482.
123 Y. Shi, J. Goodisman, J. C. Dabrowiak, *Inorg. Chem.* **2013**, *52*, 9418–9426.
124 N. Li, Y. Chen, Y.-M. Zhang, Y. Yang, Y. Su, J.-T. Chen, Y. Liu, *Sci. Rep.* **2014**, *4*, 4164–4170.
125 S. Salmaso, S. Bersani, A. Semenzato, P. Caliceti, *J. Drug Target.* **2007**, *15*, 379–390.
126 H. Zhang, Z. Cai, Y. Sun, F. Yu, Y. Chen, B. Sun, *J. Biomed. Mater. Res. A* **2012**, *100*, 2441–9.
127 A. Okamatsu, K. Motoyama, R. Onodera, T. Higashi, T. Koshigoe, Y. Shimada, K. Hattori, T. Takeuchi, H. Arima, *Bioconjug. Chem.* **2013**, *24*, 724–733.
128 A. Okamatsu, K. Motoyama, R. Onodera, T. Higashi, T. Koshigoe, Y. Shimada, K. Hattori, T. Takeuchi, H. Arima, *Biomacromolecules* **2013**, *14*, 4420–8.
129 L. Qian, Y. Guan, H. Xiao, *Int. J. Pharm.* **2008**, *357*, 244–251.
130 J. Szejtli, *Chem. Rev.* **1998**, *98*, 1743–1754.
131 R. Deveswaran, H. P. S. K, S. Bharath, B. V Basavaraj, V. Madhavan, *J. Chem. Biol. Phys. Sci*. **2012**, *2*, 325–330.
132 J. Zhang, P. X. Ma, *Adv. Drug Deliv. Rev*. **2013**, *65*, 1215–1233.

133 R. Gref, D. Duchêne, *J. Drug Deliv. Sci. Technol.* **2012**, *22*, 223–233.
134 E. Renard, A. Deratani, G. Volet, B. Sebille, *Eur. Polym. J.* **1997**, *33*, 49–57.
135 R. Anand, M. Malanga, I. Manet, F. Manoli, K. Tuza, A. Aykaç, C. Ladavière, E. Fenyvesi, A. Vargas-Berenguel, R. Gref, et al., *Photochem. Photobiol. Sci.* **2013**, *12*, 1841–1854.
136 P. Mura, M. . Faucci, F. Maestrelli, S. Furlanetto, S. Pinzauti, *J. Pharm. Biomed. Anal.* **2002**, *29*, 1015–1024.
137 S. Nie, S. Zhang, W. Pan, Y. Liu, *Drug Dev. Ind. Pharm.* **2011**, *37*, 606–612.
138 C. Liu, W. Zhang, H. Yang, W. Sun, X. Gong, J. Zhao, Y. Sun, G. Diao, *PLoS One* **2014**, *9*, e101761.
139 M. Cirri, M. Bragagni, N. Mennini, P. Mura, *Eur. J. Pharm. Biopharm.* **2012**, *80*, 46–53.
140 N. Zhang, J. Li, W. Jiang, C. Ren, J. Li, J. Xin, K. Li, *Int. J. Pharm.* **2010**, *393*, 212–218.
141 J. R. Kanwar, B. M. Long, R. K. Kanwar, *Curr. Med. Chem.* **2011**, *18*, 2079–2085.
142 S. Y. Yang, R. Hoonor, H.-S. Jin, J. Kim, *Bull. Korean Chem. Soc.* **2013**, *34*, 2016–2022.
143 J. Li, H. Xiao, J. Li, Y. Zhong, *Int. J. Pharm.* **2004**, *278*, 329–342.
144 J. Cheng, K.T. Khin, M.E. Davis, *Mol. Pharmaceutics*, **2004**, 1, 183−193.
145 J. Cheng, K.T. Khin, G.S. Jensen, A. Liu, M. E. Davis, *Bioconjugate Chem.* **2003**, 14, 1007−1017.
146 M. E. Davis, *Adv. Drug Delivery Rev.* **2009**, 61, 1189−1192.
147 M. E. Davis, *Mol. Pharm.* **2009**, *6*, 659–668.
148 C. Kim, B. P. Shah, P. Subramaniam, K.B. Lee, *Mol. Pharmaceutics* **2011**, 8, 1955−1961.
149 I. Puskás, A. Szemjonov, É. Fenyvesi, M. Malanga, L. Szente, *Carbohydr. Polym.* **2013**, *94*, 124–128.
150 M. E. Fox, F. C. Szoka, J. M. J. Fréchet, *Acc. Chem. Res.* **2009**, *42*, 1141–1151.
151 F. Tang, L. Li, D. Chen, *Adv. Mater.* **2012**, *24*, 1504–1534.
152 A. T. Dickschat, F. Behrends, M. Bühner, J. Ren, M. Weiss, H. Eckert, A. Studer, *Chemistry* **2012**, *18*, 16689–16697.
153 Y. Zhang, J. Wang, X. Bai, T. Jiang, Q. Zhang, S. Wang, *Mol. Pharm.* **2012**, *9*, 505–513.
154 I. I. Slowing, B. G. Trewyn, S. Giri, V. S. Y. Lin, *Adv. Funct. Mater.* **2007**, 17, 1225–1236.
155 A. Popat, S. B. Hartono, F. Stahr, J. Liu, S. Z. Qiao, G. Q. Lu, *Nanoscale* **2011**, 3, 2801–2818.
156 Z. Li, J. C. Barnes, A. Bosoy, J. F. Stoddart, J. I. Zink, *Chem. Soc. Rev.* **2012**, 41, 2590–2605.
157 J. L. Vivero-Escoto, I. I. Slowing, B. G. Trewyn, V. S. Lin, *Small* **2010**, 6, 1952–1967.
158 P. Yang, S. Gai, J. Lin, *Chem. Soc. Rev.* **2012**, 41, 3679–3698.
159 L. Tang, N. P. Gabrielson, F. M. Uckun, T. M. Fan, J. Cheng, *Mol. Pharm.* **2013**, *10*, 883–892.
160 C. T. Kresge, M. E. Leonowicz, W. J. Roth, J. C. Vartuli, J. S. Beck, *Nature* **1992**, *359*, 710–712.
161 S. Inagaki, Y. Fukushima, K. Kuroda, *J. Chem. Soc. Chem. Commun.* **1993**, 680–382.
162 C.-Y. Lai, B. G. Trewyn, D. M. Jeftinija, K. Jeftinija, S. Xu, S. Jeftinija, V. S.-Y. Lin, *J. Am. Chem. Soc.* **2003**, *125*, 4451–4459.
163 M. Vallet-Regi, A. Rámila, R. P. del Real, J. Pérez-Pariente, *Chem. Mater.* **2001**, *13*, 308–311.
164 M. Vallet-Regí, F. Balas, D. Arcos, *Angew. Chem. Int. Ed. Engl.* **2007**, *46*, 7548–7558.
165 B. G. Trewyn, S. Giri, I. I. Slowing, V. S.-Y. Lin, *Chem. Commun. (Camb).* **2007**, 3236–3245.
166 S.-H. Wu, C.-Y. Mou, H.-P. Lin, *Chem. Soc. Rev.* **2013**, *42*, 3862–3875.
167 A. B. D. Nandiyanto, S.-G. Kim, F. Iskandar, K. Okuyama, *Microporous Mesoporous Mater.* **2009**, *120*, 447–453.
168 J. S. Beck, J. C. Vartuli, W. J. Roth, M. E. Leonowicz, C. T. Kresge, K. D. Schmitt, C. T. W. Chu, D. H. Olson, E. W. Sheppard, *J. Am. Chem. Soc.* **1992**, *114*, 10834–10843.
169 M. Widenmeyer, R. Anwander, *Chem. Mater.* **2002**, *14*, 1827–1831.
170 L. Wang, W. Zhao, W. Tan, *Nano Res.* **2008**, *1*, 99–115.
171 D. Brühwiler, *Nanoscale* **2010**, *2*, 887–892.
172 J. Kecht, A. Schlossbauer, T. Bein, *Chem. Mater.* **2008**, *20*, 7207–7214.
173 M. Mizutani, Y. Yamada, T. Nakamura, K. Yano, *Chem. Mater.* **2008**, *20*, 4777–4782.
174 J. L. Vivero-Escoto, I. I. Slowing, C.-W. Wu, V. S.-Y. Lin, *J. Am. Chem. Soc.* **2009**, *131*, 3462–3463.
175 R. Casasús, E. Climent, M. D. Marcos, R. Martínez-Mañez, F. Sancenón, J. Soto, P. Amorós, J. Cano, E. Ruiz, *J. Am. Chem. Soc.* **2008**, *130*, 1903–1917.
176 H. Kim, S. Kim, C. Park, H. Lee, H. J. Park, C. Kim, *Adv. Mater.* **2010**, *22*, 4280–4283.
177 D. R. Radu, C.-Y. Lai, K. Jeftinija, E. W. Rowe, S. Jeftinija, V. S.-Y. Lin, *J. Am. Chem. Soc.* **2004**, *126*, 13216–13217.
178 I. Slowing, B. G. Trewyn, V. S.-Y. Lin, *J. Am. Chem. Soc.* **2006**, *128*, 14792–147923.
179 M. Longmire, P. L. Choyke, H. Kobayashi, *Nanomedicine (Lond)* **2008**, *3*, 703–717.
180 X. Huang, L. Li, T. Liu, N. Hao, H. Liu, D. Chen, F. Tang, *ACS Nano* **2011**, *5*, 5390–5399.
181 R. Agarwal, V. Singh , P. Jurney, L. Shi, S. V. Sreenivasan, K. Roy *PNAS* **2013**, *110*, 17247–17252.
182 K. S. Finnie, D. J. Waller, F. L. Perret, A. M. Krause-Heuer, H. Q. Lin, J. V. Hanna, C. J. Barbe *J Sol-Gel Sci Technol* **2009**, *49*, 12–18.

183 J.-H. Park, L. Gu, G. Von Maltzahn, E. Ruoslahti, S. N. Bhatia, M. J. Sailor *Nature Mater.* **2009**, *8*, 331–336.
184 N. K. Hon, Z. Shaposhnik, E. D. Diebold, F. Tamanoi, B. Jalali *J. Biomed. Mater. Res. Part A* **2012**, *100*, 3416–3421.
185 K. K. Pohaku Mitchell, A. Liberman, A. C. Kummel, W. C. Trogler *J. Am. Chem. Soc.* **2012**, *134*, 13997–14003.
186 T. Fontecave, C. Sanchez, T. Azaïs, C. Boissière, *Chem. Mater.* **2012**, *24*, 4326–4336.
187 W. Gao, J. M. Chan, O. C. Farokhzad *Mol. Pharmaceutics* **2010**, *7*, 1913–1920.
188 L. E. Strong, J. L. West *Nanomedicine and Nanobiotechnology* **2011**, *3*, 307–317.
189 S. Ganta, H. Devalapally, A. Shahiwala, M. Amiji *J. Control. Release* **2008**, *126*, 187–204.
190 R. V. Ulijn, *J. Mater. Chem.* **2006**, *16*, 2217–2225.
191 R. Cheng, F. Feng, F. Meng, C. Deng, J. Feijen, Z. Zhong *J. Control. Release* **2011**, *152*, 2–12.
192 G. Saito, J. A. Swanson, K.-D. Lee *Adv. Drug Deliv. Rev.* **2003**, *55*, 199–215.
193 P. Caliceti, S. Salmaso, A. Semenzato, T. Carofiglio, R. Fornasier, M. Fermeglia, M. Ferrone, S. Pricl, *Bioconjug. Chem.* **2003**, *14*, 899–908.
194 V. Oliveri, A. Puglisi, M. Viale, C. Aiello, C. Sgarlata, G. Vecchio, J. Clarke, J. Milton, J. Spencer, *Chemistry* **2013**, *19*, 13946–13955.
195 A. Puglisi, R. Purrello, E. Rizzarelli, S. Sortino, G. Vecchio, *New J. Chem.* **2007**, *31*, 1499–1506.
196 M. Ceborska, M. Zimnicka, M. Pietrzak, A. Troć, M. Koźbiał, J. Lipkowski, *Org. Biomol. Chem.* **2012**, *10*, 5186–5188.
197 V. Cucinotta, A. Giuffrida, D. La Mendola, G. Maccarrone, A. Puglisi, E. Rizzarelli, G. Vecchio *J. Chromatogr. B* **2004**, *800*, 127–133.
198 H. F. M. Nelissen, F. Venema, R. M. Uittenbogaard, M. C. Feiters, R. J. M. Nolte, *J. Chem. Soc. Perkin Trans. 2* **1997**, 2045–2053.
199 A. Clementi, M. C. Aversa, C. Corsaro, J. Spooren, R. Stancanelli, C. O'Connor, M. McNamara, A. Mazzaglia, *J. Incl. Phenom. Macrocycl. Chem.* **2010**, *69*, 321–325.
200 B. Balan, D. L. Sivadas, K. R. Gopidas, *Org. Lett.* **2007**, *9*, 2709–2712.
201 J. Kaspárková, O. Nováková, O. Vrána, F. Intini, G. Natile, V. Brabec, *Mol. Pharmacol.* **2006**, *70*, 1708–1719.
202 J. Turánek, A. Kasná, D. Záluská, J. Neca, V. Kvardová, P. Knötigová, V. Horváth, L. SIndlerová, A. Kozubík, P. Sova, et al., *Anticancer. Drugs* **2004**, *15*, 537–543.
203 P. Sova, A. Mistr, A. Kroutil, F. Zak, P. Pouckova, M. Zadinova, *Anticancer. Drugs* **2006**, *17*, 201–206.
204 L. Wanka, K. Iqbal, P. R. Schreiner, *Chem. Rev.* **2013**, *113*, 3516–3604.
205 A. Lis-Cieplak, J. Sitkowski, W. Kolodziejski, *J. Pharm. Sci.* **2014**, *103*, 274–282.
206 G.-F. Luo, X.-D. Xu, J. Zhang, J. Yang, Y.-H. Gong, Q. Lei, H.-Z. Jia, C. Li, R.-X. Zhuo, X.-Z. Zhang, *ACS Appl. Mater. Interfaces* **2012**, *4*, 5317–5324.
207 A. Franc (Brno, CZ), P. Sova (HradecnKralove, CZ), *Patent US 20090209641*, **2009**.
208 M. S. Jhaveri, A. S. Rait, K.-N. Chung, J. B. Trepel, E. H. Chang, *Mol. Cancer Ther.* **2004**, *3*, 1505–1512.
209 P. K. Naik, M. Lopus, R. Aneja, S. N. Vangapandu, H. C. Joshi, *J. Comput. Aided. Mol. Des.* **2012**, *26*, 233–247.
210 L. E. Kelemen, *Int. J. Cancer* **2006**, *119*, 243–250.
211 V. Giglio, V. Oliveri, M. Viale, R. Gangemi, G. Natile, F. P. Intini, G. Vecchio, *Chempluschem* **2015**, *80*, 536–543.
212 N. Wiedenhof, J. N. J. J. Lammers, C. L. van Panthaleon Van Eck, *Starch - Stärke* **1969**, *21*, 119–123.
213 A. Harada, M. Furue, S. Nozakura, *Polym. J.* **1981**, *13*, 777–781.
214 G. Crini, M. Morcellet, *J. Sep. Sci.* **2002**, *25*, 789–813.
215 B. Gidwani, A. Vyas, *Colloids Surf. B. Biointerfaces* **2014**, *114*, 130–137.
216 K. Teranishi, K. Watanabe, M. Hisamatsu, T. Yamada, *J. Carbohydr. Chem.* **1998**, *17*, 489–494.
217 F. Barbato, B. Cappello, M. I. La Rotonda, A. Miro, F. Quaglia, *J. Incl. Phenom. Macrocycl. Chem.* **2003**, *46*, 179–185.
218 V. H. Soto Tellini, A. Jover, J. C. García, L. Galantini, F. Meijide, J. V. Tato, *J. Am. Chem. Soc.* **2006**, *128*, 5728–5734.
219 S. Daoud-Mahammed, P. Couvreur, K. Bouchemal, M. Chéron, G. Lebas, C. Amiel, R. Gref, *Biomacromolecules* **2009**, *10*, 547–554.
220 V. Wintgens, C. Amiel, *Eur. Polym. J.* **2010**, *46*, 1915–1922.
221 M. di Cagno, T. Terndrup Nielsen, K. Lambertsen Larsen, J. Kuntsche, A. Bauer-Brandl, *Int. J. Pharm.* **2014**, *468*, 258–263.

222 J. A. Arancibia, G. M. Escandar, *Analyst* **1999**, *124*, 1833–1838.

223 C. Moers, L. Nuhn, M. Wissel, R. Stangenberg, M. Mondeshki, E. Berger-Nicoletti, A. Thomas, D. Schaeffel, K. Koynov, M. Klapper, et al., *Macromolecules* **2013**, *46*, 9544–9553.

224 M. Othman, K. Bouchemal, P. Couvreur, R. Gref, *Int. J. Pharm.* **2009**, *379*, 218–225.

225 S. Wilhelm, C. Carter, M. Lynch, T. Lowinger, J. Dumas, R. A. Smith, B. Schwartz, R. Simantov, S. Kelley, *Nat. Rev. Drug Discov.* **2006**, *5*, 835–844.

226 D. Strumberg, A. Awada, H. Hirte, J. W. Clark, S. Seeber, P. Piccart, E. Hofstra, D. Voliotis, O. Christensen, A. Brueckner, et al., *Eur. J. Cancer* **2006**, *42*, 548–556.

227 M. L. Bondì, C. Botto, E. Amore, M. R. Emma, G. Augello, E. F. Craparo, M. Cervello, *Int. J. Pharm.* **2015**, *493*, 75–85.

228 L. Dong, Y. Zhang, Y. Zhao, H. Wang, Y. Wang, Z. Luo, H. Jiang, X. Yang, C. Duan, B. Zhang, *Fuel* **2015**, *155*, 55–62.

229 H. Cao, Y. Wang, X. He, Z. Zhang, Q. Yin, Y. Chen, H. Yu, Y. Huang, L. Chen, M. Xu, et al., *Mol. Pharm.* **2015**, *12*, 922–931.

230 T. Higuchi, K. A. Connors *Adv. Anal. Chem. Instrum.* **1965**, *4*, 117–122.

231 M. M. Doile, K. A. Fortunato, I. C. Schmücker, S. K. Schucko, M. A. S. Silva, P. O. Rodrigues, *AAPS PharmSciTech* **2008**, *9*, 314–321.

232 Z. Fülöp, T. T. Nielsen, K. L. Larsen, T. Loftsson, *Carbohydr. Polym.* **2013**, *97*, 635–642.

233 N. J. Gleason, C. J. Nodes, E. M. Higham, N. Guckert, I. A. Aksay, J. E. Schwarzbauer, J. D. Carbeck, *Langmuir* **2003**, *19*, 513–518.

234 B. Pauwels, G. Van Tendeloo, C. Thoelen, W. Van Rhijn, P. A. Jacobs, *Adv. Mater.* **2001**, *13*, 1317–1320.

235 B. Godin, C. Chiappini, S. Srinivasan, J. F. Alexander, K. Yokoi, M. Ferrari, P. Decuzzi, X. Liu *Adv. Funct Mat*. **2012**, *22*, 4225–4235.

236 A. Zabala Ruiz, H. Li, G. Calzaferri, *Angew. Chem. Int. Ed. Engl.* **2006**, *45*, 5282–5287.

237 J. Park, S. Bauer, K. von der Mark, P. Schmuki, *Nano let*. **2007**, *7*, 1686−1691.

238 L. Ferreira, J. M. Karp, L. Nobre, R. Langer *Cell Stem. Cell.* **2008**, *3*, 136−146.

239 D. Bocking, O. Wiltschka, J. Niinimaki, H. Shokry, R. Brenner, M. Linden, C. Sahlgren *Nanoscale* **2014**, *6*, 1490−1498.

240 N. S. Kehr, H.-J. Galla, K. Riehemann, H. Fuchs, *RSC Adv*. **2015**, *5*, 5704−5710.

241 O. Olivares, N.V. Likhanova, B. Gómez, J. Navarrete, M.E. Llanos-Serrano, E. Arce, J.M. Hallen *Appl. Surf. Sci.* **2006**, *252*, 2894–2909.

242 N. Wong Shi Kam, M. O'Connell, J. A. Wisdom, H. Dai *PNAS* **2005**, *102*, 11600 –11605.

243 Y. Li, X. Chen, N. Gu, *J. Phys. Chem. B* **2008**, *112*, 16647–16653.

244 B. Di Blasio, S. Galdiero, M. Saviano, C. Pedone, E. Benedetti, E. Rizzarelli, S. Pedotti, G. Vecchio, W. A. Gibbons, *Carbohydr. Res.* **1996**, *282*, 41–52.

245 R. J. Lee, P. S. Low, *J. Biol. Chem.* **1994**, *269*, 3198–3204.